AD-A060 463 PURDUE UNIV LAFAYETTE IND PROJECT SQUID HEADQUARTERS F/G 20/4
AN EXPERIMENTAL STUDY OF THE TRANSPORT OF A NON-DIFFUSIVE SCALA--ETC(U)
AUG 78 K C CORNELIUS, J F FOSS N00014-75-C-1143
UNCLASSIFIED SQUID-MSU-1-PU NL

1 OF 2
AD A060 463

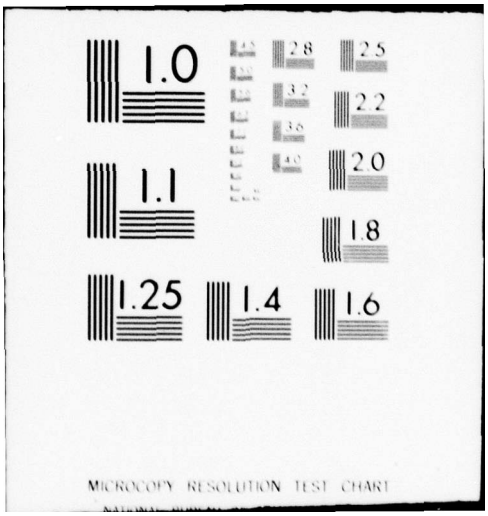
1.0
1.1
1.25
1.4
1.6
1.8
2.0
2.2
2.5
2.8
3.2
3.6
4.0
MICROCOPY RESOLUTION TEST CHART

AD A060463

DDC FILE COPY

(12) 5c

LEVEL II

PROJECT SQUID
TECHNICAL REPORT MSU-1-PU

AN EXPERIMENTAL STUDY OF THE TRANSPORT OF A NON-DIFFUSIVE SCALAR CONTAMINANT IN THE DECAYING TURBULENCE FIELD OF AN ENCLOSED CHAMBER

BY

K. C. CORNELIUS
J. F. FOSS
MICHIGAN STATE UNIVERSITY
EAST LANSING, MICHIGAN 48824

PROJECT SQUID HEADQUARTERS
CHAFFEE HALL
PURDUE UNIVERSITY
WEST LAFAYETTE, INDIANA 47907

AUGUST 1978

DDC
RECEIVED
OCT 30 1978
A

Project SQUID is a cooperative program of basic research relating to Jet Propulsion. It is sponsored by the Office of Naval Research and is administered by Purdue University through Contract N00014-75-C1143, NR-098-038.

This document has been approved for public release and sale;
its distribution is unlimited

78 10 24 047

(14) SQUID-

Technical Report MSU-1-PU

PROJECT SQUID

A COOPERATIVE PROGRAM OF FUNDAMENTAL RESEARCH
AS RELATED TO JET PROPULSION
OFFICE OF NAVAL RESEARCH, DEPARTMENT OF THE NAVY

CONTRACT (15) N00014-75-1143 NR-098-038

(6) AN EXPERIMENTAL STUDY OF THE TRANSPORT OF A NON-DIFFUSIVE SCALAR CONTAMINANT IN THE DECAYING TURBULENCE FIELD OF AN ENCLOSED CHAMBER,

by (9) Final rept.,

(10) K. C./Cornelius
J. F./Foss
Michigan State University
East Lansing, Michigan 48824

(11) August 1978

(12) 116p.

PROJECT SQUID HEADQUARTERS
CHAFFEE HALL
PURDUE UNIVERSITY
WEST LAFAYETTE, INDIANA 47907

THIS DOCUMENT HAS BEEN APPROVED FOR PUBLIC RELEASE AND SALE:
ITS DISTRIBUTION IS UNLIMITED

78 10 24 047
403 617 LB

TABLE OF CONTENTS

		Page
List of Tables		
List of Figures		
1.	INTRODUCTION	1
2.	EXPERIMENTAL FACILITY AND TECHNIQUES	5
	2.1. Introduction	5
	2.2. Details of the Experimental Facility	5
	2.3. Optical System	6
	2.4. Particle Generators	8
	2.5. Signal Processing	10
3.	ANALYTICAL AND BACKGROUND CONSIDERATIONS	13
	3.1. Description of the Problem	13
	3.2. Scalar Concentration Field	16
	3.2.1. The Ensemble Average Concentration Distribution	16
	3.2.2. The Ensemble Average Fluctuation Intensity Distribution	20
	3.2.3. Dispersion Considerations	21
	3.2.4. Fourier Transform Considerations	25
4.	DYNAMIC BEHAVIOR OF THE MARKING PARTICLES	28
	4.1. Aerodynamic Drag	28
	4.2. Gravitational Effects	32
	4.3. Particle Diffusion by Molecular Agitation	32
	4.4. Influence of Particles on Carrier Gas Properties	33
5.	RESULTS	35
	5.1. Flow Visualization	35
	5.2. Data Base for the Particle Experiments	38
	5.3. Ensemble Average Distributions	39
	5.4. Measures of the Instantaneous Scans	41
6.	DISCUSSION OF RESULTS	45
	6.1. The Ensemble Average Concentration Distributions	45
	6.2. Measures of the Instantaneous Scans	47
	6.3. Inference of the Lagrangian Scales in the Present Experiment	48
	6.3.1. A Priori Estimation of the Lagrangian Microscale	49
	6.3.2. Evaluation of Parameters which Describe the Turbulent Dispersion	50

		Page
6.3.2.1.	A Posteriori Evaluation of the Microscale and Δt_r	51
6.3.2.2.	A Posteriori Evaluation of the Macroscale	54
7.	SUMMARY AND CONCLUSIONS	55
REFERENCES		60
APPENDIX A:	GAS HANDLING SYSTEM	101
APPENDIX B:	THE DESIGN OF THE GRID/SPLITTER PLATE ACTUATION SYSTEM	108
APPENDIX C:	REPRESENTATIVE UNSTABLE, NEUTRALLY STABLE AND STABLE, NON-DIFFUSIVE MIXING FIELDS AS REVEALED BY THE PRESENCE($), ABSENCE ( ) OF THE MARKING CONTAMINANT IN THE SCATTERING VOLUME	115
APPENDIX D:	DISPERSION IN A DECAYING TURBULENCE FIELD	120
APPENDIX E:	A REVIEW AND REEVALUATION OF SHLIEN'S EXPERIMENTAL RESULTS IN HOMOGENEOUS DECAYING TURBULENCE	128

NOTE: The Appendices have been removed from the Final Report because of length limitations. They are available from the second author.

LIST OF TABLES

Table I. Slit and Scattering Volume Dimensions from Selected Locations — Page 64

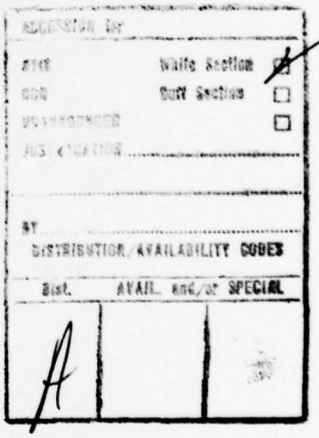

List of Figures

Figure		Page Number
Figure 1.	Schematic Representation of the Mixing Chamber	65
Figure 2.	Detail of Turbulence Generating Grid	66
Figure 3.	Schematic Representation of the Acceleration/Deceleration System	66
Figure 4.	Velocity of Grid as a Function of Time	67
Figure 5.	Schematic Representation of the Optical and Data Acquisition Systems	68
Figure 6.	Detailed Representation of Disc and Slits	69
Figure 7.	Representative cross-section of Light Transmission Slit in the Rotating Disc	70
Figure 8.	Particle Generator suitable for use with air	71
Figure 9.	Electron Microscope Photograph of Soy Bean Oil Droplets	72
Figure 10.	Particle Generator to create 0.5 μ crystals of Acetic Acid	73
Figure 11.	Electron Microscope Photograph of Acetic Acid Particles	74
Figure 12.	Ink Tracings of Oscilloscope Photographs Showing: a) an instantaneous scan of the photomultiplier tube voltage (E_{pmt}) for the second scan following the passage of the grid b) a 3-second time exposure of the scope traces for the fully mixed condition of large time.	75

PRECEDING PAGE BLANK

List of Figures
Page 2

Figure		Page Number
Figure 13.	Data Acquisition System	76
Figure 14.	Circuit Diagram for the Comparator Circuit	77
Figure 15.	Representation of the non-diffusing mixing field	78
Figure 16a	Representative length and velocity scales for homogeneous turbulence taken from Wyatt (1955)	79
Figure 16b	Schematic representation of the quantities used in the Lagrangian dispersion analysis	80
Figure 17.	Amplitude response of spherical particles to an oscillatory air flow from equation 4.1.7.	81
Figure 18.	Close-up of the initial mixing process to show the periodic structures developed from the instability of the vortex sheet	82
Figure 19.	Schematic representation of the parameters associated with the initial mixing process	83
Figure 20.	Close-up of the mixing phenomena	84
Figure 21.	Large view of the mixing phenomena	85
Figure 22.	Representative $\langle\Gamma(z,t)\rangle$ Distributions for the Gas Mixing Experiments Presented on Standard and Probability Coordinates	86
Figure 23.	Comparison of the $\langle\Gamma(z,t)\rangle$ measurements for the Freon 12 and air data sets $U_o t/M = 12$	87
Figure 24.	Sample Least Squares Fits, to the Ensemble Average Data for the Freon 12 and Air Carrier Gases, on Probability Coordinates	88

List of Figures
Page 3

Figure		Page Number
Figure 25.	Probability Coordinates Representation of Ensemble Average Concentration for Freon	89
Figure 26.	Probability Coordinates Representation of Ensemble Average Concentration for Air	90
Figure 27a	Width Measure (σ_m) of the ensemble average concentration distribution - short time results	91
Figure 27b	Width Measure (σ_m) of the ensemble average concentration distribution Long time results	92
Figure 28.	z Values of Physical Displacement from Centerline Corresponding to $\langle\Gamma(z,t)\rangle = 0.15$ and 0.85	93
Figure 29.	Definitions of Instantaneous Scan Measures	94
Figure 30a	Measures of the Mixing Region Width as Determined from the Conventional and the Instantaneous Scans . . . Freon 12 Carrier Gas	95
Figure 30b	Measures of the Mixing Region Width as Determined from the Conventional and the Instantaneous Scans . . . Freon 12 Carrier Gas	96
Figure 31.	Evaluation of the Lagrangran Microscale (τ^*) and the Effective Release time (t_r).	97
Figure 32.	Long Time Results for the Dispersion Parameter z_p^2	98
Figure 33.	Theoretical values of z^{*2} $(\Delta t/\Delta t_r; \tau^*, n)$	99
Figure 34.	Theoretical values of z^{*2} $(\Delta t/\Delta t_r; \Lambda^*, \Delta t_j, \Delta t_r, n)$	100

ABSTRACT

AN EXPERIMENTAL STUDY OF THE TRANSPORT OF A
NON-DIFFUSIVE SCALAR CONTAMINANT
IN THE DECAYING TURBULENCE FIELD
OF AN ENCLOSED CHAMBER

An experimental investigation of the convective properties of a turbulence field within a closed mixing chamber has been executed; the investigation is supported by appropriate theoretical analyses. The purposes of the study were (i) to develop an experimental technique which could ascertain the convective, or dispersive, properties of such a turbulence field (i.e., with the constraint of "zero" molecular diffusivity) and (ii) to document the influence of the Reynolds number on the convective transport properties of a representative field.

The derived technique involves the introduction of submicron particulate matter into the lower half-volume (as defined by a horizontal splitter plate which is rapidly removed from the chamber at the initiation of an experiment) and the subsequent monitoring of the presence/absence of this contaminant along a vertical line centered at the plane of the splitter plate. An optical/mechanical/electrical technique was used to scan 205 locations along a 7.4 cm portion of an incident, focused ($d \simeq 0.1$ mm) , laser beam and the scattered light intensity was used to identify the presence or absence of the fluid elements which originated in the lower half-volume. That is, since the particulate matter is shown to be too large to respond to the diffusion effects of the Browman motion of the gas, and too small to move independently of the fluid element of its origin, it is inferred that it faithfully marks the lower half-volume

PRECEDING PAGE BLANK

fluid over the duration of the experiment (0.6 sec). The 7.4 cm scan length covered 2.92 mesh lengths of the biplane, round rod, turbulence generating grid. Air was used for 69 experiments; Freon 12 was used for 100 experiments ($\nu_{air} = 5.8\nu_{Freon\ 12}$).

A principal result of this investigation is that the particle dispersion is dependent upon the mesh Reynolds number (U_oM/ν); the width of the mixing field was found to decrease as the Reynolds number was increased. A theoretical model of the dispersion was developed using the suggestion by Batchelor and Townsend [1956] that the Lagrangian velocity auto correlation function can be made stationary, in a decaying turbulence field,by an appropriate stretching of the time coordinate. The present model utilizes both the Lagrangian micro and macro scales to describe this correlation function; numerical values for these two scales are inferred from the experimental data. The observed decrease in the particle dispersion with increasing Reynolds number is supported by a previously suggested relationship between the Lagrangian micro scale and the mesh Reynolds number, a new value for the coefficient in this relationship is proposed.

Analytical considerations are presented to support the use of a (spatial) Gaussian cumulative distribution function for the description of the ensemble average concentration; viz,

$$\Gamma(z,t) = [2\pi\ \sigma_m(t)^2]^{-1/2} \int_o^z \exp - [(\hat{\alpha} - \langle z \rangle)/2\sigma_m(t)^2]d\hat{\alpha}.$$

Satisfactory agreement between this distribution and the experimental data was obtained; $\sigma_m(t)^2$ was used to evaluate the mean square particle dispersion, z_p^2. Two properties of the instantaneous scans were defined: i) an ensemble average measure of the instantaneous width of the mixing field, σ_I, and an ensemble average measure of the migration of the instantaneous center lines, $\sigma_{\Delta z}$. The instantaneous scans are shown to have essentially the same width as that of the ensemble average field $\sigma_I \gtrsim 0.8\sigma_m$ whereas $\sigma_{\Delta z}$ exhibits very little growth with respect to time following the establishment of its nominal value at $U_ot/M \simeq 8$.

NOMENCLATURE

a	radius of particle
$\mathring{A}$	angstrom 10^{-10}
A_e	area of exit discharge nozzle
A	experimental constant in energy decay law, see 3.1.7
A_p	area of piston
A_G	cross sectional area of grid
B	constant
$B(\vec{k})$	Fourier transform of $\Gamma(x,y,z)$
B^*	complex conjugate of B
$B_\gamma(k)$	amplitude spectra of $<\gamma^2>$
C	concentration of scalar contaminant
c_s	constant 7.14 cm/radian
C_L	constant defined in (6.3.1)
C_D	drag coefficient
C_v	strength of irrotational vortex
C_λ	see (3.2.24)
C_1	$C_\lambda/(1-n/2)$
C_f	see 3.2.5
C_2	$C_f/(1-n/2)$
dL	diameter of biplanar grid elements
d_o	minimum diameter of focused laser beam
d	diameter of laser beam at $(1/e^2)$ intensity level
D	molecular diffusivity
D_τ	turbulent diffusivity
D_p	particle diffusivity
f	focal length of lens

F	drag force of grid
$F_n(\vec{k})$	Fourier transform of u(x,y,z)
g	gravitational constant
H	lateral dimension of chamber
h	distance between concentrated vorticity centers
I_s	intensity of segregation
(i,j,k)	indicial notation
K_B	Boltzman constant
$\vec{k}$	wavenumber variable
L	length of cylinder (hydraulic)
L_s	scale of segregation
L_p	length scale for the dispersion analysis, see (3.2.21)
m_p	mass of particle
m_t	total mass which is attached to piston rod
M	mesh length of grid
m	$m = (1-n/2)$, m is used in the dispersion analysis
N	number of experiments
n	exponent of decay law, see (3.1.7)
p	pressure (static)
P_p	pressure acting on piston
$\tilde{q}$	turbulent energy intensity $(\bar{u}^2+\bar{v}^2+\bar{w}^2)^{1/2}$
r	radial coordinate
r_o	inner radius of helical slit 6.99 cm
r_e	eddy of Kolmogoroff size
R_L	Lagrangian correlation coefficient, see (3.2.19)
R_M	Reynolds number $(U_o M/\nu)$
S_c	Schmidt Number (ν/D)
S_T	Strouhal number

t	time variable
δt_L	time increment equal to the transform, (3.2.24), of the microscale τ_L
t_o	apparent origin of kinetic energy decay
Δt	$t-t_o$
Δt_j	from the transformation of the juncture point, see (3.2.25)
T	temperature (absolute)
t_m	total elapsed time for passage of grid through chamber
t_r	see (3.2.21), release time of the contaminant
$T_n(\vec{k})$	transfer function
u	velocity in x direction
u_θ	component of velocity (cylindrical coordinates)
U_o	speed of grid
v	velocity in y direction
v_r	radial component of velocity (cylindrical coordinates)
w	velocity in z direction
$\tilde{w}$	r.m.s. of the z component velocity fluctuation
W	total work done on fluid by action of grid
$\langle X_i^2 \rangle$	mean square displacement of a fluid particle
(x,y,z)	cartesian coordinates, x in direction of U_o, z in direction of mean gradient of Γ
Δz_o	length of focused laser beam in which d_o is constant
z_m	centerline of mixing chamber
z^*	normalized root mean square of the particle displacement $z_p^2/L_p^2 = z^{*2}$
z_c	center of ensemble average distribution
$\langle z_p^2 \rangle$	mean square displacement of particle in the z direction
$z_{(\ )}$	see figure 29 for definition of special symbols

GREEK SYMBOLS

α	$3\nu/a^2$
$\hat{\alpha}$	dummy variable of integration
β	$3\rho/(2\rho_p+\rho)$
Γ	concentration of non diffusive contaminant
γ	fluctuating value of Γ; $(\Gamma - \langle\Gamma\rangle)$
Λ	incremental value
δ	boundary layer thickness
ε	dissipation of turbulent energy
ω	frequency (wavenumber)
θ	radians (angular)
$\hat{\theta}$	unit vector in θ direction
λ	wavelength of disturbance
λ_g, λ_t	Taylor microscale (g: spatial, t: time)
λ_L	wavelength of laser radiation
Λ^*	Lagrangian macroscale Λ/C_2
μ	absolute viscosity
ν	kinematic viscosity
ρ	density of fluid
ρ_p	density of particle
σ_m	standard deviation of the spatial distribution for $\langle\Gamma(z,t)\rangle$ (a Gaussian distribution for $\langle\Gamma(z,t)\rangle$ is assumed, see section 5), see 3.2.12
$\sigma_{\Delta z}$	see 5.4.1
σ_I	see 5.4.2
τ	stretched time coordinate, $\tau = C \ln \Delta t/\Delta t_\tau$, see (3.2.24,5)
τ_L	Lagrangian microscale in the stationary coordinates
τ^*	τ_L / C_1
υ	Lagrangian velocity

1. INTRODUCTION

The efficient mixing of one fluid, or a contaminant substance, with the host fluid is an intrinsic feature of a turbulent flow. The term "mixing" is often used to describe the net effects of turbulent dispersion, in which the eddying motions provide a convective transport of the material to be mixed, and molecular diffusion, in which the concentration of the material in a given fluid element is changed by the transport associated with the agitation at the molecular level. As noted by Brodkey [1975] the interpretation of the degree of mixing is related to the scale of the observation, i.e., to the size of the volume used to define the concentration. Two measures of mixing are commonly employed, Brodkey [1975], the intensity of segregation I_s and the scale of segregation L_s. For a binary mixture, where C is the instantaneous concentration $(\bar{C}+c)$ of the contaminant, the intensity of the segregation (I_s) is given as

$$I_s = \frac{\overline{c^2}}{\bar{C}(1-\bar{C})} \qquad (1.1)$$

and the scale of the segregation (L_s) is given as

$$L_s = \int \overline{c(\vec{x})c(\vec{x}+\vec{r})}\,dr \qquad (1.2)$$

The turbulent motions play a dual role in the mixing process. They are responsible for the convective transport of the material to be mixed and they can greatly enhance the molecular diffusion by straining the concentration field and hence steepening the spatial gradient of the transported material. This dual role, and the influence of the initial events on the subsequent distributions, result in turbulent mixing phenomena which are of fundamental interest.

The present investigation was conceived and executed as the first stage of a research program to examine these basic phenomena of turbulent mixing. The total program is to involve measurements of the velocity, the molecular species concentration

and the presence or absence of a non-diffusive contaminant in a simple mixing field which may be characterized as a decaying, homogeneous turbulence field. The initial condition for the mixing is similarly simple; the fluids to be mixed are segregated in two distinct volumes until the initiation of the mixing process. The series of experiments in the total program are to reveal the influence of the control variables: different states of the initial turbulence kinetic energy and scales, and ii) different densities of the gases to be mixed. The data acquisition techniques, discussed below, are to provide quite detailed representations of the mixing process.

The present study is solely concerned with the development and application of the non-diffusive contaminant experimental technique. The contaminant is introduced into one-half of the mixing chamber and is convectively mixed with the other half-volume following the initiation of the experiment. Mechanical/optical techniques are used to identify the presence/absence of the contaminant within small volumes along a segment of the mixing region. Since the half-volume of origin of the fluid element is known, the dispersive properties of the turbulence field may be inferred. The use of a closed mixing chamber greatly simplifies the task of providing a sufficient volume of the marking contaminant. Hence, this distinctive experimental technique would be somewhat more difficult to utilize in conventional wind tunnel flow systems.

The first analytical description of dispersion in a homogeneous, stationary turbulence field is that provided by Taylor (1921) in the classic paper entitled "Diffusion by Continuous Movements," Townsend (1954) recognized that the straining action of the turbulence would influence the (molecular) diffusive as well as the dispersive properties of the field and suggested appropriate modifications to the Taylor analysis. Townsend's concepts were refined by Saffman (1961) and the full problem has been reconsidered most recently by Chevray (1977).

The physically realistic case of decaying homogeneous turbulence is, in contradistinction to the above studies, non-stationary. Batchelor and Townsend (1956) propose that an appropriate stretching of the time coordinate will cause the Lagrangian correlation function to be stationary. This hypothesis is a central element of the theoretical structure which is utilized to interpret the experimental results. The objective of these theoretical considerations is, like the prior efforts of Uberoi and Corrsin (1953) and Shlien and Corrsin (1975), to deduce Lagrangian scales from the observed dispersion measurements. Tennekes [1975] has reexamined the data of Shlien and Corrsin and has derived an analytical relationship between the Eulerian and Lagrangian time microscales in decaying isotropic turbulence. Tennekes shows that the ratio of the Lagrangian microscale to the Eulerian time microscale is proportional to $R_\lambda^{\frac{1}{2}}$; ($R_\lambda = q\,\lambda/\nu$). Quantitative reevaluations of the Shlien and Corrsin and the Tennekes results are presented in Appendix E. An important difference between the present and former experiments is the diffusive nature of the contaminant used to mark the fluid; a line source of heat was used to thermally mark the fluid elements in the above two research efforts. A second major difference is associated with the time which is available for the dispersion. The temperature "tagging" experiments were initiated following the establishment of a homogeneous and approximately isotropic turbulence state. Consequently, a relatively limited extent of the stretched time coordinate was available for the contaminant dispersion. Conversely, the present experiment initiates the dispersion in the initially inhomogeneous field and thereby gains a substantial period of development in the stretched time coordinate. A third feature of the present experiment is that the primary data are derived from essentially instantaneous scans through the mixing field with the ensemble statistics being generated from a number of experiments. Consequently, the data base is characterized by considerable detail in terms of a given scan through the mixing region and a relatively limited number of realizations

with which to form any particular ensemble average. The former feature is used to evaluate the statistical features of the instantaneous scans; these interpretations are not possible with the classical wind-tunnel, single-probe techniques.

The above matters are made explicit in the following sections. Section 2 presents the Experimental Facility and Techniques, including the mixing chamber, the optical data acquisition system, the contaminant generator and the signal processing units. Analytical descriptions of the various aspects of this investigation are presented in Section 3. The dynamics of small particles and the analytical considerations which support the interpretation of the present particles as being non-diffusive are presented in Section 4. Section 5 presents the results which can be inferred from the binary (presence/absence of contaminant) data from each observation volume along the sampled segment. The relationship between the theoretical considerations and the experimental results is presented in Section 6.

2. EXPERIMENTAL FACILITY AND TECHNIQUES

2.1. Introduction

A turbulent motion in the absence of a mean velocity was generated by passing a bi-planar grid through an enclosed volume. Light scattering techniques were used to sense the presence or absence of the submicron particles which served as a marking agent for the gas originally contained in the lower half volume, subsequently referred to as gas B. A rapid scan of the mixing region was made possible by an optical-mechanical system. Light scattering intensity measurements were sequentially recorded from short (0.36mm), small diameter (0.2 mm) portions of a 74 mm segment of the incident laser beam. The physical apparatus to create the mixing field and to execute the measurements is described in detail in the following sub-sections. It should be noted that the rapid scan represents a unique experimental technique. The gas handling system that was required for introducing superheated Freon 12 and 22 into the mixing chamber is described in Appendix A.

2.2. Details of the Experimental Facility

A schematic representation of the mixing chamber is shown in Figure 1. The mixing chamber was constructed of 1.25 cm plate stock of dimensions (0.46x0.46x0.61)m; the large I-beams provided a rigid support for the apparatus. The incident light ports were covered with 17.8 cm diameter coated glass discs; the viewing port was a 12.7 cm hole which accommodated the collection lens.

A 0.159-cm thick divider plate was located at the midsection of the chamber and separated the two gas volumes (A and B) prior to the initiation of the experiment. The plate extended through the end wall of the chamber which was fitted with four Teflon guide surfaces to inhibit the flexing of the plate during acceleration and deceleration. The grid/splitter plate system was supported on four linear ball bearings which provided a smooth but rigid transport of the plate and grid to the forward section of the chamber at the initiation of the experiment. The square mesh, biplanar, round rod grid was constructed of aluminum

tubing pinned at the bar cross-sections; it was permanently fixed at the end of the plate. The diameter and mesh size were selected to provide a solidity ratio of 0.34; the tubing diameter was 0.476 cm with a mesh width of 2.54 cm. Figure 2 provides a photograph of the opened mixing chamber. The splitter plate has been removed; the grid and the ends of the four guide ways are visible.

A schematic representation of the acceleration/deceleration system is shown in Figure 3. The quick acting solenoid valve allowed the rapid pressurization of the pneumatic side of the cylinder. When the unit is operated, the piston and the attached grid and splitter plate accelerated until the back pressure in the hydraulic fluid was sufficiently large to create a zero net force on the piston. The deceleration was accomplished by the gradual seating of a tapered plug attached to the end of the activating shaft. This facility provided a relatively uniform acceleration from 0 to 6.22 m/sec in 8.9 cm, a "constant" speed through the chamber, and a deceleration over the final 2.5 cm of travel. This motion was measured by attaching a hot wire ($d = 20\mu m$) on the moving assembly. A linearizer was used and an exponent was chosen to match the upper velocity range with the "best" linear response. A plot of the velocity versus time is shown in Figure 4. See Appendix B for the detailed design and the computer simulation considerations of the acceleration/deceleration system.

2.3. Optical System

A schematic representation of the optical system is presented in Figure 5. A Coherent Radiation CR-5 Argon Ion laser was used as the light source. The laser was tuned for the 4880 Å line with an output power level of 0.4 watts. The 2-mm diameter laser beam was focused with a 31.75-cm focal length spherical lens and directed by front surface mirrors from the top to the bottom of the chamber through two transparent windows.

The collection optics consisted of two aerial photography camera lenses (focal number of 4.0, focal length of 30.5 cm) which were placed in close proximity in order to achieve a

1.36 magnification of the original image. This represented the maximum magnification and consequently the minimum scan length with the available optics. These conditions were necessary since the smallest scales of the turbulent motion were estimated to be 0.1 mm. The resulting scan in the mixing chamber covered 7.38 cm. The first lens was placed flush with the inside surface of the 12.7-cm hole in the side of the chamber. This eliminated the need for a finite thickness window which would have caused spherical aberrations of the scattered light. The second lens was coaxial with the first and was moved axially such that the image of the incident laser beam could be focused onto the face of a rotating disk.

The high strength aluminum disk served as an optical-mechanical gate by only allowing the transmission of light from a scattering volume defined by the intersection of the recreated beam and a slit cut in the face of the disk. The slits were machined following the contour $r = r_o + c_s\theta_i$ where $c_s = 7.14$ cm/radian, $r_o = 6.99$ cm, $0 \leq \theta \leq 80^o$ and $\theta_i = \theta + \frac{\pi}{2}(i-1)$. The disk was rotated at constant speed (4286 rpm) by a 1/2 h.p. motor. Since $d\theta/dt$ = constant, dr/dt is also constant and the optical-mechanical gate provides a constant rate scan of the recreated laser line over the radial span $r_o \leq r \leq r_o + 10$ cm. The scan is centered at the midplane of the mixing field. Each scan was completed in 3.11 msec; the scans were repeated each 3.5 msec. Figure 6 presents a detailed representation of the disc and slits. Some difficulty was encountered when trying to cut a slit width of 0.025 cm on the face of the disk. The machining operation left a groove which varied linearly from 0.06 cm to 0.025 cm. Following numerous attempts to rectify this situation, a solution was achieved by placing Mylar tape over the machined groove and cutting a slit with two razor blades displaced by 0.025 cm. One of the edges on the disk was used as a guide. Microphotographs were taken of the slit variation after the data had been accumulated; a sample is shown in Figure 7. The slit widths determined from these photographs are presented in Table 1. The height of

the scattering volume is a function of the magnification ratio (1.36), the diameter of the laser beam and the intersection angle between the slit and the recreated laser beam. Table 1 also presents the scattering volume heights for representative locations. The diameter of the scattering volume was established by the focusing lens. Johnson [1971] provides an analytical description of the minimum diameter, d_o, and the length, Δz_o, over which the diameter is maintained. The minimum diameter d_o is located at $\frac{\Delta z_o}{2}$ from either end of the "constant" diameter region.

$$d_o = \frac{4}{\pi} \frac{\lambda_L f}{d_L} \cong 0.1 \text{ mm} \qquad (2.3.1)$$

where f = focal length of lens (31.75 cm), $\lambda_{Laser} = 4880\mathring{A}$, $d_L = 2$ mm.

$$\Delta z_o = 4 \left(\frac{f}{d_L}\right)^2 \lambda_L \cong 5 \text{ cm} \qquad (2.3.2)$$

The total scan length was 7.38 cm and 205 data points were acquired along the scan. The distance between centers of the sample volumes was slightly greater than the nominal length of the volumes, namely 0.36 versus 0.3 mm; hence no known spatial overlapping between samples was incurred.

The alignment procedure was quite critical and great care was taken to align the laser beam parallel to the disk and then to focus a point source onto the face of the rotating disk. The latter was accomplished by adjusting the focal length of the second lens until the pulse width from the photomultiplier tube was a minimum. This alignment procedure allowed less than 0.1 degrees alignment difference between the incident and focused laser beams.

2.4. Particle Generators

Two particle generators were developed in the course of this investigation. The first, which was quite satisfactory for use with (at least) air was not suitable for use with Freon. Both generators will be described in this section.

The generator was required to produce approximately 10^6 particles/cc of carrier gas; this concentration is necessary

to achieve the nominal value of 20 particles/scattering volume. Further requirements include:

i) particle sizes: $0.5 \pm \simeq 0.3$ microns (μm)

ii) non-toxic particles

iii) method of generation should be independent of carrier gas

iv) particle dimensions should be stable over the lifetime of the experiment.

The first generator satisfied requirements (i) and (ii); it is shown in Figure 8.

The particles were formed from soybean oil which was introduced as droplets into the stream of carrier gas. An oil lubricator, previously used in a compressed air system, was used to create the oil drops. The particle droplets for the experiment were created by the successive impacts of the initially (large) drops on the pressed wire screens (of diminishing open area) and the subsequent straining of the liquid by the shear of the higher speed gas. An electron microscope photograph of the resulting droplets (see Figure 9) indicated that droplet diameters of 0.2 - 0.4 microns were achieved with this generator. Unfortunately, the droplets so produced in Freon appeared to evaporate (or at least to change their surface charge characteristics). No particle scattering was observed when this scheme was used with Freon as the carrier gas.

The second particle generator satisfied all four criteria; it is shown schematically in Figure 10. This generator makes use of the Rayleigh instability of a capillary jet and the subsequent formation of droplets to create the desired marking particles. The stability of the particle was ensured by using a liquid solution of 10 percent acetic acid* in distilled water. When the liquid water evaporated following the droplet formation a crystalline residue was left to serve as the scattering particle. It was inferred that the 0.45-μm micro porous filter provided a capillary jet of the same diameter at its downstream face. A capillary jet is unstable; the analysis of Lord Rayleigh [1892] was used to infer that 0.9-μm droplets were formed. An

*Acetic acid: CH_3 COOH, m.w. 60.03

unambiguous measure of the particle sizes was not obtained. An electron microscope* photograph of the particles which settled from the mixing chamber is shown in Figure 11. A long time (24 hr.) was required for the settling and some agglomeration of the initially distinct particles is suspected. This technique is vulnerable to oversize droplets which impinge upon the upstream face of the filter; the apparent difficulty is the merging of the capillary jets and hence the formation of droplets of an excessive size. The generator system appeared to operate the same for the different carrier gasses....Freon 12 and 22 and Air. An improvement in the efficiency of the system would be desirable since an asymptotic state is reached when the particle contaminated gas is recycled through the compressor and particle generator.

2.5. Signal Processing

The scattered light, which is collected and focused onto the photomultiplier tube by the optical system, results in a voltage signal which can be used to signify the presence or absence of the marking particles. The characteristics of the photomultiplier tube and the signal processing electronics are described in this section.

An RCA 4518 photomultiplier tube was used for the experiments. This tube has a 20 cm^2 photosensitive area and a quantum efficiency of 18 percent. The 10K ohm load resistor and the associated capacitance of the output circuit resulted in a 5-μsec time constant. The tube was operated with 900 volts across the dynode chain; the corresponding cathode sensitivity and current amplification were 0.06 amps/watt and 8×10^3 respectively.

The particulate seeding was nominally controlled to provide 20 particles per scattering volume for the marked fluid. With this seeding density and for an incident laser power of 0.4 watts, the optical/electronics system delivered a current of approximately one micro amp. This current level corresponds to approximately 10^4 photoelectrons for each 5-μsec sample period. This relatively large number guarantees that the photomultiplier

*A 1% solution of Phototungstic acid (PTA) was added to the distilled water to facilitate the preparation of the slide.

tube and associated circuitry will not be adversely influenced by the dark current and that a statistically reliable representation of the particles' presence can be expected.

The photomultiplier tube signal was amplified (PAR 101) by 10^2 and input to an electronic comparator circuit. The comparator level of 0.06 volts was sufficiently above the "system noise/Rayleigh (molecular) Scattering/dark current" level of 0.02 volts such that no spurious readings were attributed to these effects. Voltage levels of greater than 0.06 volts were considered to represent the presence of particulate matter and hence the presence of gas B in the scattering volume. A minimum value of approximately 0.2 volts was observed for the region of particulate matter when the experiment was initiated; hence, the signal-to-noise level was approximately 10 and the minimum signal level exceeded the threshold by approximately 3. The voltage amplitude associated with the presence of the particulate matter did not exhibit a unique value; the amplitude fluctuations were inferred to be approximately ±50 percent of the average amplitude for those scattering volumes which contained the marked fluid. Consequently, it was not possible to set a criterion for the discrimination of a partially filled scattering volume. There are two principal factors which contribute to the amplitude fluctuation when the scattering volume is completely filled with marked fluid: (i) the nominal seeding of 20 particles per scattering volume results in a standard deviation of ±4.5 particles or ±23 percent (assuming a Poisson distribution for the number of particles in a scattering volume) and (ii) the variation in the scattering volume dimensions over the four scans was approximately ±25 percent.

Figure 12 presents an oscilloscope trace of the photomultiplier tube output immediately following the passage of the grid and splitter plate. The relevant voltage levels are noted on this trace. Figure 13 shows a block diagram of the data processing circuitry which achieves the analog to digital conversion and which synchronizes the data from the P.M. tube and rotating disk. The comparator curcuit which was used to

process the analog signal from the photomultiplier tube is shown in Figure 14.

Each scan of the mixing field is initiated by the strobe signal from the phototransistor. The phototransistor output is activated by the incident HeNe (low power) laser beam passage through the slit. This scheme for initiating the data scan is estimated to provide repeatability of 0.05 mm (or 14 percent of one scattering volume) in the spatial locations for the separate traverses. Figure 15 shows the binary output of the mixing field for one experimental run.

3. ANALYTICAL AND BACKGROUND CONSIDERATIONS

3.1 Description of the Problem

It is useful to consider the present study in terms of an idealized experiment and the differences between it and the actual experiments which were executed. The idealized experiment involves a homogeneous, isotropic turbulence field (of indefinite extent) at the initiation of the experiment (t=0). The initial concentration field is specified by the conditions

$$\Gamma(x,y,z,0) = 1 \text{ for } z < 0$$
$$\Gamma(x,y,z,0) = 0 \text{ for } z \geq 0 \qquad (3.1.1)$$

where $\Gamma = 1$ indicates the presence of the non-diffusive contaminant in the differential sized volume located at the (x,y,z) point. The subsequent $\Gamma(x,y,z,t)$ distributions result from the convective transport of the turbulence field. The actual experiment is rather different in certain of its detailed features. The passage of the splitter plate trailing edge provides an extremely rapid mixing of the upper and lower fluid regions over a scale several times the plate thickness (t_{plate} = 1.56 mm). This provides an actual "initial condition" which is a well-mixed region for ±7mm. Detailed considerations of the initial condition are presented in Section 5. The balance of the initial turbulence field is that which results from the passage of the biplanar grid.

The x-component, ensemble mean velocity will be positive (i.e., the fluid motion will be toward the receding grid) in the wake regions of the grid and splitter plate. The velocity u in the open regions will be negative. The closed mixing chamber results in the integral constraint:

$$\int \int u \, dy \, dz = 0 \qquad (3.1.2)$$

for all y and z in the interior of the chamber.

The differential forms of the mass and momentum conservation equations are instructive in the interpretation of the initial region behavior. Since the subject gases behave as incompressible, Newtonian fluids, these equations are written in their ensemble averaged form as

$$\frac{\partial \bar{u}_i}{\partial x_i} = 0 = \frac{\partial \bar{u}}{\partial x} + \frac{\partial \bar{v}}{\partial y} + \frac{\partial \bar{w}}{\partial z} \qquad (3.1.3)$$

and

$$\frac{\partial \bar{u}_i}{\partial t} + \bar{u}_j \frac{\partial \bar{u}_i}{\partial x_j} = - \frac{\partial \bar{p}}{\rho \partial x_i} + \frac{\nu \partial \bar{u}_i}{\partial x_i \partial x_j} - \frac{\partial \overline{u_i u_j}}{\partial x_j} \qquad (3.1.4)$$

The turbulent stresses of (3.1.4) will serve to accelerate ($\frac{\partial u}{\partial x} > 0$) and to decelerate ($\frac{\partial \bar{u}}{\partial x} < 0$) the fluid behind the grid members and in the open regions respectively. The natural symmetry of the grid and plate leads to planes of zero $\bar{v}$ and $\bar{w}$ and the conservation of mass equation can be used to infer non-zero $\bar{v}$ and $\bar{w}$ values between these planes in response to the observed $\partial \bar{u}/\partial x$ values. For example, for the $y = 0$ plane between two grid members (i.e., $\bar{v} = 0$ for all z), $\bar{w}$ is zero at the mid-plane of a horizontal rod, it is negative in the region between the plane of the rod and the center plane, and it is zero at the midplane between the rods. The presence of this mean motion following the passage of the grid suggests that convective transport effects are present in the actual experiment that would not be present if the idealized initial condition of homogeneous turbulence were obtained. The physical extent of the inhomogeneous region can be estimated from the experimental results of Sato and Yamamoto [1974]. Their hot-wire traverses downstream of a biplanar, round rod grid of solidity 0.44 (vs. 0.34 for the present study) indicate that homogeneity is obtained in approximately 3 mesh lengths. This corresponds to approximately the fourth scan for the present study.

The turbulence kinetic energy equation with $\overline{q^2} = \overline{u_i u_i}/2$

$$\frac{\partial \overline{q^2}}{\partial t} + \frac{\partial}{\partial x_j} \bar{u}_j \overline{q^2} = - \frac{\partial}{\partial x_j} \overline{u_j (q^2 + p/\rho)} - \overline{u_i u_j} \frac{\partial \bar{u}_i}{\partial x_j}$$

$$+ \nu \frac{\partial}{\partial x_j} \overline{u_i \left(\frac{\partial u_i}{\partial x_j} + \frac{\partial u_j}{\partial x_i} \right)} - \nu \overline{\frac{\partial u_i}{\partial x_j} \left(\frac{\partial u_i}{\partial x_j} + \frac{\partial u_j}{\partial x_i} \right)} \qquad (3.1.5)$$

makes explicit that the turbulence kinetic energy is generated in this initial inhomogeneous region and decays (balance of first and last terms) as a result of dissipation effects thereafter. The maximum magnitude of the turbulence kinetic energy can be

established in terms of the work done by the grid/splitter plate movement through the chamber. Let C_D be the drag coefficient for the physical structure used to create the turbulence field. The total work done is

$$W = \int \vec{F} \cdot \vec{ds}$$

Since $F_D = \frac{C_D \rho V_o^2 A_G}{2}$ and $\vec{ds} = \vec{V}_o \, dt$

$$W = \frac{\rho C_D A_G}{2} \int_o^{t_m} V_o^3 \, dt$$

here t_m is the time required to move the assembly across the chamber. Since the grid movement is controlled by the hydraulic actuator and since this motion is independent of the drag force acting on the grid, the initial kinetic energy states for the air and Freon gases will be in the ratio of their C_D values. Assuming that the C_D value is set by the grid elements, the data of Friehe and Schwarz [1970] can be used to establish the ratio

$$\frac{C_D\,[R_e = 6 \times 10^4]}{C_D[R_e = 10^4]} = \frac{\overline{q^2}_{avg}\ (t=0,\ Freon)}{\overline{q^2}_{avg}\ (t=0,\ air)} \cong 1.2 \qquad (3.1.6)$$

It is well known that in a parallel flow $\overline{u}^2$ is the turbulence velocity component which is first and predominantly energized by the destruction of the mean flow energy; see Corrsin [1957]. It is expected that this anisotropic condition is present in the current experiment. A very considerable data base is available for the flow behind biplanar grids. Comte-Bellot and Corrsin [1966] have summarized these results including those of Wyatt [1955] which are for a configuration very similar to that of the present study.

Following the establishment of a homogeneous turbulence field and prior to the final period of decay, the available experimental data suggest that a power law solution to (3.1.5) is appropriate. Comte-Bellot and Corrsin [1966] organize the experimental results in terms of

$$\frac{U_o^2}{\overline{u}^2} = A \left\{\frac{U_o t}{M} - \frac{U_o t_o}{M}\right\}^n \qquad (3.1.7)$$

which includes the presence of an apparent origin to account for the initial period of inhomogeneous turbulence. Using the data of Wyatt [1955] a graphical representation of the pertinent turbulence quantities in the present experiment has been prepared, see Figure 16.

Data for round rod, biplanar, grids show that the apparent origin (t_o) shifts to smaller values as the velocity is increased and mesh size is kept constant; see Comte-Bellot and Corrsin [1966]. Wyatt's data suggests that $\frac{U_o t_o}{M}$ decreases from 5 to 4 for a corresponding R_M range of 10^4 to 6×10^4. These are the relevant R_M for the present experiment. However, it is clear, from other data reported by Comte-Bellot and Corrsin, that well defined values of $\frac{U_o t_o}{M}$ do not exist.

In their study of the decay relations behind a biplanar grid, Comte-Bellot and Corrsin have reported that there was no apparent change in the decay laws for $\frac{H}{M} = 9$ and $\frac{H}{M} = 18$, where H represents the lateral dimension of the wind tunnel. The corresponding value for this experiment is $\frac{H}{M} = 18$. Uzkan and Reynolds [1967] have reported an experiment in which the decaying turbulence field was bounded (on one side) by a wall which moved at the free stream velocity U_o. The contamination of the interior turbulence by the wall effects is seen to proceed at a reduced rate for this condition. Their data show that it would require 54 seconds for the boundary influence to migrate 5 cm into the free stream at $R_M = 10^4$. Since times of less than 0.8 seconds are of interest in the present experiment, it is inferred that there is no influence of the boundaries on the measurements reported herein. Bradshaw (1977) has reported that experiments of this type are sensitive to the Reynolds number; however, the influence of the stationary wall will not influence either the Freon or the air results.

3.2. Scalar Concentration Field

3.2.1. The Ensemble Average Concentration Distribution

The transport equation for a scaler contaminant, C, is

$$\frac{\partial C}{\partial t} + \frac{\partial}{\partial x_j} u_j C = D \frac{\partial^2 C}{\partial x_j \partial x_j} \qquad (3.2.1)$$

where C is presumed to follow a Fickian law of diffusion. For

the present discussion, it is useful to consider the idealized condition in which $D \simeq 0$; this is closely approximated in the experiment as shown by the analyses in Section 4.

For the condition that $D = 0$, the mean concentration of the nondiffusive contaminant Γ (i.e., $\langle\Gamma\rangle$)† is given by

$$\frac{\partial\langle\Gamma\rangle}{\partial t} = -\frac{\partial}{\partial x_j}\langle u_j\rangle\langle\Gamma\rangle - \frac{\partial}{\partial x_j}\langle\dot{u}_j\gamma\rangle \qquad (3.2.2)$$

Since $\langle u_j\rangle \equiv 0$, except for the initial period of inhomogeneity, the expression for this restricted condition is of interest.

$$\frac{\partial\langle\Gamma\rangle}{\partial t} = -\frac{\partial}{\partial x_j}\langle\dot{u}_j\gamma\rangle = \frac{\partial}{\partial x_j}\left\{D_\tau \frac{\partial\langle\Gamma\rangle}{\partial x_j}\right\} \qquad (3.2.3)$$

In 3.2.3 the turbulent transport term is written as a product of the turbulent diffusivity and the gradient of the mean concentration field. This is based on an ad hoc analogy to molecular transport modeling, Corrsin [1974].

For the problem under consideration, namely, homogeneous turbulence, D_τ can be assumed to be independent of the direction of diffusion; consequently, (3.2.3) can be written as

$$\frac{\partial\langle\Gamma\rangle}{\partial t} = D_\tau(t)\frac{\partial^2\langle\Gamma\rangle}{\partial z^2} \qquad (3.2.4.a)$$

with boundary conditions

$$\begin{aligned}\langle\Gamma\ (z,0)\rangle &= 0\ ,\ z\leq 0\\ \langle\Gamma\ (z,0)\rangle &= 1\ ,\ z>0\end{aligned} \qquad (3.2.4.b)$$

The general solution of this equation in a semi-infinite region ($-\infty<z<\infty$) is given by Ozisik [1968].

$$\langle\Gamma(z,t)\rangle = \frac{1}{\left\{4\pi\int_0^t D_\tau(t')dt'\right\}^{\frac{1}{2}}}\int_{-\infty}^{\infty}\exp\left[-\frac{(z-z')^2}{\left\{4\int_0^t D_\tau(t)dt'\right\}^{\frac{1}{2}}}\right]\Gamma(z'0)dz' \qquad (3.2.5)$$

where $\Gamma(z'0)$ is the initial concentration distribution.

† Note that both $(\bar{\ })$ and $\langle\ (\ )\rangle$ will be used to designate an ensemble average of ( ).

The same result for $\langle\Gamma(z,t)\rangle$ can be obtained by an independent analysis which is due to Batchelor [1956]. This alternative development is considered in order to clarify the assumptions and restrictions which are used in each analysis.

For the conditions of homogeneous turbulence, without mean velocity gradients, it is reasonable to assume that the three-dimensional particle displacements follow a Gaussian distribution with standard deviations (x_p, y_p, z_p). The probability density function of the particle displacements is therefore

$$Q(x,y,z,t) = \frac{1}{(2\pi)^{\frac{1}{2}}} \frac{1}{(x_p^2 + y_p^2 + z_p^2)^{\frac{1}{2}}} \exp - \frac{1}{2} \{ \frac{(x-x')^2}{x_p^2} + \frac{(y-y')^2}{y_p^2} + \frac{(z-z'^2)}{z_p^2} \} \qquad (3.2.6)$$

For a scalar contaminant which indelibly marks the fluid element and for one whose presence is identified by $\Gamma = 1$ (and absence by $\Gamma = 0$), the ensemble average concentration distribution of the contaminant is directly related to the displacement of the original particle distribution as

$$\langle\Gamma(x,y,z,t)\rangle = \int_{-\infty}^{\infty}\int\int Q(x-x',y-y',z-z',t)\ \Gamma(x',y',z',0)\ dx'dy'dz' \qquad (3.2.7)$$

where $\Gamma(x',y',z',0)$ is the initial concentration distribution. For the experiment under consideration, the initial distribution of the contaminant occupies the volume $(x, y, z>0)$; therefore, $\langle\Gamma(x,y,z,t)\rangle = \langle\Gamma(z,t)\rangle$ and

$$\langle\Gamma(z,t)\rangle = \int_{-\infty}^{\infty} \frac{1}{(2\pi z_p^2)^{\frac{1}{2}}} \exp - \frac{1}{2} \{ \frac{(z-z')^2}{z_p^2} \} \Gamma(z',0)\ dz' \qquad (3.2.8)$$

This result suggests that the mean square displacement of a fluid particle, which represents the dispersive property

of the turbulence field, governs the behavior of the ensemble average concentration distribution. The mean square displacement can be developed using Lagrangian considerations; this development is presented in Appendix D.

The above equation is similar to (3.2.5), where by identity,

$$z_p^2 = 2 \int_o^t D_\tau(t')dt' \qquad (3.2.9.a)$$

or

$$D_\tau(t) = \frac{1}{2} \frac{d\, z_p^2}{dt} \qquad (3.2.9.b)$$

This result was observed by Hinze [1975]. Hence the turbulent diffusivity can be calculated from the time rate of change of the particle mean square displacement.

The mean concentration equation, (3.2.8), can be written in terms of the error function by defining new independent variables; see Ozisik [1968]. Let

$$\hat{\alpha} = \frac{z-z'}{(2z_p^2)^{\frac{1}{2}}} \quad \text{and} \quad dz' = (2\, z_p^2)^{\frac{1}{2}}\, d\hat{\alpha} \qquad (3.2.10)$$

Utilizing the boundary conditions from (3.2.4.a), the following expression is obtained for the ensemble average distribution; viz.,

$$\langle \Gamma(z,t) \rangle = \frac{1}{2} (1 + \text{erf}(z)) \qquad (3.2.11)^{\dagger}$$

For the experimental data under consideration a Gaussian cumulative distribution function which is identical to (3.2.8) will be used to describe $\Gamma(z,t)$, namely,

$$\langle \Gamma(z,t) \rangle = \frac{1}{(2\pi)^{\frac{1}{2}}\sigma_m} \int_o^z \exp - \frac{(\hat{\alpha}-\langle z \rangle)^2}{2\, \sigma_m^2}\, d\hat{\alpha} \qquad (3.2.12)$$

The separate symbols: σ_m and z_p, will be maintained to

†The error function of (3.2.11) is defined as

$$\text{erf}(z) = \frac{2}{\pi^{\frac{1}{2}}} \int_o^z \exp(-\hat{\sigma}^2)\, d\hat{\sigma}$$

respectively represent the best fit of a Gaussian C.D.F.† to the experimental data for $\langle\Gamma(z,t)\rangle$ and the standard deviation of the particle displacements in (the assumed Gaussian distribution of) the flow field.

The rate of transport of the marking contaminant across the midplane of the mixing chamber can be expressed in terms of the variables used in the above considerations. The ensemble average flux term of the contaminant across the midplane is $\langle w\gamma\rangle_{z=o}$ and, by using (3.2.3), (3.2.5) with the $\Gamma(z',o)$ given by (3.2.4.b), and (3.2.9.b), the expression for $\langle w\gamma\rangle_{z=o}$ becomes

$$\langle w\gamma\rangle_{z=o} = \frac{1}{(2\pi)^{\frac{1}{2}}} \frac{d\, z_p}{dt} \qquad (3.2.13)$$

The total flux of $\langle\Gamma\rangle$ during the elapsed time period $o \leq t' \leq t$ may be expressed as the integral of (3.2.13); viz.,

$$\int_o^t \langle w\gamma\rangle_{z=o} dt' = \frac{1}{(2\pi)^{\frac{1}{2}}} z_p \qquad (3.2.14)$$

3.2.2. The Ensemble Average Fluctuation Intensity Distribution

The mean square concentration fluctuation, $\langle c^2\rangle$, equation is

$$\frac{\partial}{\partial t}\langle c^2\rangle = -\langle u_j c\rangle \frac{\partial\langle c\rangle}{\partial x_j} - \frac{\partial}{\partial x_j}\langle c^2 u_j\rangle - D\left\langle \frac{\partial c}{\partial x_j}\frac{\partial c}{\partial x_j}\right\rangle - D\left\langle \frac{\partial^2 c^2}{\partial x_j \partial x_j}\right\rangle \qquad (3.2.15)$$

where $c = C - \bar{C}$ in which the turbulent effects serve to produce and convectively transport the concentration fluctuations (i.e., the first two terms on the right side of (3.2.15)) and the molecular effects destroy and diffuse the $\langle c^2\rangle$ by the action of the second two terms. In the absence of diffusion, i.e., for D = 0, a balance is possible if the production and transport are in balance. This condition occurs at the midplane of the mixing region as shown by the following analysis.

If D = 0, then the probability density function for Γ, $P_\Gamma(\alpha, t)$, can be represented by two Dirac functions at $\alpha = 0$

† Cumulative Distribution Function

and $\alpha = 1$ such that the mean value of Γ is obtained as

$$\langle\Gamma\rangle = \int_0^1 P_\Gamma(\alpha, t)\, \alpha\, d\alpha = P_\Gamma(1, t) \qquad (3.2.16)$$

The mean square fluctuation is

$$\begin{aligned}\langle\Gamma\rangle &= \int_0^1 (\alpha-\langle\Gamma\rangle)^2 P_\Gamma(\alpha,t)\, d\alpha \\ &= \langle\Gamma\rangle^2 P_\Gamma(o,t) -)1 -\langle\Gamma\rangle)^2 P_\Gamma(1,t) \qquad (3.2.17) \\ &= \langle\Gamma\rangle(1-\langle\Gamma\rangle)\end{aligned}$$

Hence, at the centerline, $\langle\gamma^2\rangle$ is constant for all time (since $\langle\Gamma\rangle = 0.5$); its value is 0.25.

Using the results of (3.2.17), $\langle\gamma^2\rangle$ can be written as

$$\langle\gamma^2\rangle = 0.25 \quad \{1 - \mathrm{erf}^2 \quad \frac{z}{(2z_p^2)^\pi}\} \qquad (3.2.18)$$

Measurements by Foss, Schlien and Corrsin [1972] in the mixing field downstream of a half-heated grid showed that the above estimate for the temperature fluctuation was 250% larger than the experimental data. Hence, the molecular diffusivity plays an important role in such flows even though the Gaussian C.D.F. of equation (3.2.8) was closely approximated by the experimental data for the mean temperature distribution. Analytical descriptions of the fluctuation intensity for the diffusive condition have been developed by Libby [1975] and the above investigators.

3.2.3. Dispersion Considerations

The $\Gamma(z,t)$ distributions which have been recorded in the present work represent the effects of turbulent transport. It is interesting to note that the non-diffusive nature of the sensed contaminant results in a direct correspondence between $\langle\Gamma(z,t)\rangle$ and the turbulent transport. This is in contrast with studies which use thermal tracers as the marking element. Taylor [1935] was the first to analytically describe such transport by the application of Lagrangian concepts. Using

v_i as the velocity of a fluid dynamic particle, the Lagrangian auto correlation for stationary turbulence can be expressed as

$$R_L = \frac{\langle v_i(t)\, v_i(t+\alpha)\rangle}{\langle v^2\rangle} \qquad (3.2.19)$$

and the mean square displacement of a fluid element from its point of origin in a stationary, homogeneous turbulence field is

$$\langle x_i^2\rangle = 2\langle v_i^2\rangle \int_o^t dt' \int_o^{t'} R_L(\alpha)\, d\alpha \qquad (3.2.20)$$

for stationary turbulence, the limiting cases of short time: $\tau \to 0, R_L(\alpha) = 1$ and $\langle x^2\rangle = 2\langle v^2\rangle t^2$ and of long time: $t \to \infty$, $\int_o^\infty R_L(\alpha)\, d\alpha = \Lambda$ and $\langle x^2\rangle = 2\langle v^2\rangle \Lambda t$, are of interest.

A turbulence field without mean shear will, of course, decay. If a tagged particle is released in such a field, its dispersion as a function of time will be influenced by the decay of the turbulence kinetic energy. A theoretical description of this physically realistic condition would require that the Lagrangian correlation function would specifically account for the decaying turbulence kinetic energy.

Falco [1972] made direct optical measurements of the velocity of small particles in the decaying turbulence field behind a biplanar grid in an enclosed water tank facility. From these measurements he obtained a (spherical) Lagrangian correlation at $\frac{U_o t}{M} = 89$ and 156. It is apparent from these measurements that there is a temporal growth of the Lagrangian scales as $\frac{U_o t}{M}$ increases; however, due to the sparse nature of the data (8 points for the correlation) it would be difficult to determine the quantitative features of this growth. Several authors, including Batchelor and Townsend [1956] and Shlien and Corrsin [1974], have formulated analyses to account for the decay of the turbulence energy and its relationship to the dispersion of a contaminant. A new version of such

an analysis is presented in Appendix D. The common feature of these analyses is the assumption of a self preserving state of the Lagrangian correlation function, $R_L(\tau)$, by the use of a stretched time coordinate, τ.† The equivalent results, for the mean square displacement, z_p^2, of a fluid particle for the short and long time special cases, are given below. The dispersion measure in the z direction of the present experiment, z_p^2, has been made nondimensional using the scale length L_p where

$$L_p^2 = \langle v^2(t_r - t_o)\rangle (t_r - t_o)^2. \qquad (3.2.21)$$

$$= \langle v^2(\Delta t_r)\rangle \ \Delta t_r^2 .$$

t_r is the "release time" for the tagged particle, t_o is the apparent temporal origin of the decaying turbulence and v is the Lagrangian velocity of the tagged particle. The short time result is, for

$$z^{*2} = \frac{z_p^2}{L_p^2} ,$$

$$z^{*2} = \frac{2}{(1-\frac{n}{2})^2}\left[\left(\frac{1}{2} - \left(\frac{1}{\tau^*}\right)^2\right)\left\{\left(\frac{\Delta t}{\Delta t_r}\right)^{2(1-\frac{n}{2})} + 1\right)\right\} + \left(\frac{\Delta t}{\Delta t_r}\right)^{(1-\frac{n}{2})}$$

$$\left[\left(\frac{1-\frac{n}{2}}{\tau^*}\right)^2 \ln^2\left(\frac{\Delta t}{\Delta t_r}\right) - 2\left(\frac{1}{2} - \left(\frac{1}{\tau^*}\right)^2\right)\right]\Bigg]$$

$$\text{for } \frac{\Delta t}{\Delta t_r} \leq \frac{\Delta t_j}{\Delta t_r} . \qquad (3.2.22)$$

Note, t_j and τ^* are defined below; (3.2.22) is also equation D.2.3. The long time result is

† This assumption was introduced by Batchelor and Townsend [1956].

$$z^{*2}\left(\frac{\Delta t}{\Delta t_r}\right) - z^{*2}\left(\frac{\Delta t_j}{\Delta t_r}\right) =$$

$$\frac{2}{(1-\frac{n}{2})^2}\left[\left(\frac{\Lambda^{*2}}{\Lambda^{*2}-1}\right)\left[\left(\frac{\Delta t_j}{\Delta t_r}\right)^{(1-\frac{n}{2})}\left(\frac{\Lambda^*-1}{\Lambda^*}\right) - \left(\frac{\Delta t}{\Delta t_r}\right)^{(1-\frac{n}{2})}\left(\frac{\Lambda^*-1}{\Lambda^*}\right)\right] +\right.$$

$$\left.\frac{1}{2}\left(\frac{\Lambda^*}{\Lambda^*+1}\right)\left[\left(\frac{\Delta t}{\Delta t_r}\right)^{2(1-\frac{n}{2})} - \left(\frac{\Delta t_j}{\Delta t_r}\right)^{2(1-\frac{n}{2})}\right]\right]$$

$$\text{for } \frac{\Delta t}{\Delta t_r} > \frac{\Delta t_j}{\Delta t_r} . \qquad (3.2.23)$$

The symbol n represents the decay exponent of the turbulence kinetic energy; see equation (3.1.7). The variables τ^* and Λ^* are defined as $\tau^* = \frac{\tau_L}{C_1}$ and $\Lambda^* = \frac{\Lambda}{C_2}$ where τ_L and Λ are the Lagrangian micro and macroscales in the stationary reference frame. Theoretical curves of 3.2.22 and 3.2.23 for various τ_L and Λ values are presented and discussed in Article 6.

The constants C_1 and C_2 are related to the temporal transformation in which the Lagrangian velocity correlation (3.2.19) is stationary; i.e., $\frac{\partial}{\partial t}(R_L(t,\tau)) = 0$. The temporal transformation which yields a stationary condition for $R_L(\tau)$ for $\tau \leq \tau_j$ is

$$\frac{\Delta t}{\Delta t_r} = \exp\left[\frac{\tau}{C_\lambda}\right] \qquad (3.2.24)$$

where $C_\lambda = (1-\frac{n}{2})C_1$. The similarly defined temporal transformation for $\tau > \tau_j$ is

$$\frac{\Delta t}{\Delta t_r} = \exp\left[\frac{\tau}{C_\int}\right] \qquad (3.2.25)$$

where $C_\int = (1-\frac{n}{2})C_2$. The symbols Δt, Δt_r and Δt_j are the times referenced to the temporal origin as $\Delta t = t-t_o$, $\Delta t_r = t_r-t_o$, and $\Delta t_j = t_j-t_o$. The symbol τ_j represents the

juncture point between the short and long time formulations. Figure 16b shows a graphical representation of these concepts. The following relationship defines the juncture point in the $\frac{\Delta t}{\Delta t_r}$ reference frame:

$$1 - \left(\frac{1-\frac{n}{2}}{\tau^*}\right)^2 \ln^2\left(\frac{\Delta t_j}{\Delta t_r}\right) - \left(\frac{\Delta t_j}{\Delta t_r}\right)^{-\left(\frac{1-\frac{n}{2}}{\Lambda^*}\right)} = 0 \qquad (3.2.26)$$

The Lagrangian macroscale, Λ, is a property of the turbulence field and is clearly related to the dispersive character of a turbulent flow. Previous experimental efforts to determine the dispersion have made use of a passive scalar contaminant such as a low overheat thermal marker. In these studies, temperature tagging wires mark a spot or line of the fluid and downstream temperature measurements define the mean temperature as a function of the transverse distance. The value z_p^2 is inferred from the latter. Such studies have been performed by Uberoi and Corrsin [1953], Townsend [1956], and Shlien and Corrsin [1974]. The last authors provide a well developed scheme for interpreting the influence of the decaying non-stationary condition of the turbulence. The influence of the non-zero diffusivity of the thermal energy in such experiments has been theoretically examined by Saffman [1961]. Saffman's analysis, which is limited to small times from the initiation of the mixing, provides a corrective interpretation to the earlier Townsend [1956] analysis which had served a similar purpose for the original work of Taylor [1935]. Chevray [1977] has developed an alternate analytical structure which extends the prior results of Saffman. Qualitatively, the present investigation is as if the marking contaminant were impressed upon a region, instead of a line or spot, of the host fluid.

3.2.4. Fourier Transform Considerations

A useful description of the scalar concentration field can be gained by the use of Fourier transforms. Let the

function $B(\vec{k})$ represent the amplitude of the wave which is related to the spatial distribution of $\Gamma(\vec{x})$ as

$$B(\vec{k}) = (2\Pi)^{-3} \iiint_{-\infty}^{\infty} \Gamma(\vec{x}) \exp(-i\, \vec{k}\cdot\vec{x})\, d\vec{x} \qquad (3.2.27)$$

Similarly, the velocity component u_n can be transformed to a wave description as

$$F_n(\vec{k}) = (2\Pi)^{-3} \iiint_{-\infty}^{\infty} u_n(\vec{x}) \exp(-i\vec{k}\cdot\vec{x})\, d\,\vec{x}. \qquad (3.2.28)$$

Operating on the conservation equation for Γ results in (see, eg. Yeh and Van Atta [1973])

$$\frac{\partial}{\partial t}[\tfrac{1}{2}\phi(\vec{k})] = -i\, k_j \iiint T_n(k, k')\, dk' - D\, k^2 \phi_n(k) \qquad (3.2.29)$$

where $\phi = \langle BB^* \rangle \Delta k^3$ which represents the intensity of the concentration fluctuation at wave numbers $k_i \pm \Delta k_i/2$. (B^* is the complex conjugate of B.) The function $T_n(k, k')$ represents the transfer of the fluctuation intensity to higher wave numbers; formally, it can be expressed as:

$$T_n(k) = \tfrac{1}{2} i (\Delta k)^3 k_i \langle F_n^*(k - k') B^*(k')\, B(k) - F_n(k-k')\, B^*(k)\, B(k') \rangle \qquad (3.2.30)$$

This transfer term is responsible for enriching or transferring energy ($\phi(k)$) to large values of k. Its effect is limited by the presence of the last term in (3.2.11) in which the concentration fluctuations are "smoothed" by the diffusive action of the molecular diffusivity. For the idealized experiment involving D = 0, the striations of the mixed regions will become of finer and finer scale. Batchelor [1959] has developed a theoretical description of the scalar field for the condition of small conductivity (diffusivity). His work shows that the $\phi(k)$ spectra falls off at the lesser slope of k^{-1} beyond the break where $F_n(\vec{k})$ changes from a -5/3 to a region of more rapid decay. Gibson and Schwarz [1963], Nye and Brodkey [1967], and Grant & Nisbet [1957] have observed the k^{-1} behavior in : i) salt concentration and temperature measure-

ments, ii) dye, and iii) temperature measurements respectively. Interestingly, there was no significant difference between the salt and heated water results in the Gibson and Schwarz experiment.

4. DYNAMIC BEHAVIOR OF THE MARKING PARTICLES

The previous sections have identified the basic premise of the experimental technique: that a marking contaminant may be found which faithfully moves with the same continuum fluid element from the initiation to the termination of the experiment.* The contaminant particle selected must be sufficiently large that it is not displaced from the continuum element by the random agitation of the molecular motion and it must be sufficiently small that it does not: i) follow an inertia dominated trajectory and thereby define a pathline which is different from that of the continuum element of its origin, ii) influence the density or stability properties of the fluid, or iii) fall away from the continuum element under the action of the gravitational force.

The following subsections consider these effects based upon air as the host fluid for submicron particles ($a = 0.25\mu m$) of specific gravity 1.0.

4.1. Aerodynamic Drag

The equation which describes the motion of the fluid element and the corresponding response of the particle has been analyzed by Tchen [1947], Hinze [1975], Corrsin and Lumley [1956] and Soo [1967]. The following equation was extracted from Khosla and Lederman [1973].

$$\frac{du_{p_i}}{dt_p} = \frac{3\rho}{2\rho_p+\rho}\left[\frac{du_i}{dt} - \frac{2}{3}\nu\frac{\partial^2 u}{\partial x_j \partial x_j}\right] + \frac{2}{\rho+\rho_p}\left[\frac{9\mu}{2a^2}(u_i-u_{p_i}) + \rho(u_k-u_{p_k})\frac{\partial u_i}{\partial x_k}\right] + \frac{9}{(2\rho_p+\rho)a}\left(\frac{\rho\mu}{\pi}\right)^{\frac{1}{2}}\int_{t_r}^{t_p}\frac{\frac{d}{d\tau}(u_i-u_{pi})}{\sqrt{t_p-\tau}}\,d\tau \qquad (4.1.1)$$

where u_{p_i} is the vector velocity of the particle, u_i is the velocity of the gas, ν the coefficient of kinematic viscosity, μ the coefficient of viscosity, ρ_p the density of the solid

*Becker [1977] identified this technique as "marker nephelometry"

PRECEDING PAGE BLANK

material and a is the radius of the particle. Tchen assumes that the particle radius is small and

$$\frac{u_{p_i}}{a^2 \frac{\partial^2 u_i}{\partial x_j \partial x_j}} >> 1 \qquad (4.1.2)$$

The most restrictive assumption made by Tchen is that during the motion of the particle, the same fluid element remains in its neighborhood. Thus he postulates

$$\frac{d}{dt_p} \simeq \frac{d}{dt} \, . \qquad (4.1.3)$$

This assumption is required for a solution to be realized so that one can achieve an estimate of the phase lag as well as amplitude decrease. Since this equation is linear, a one-dimensional velocity field will be considered and the effects of self-diffusion and gravity can be obtained by a separate analysis. The resulting expression for the particle motion is

$$\frac{du_p}{dt} = \beta \frac{du}{dt} + \alpha\beta (u - u_p) + \beta \left(\frac{3\alpha}{\pi}\right)^{1/2} \int_{t_r}^{t} \frac{\frac{d}{d\tau}(u - u_p)}{\sqrt{t-\tau}} \, d\tau \qquad (4.1.4)$$

where $\alpha = \frac{3\nu}{a^2}$ and $\beta = \frac{3\rho}{(2\rho_p + \rho)}$

This equation was solved by Chao [1964] using Fourier transform techniques, which allows the time dependent character of the velocity field to be expressed as a frequency fluctuation (ω). The Fourier transform of the velocity is

$$u(\omega) = \int_{-\infty}^{\infty} u(t) \exp(-i\,\omega t) \, dt. \qquad (4.1.5)$$

The solution for the particle velocity as a function of the fluctuation frequency is

$$u_p(\omega) = \frac{\{1 + [1.5\omega/\alpha]^{\frac{1}{2}} + i(\omega/\alpha + [1.5\omega/\alpha]^{\frac{1}{2}})\} \, u(\omega)}{\{1 + [1.5\omega/\alpha]^{\frac{1}{2}} + i(\omega/\alpha\beta + [1.5\omega/\alpha]^{\frac{1}{2}})\}} \qquad (4.1.6)$$

By multiplying the velocities u_p and u by their respective complex conjugates and introducing the energy spectrum density function $F(\omega)$, a relation is obtained between the intensity of the particle motion and that of the surrounding fluid.

$$\langle u_p^2 \rangle = \langle u^2 \rangle \int_o^\infty \frac{\Omega^{(1)}}{\Omega(2)} \quad F(\omega)\, d\omega$$

$$\Omega^{(1)} = \left(\frac{\omega}{\alpha}\right)^2 + \sqrt{6}\left(\frac{\omega}{\alpha}\right)^{3/2} + 3\left(\frac{\omega}{\alpha}\right) + \sqrt{6}\left(\frac{\omega}{\alpha}\right)^{1/2} + 1 \qquad (4.1.7)$$

$$\Omega^{(2)} = \frac{1}{\beta^2}\left(\frac{\omega}{\alpha}\right)^2 + \frac{\sqrt{6}}{\beta}\left(\frac{\omega}{\alpha}\right)^{3/2} + 3\left(\frac{\omega}{\alpha}\right) + \sqrt{6}\left(\frac{\omega}{\alpha}\right)^{1/2} + 1$$

The ratio $\{\langle u_p \rangle / \langle u^2 \rangle\}$ can be used to infer the ability of the particle to move with an accelerating fluid element. This ratio is presented in Figure 17 as a function of the oscillation frequency ω for the conditions: d = 0.25, 0.5, 1, 2μm), ρ_p = 1gm/cc, $\rho = \rho_{air}$ (STP)). One can infer from the above results that a 0.5 mm particle will follow the flow with a time scale of the order of one micro-second. Using the data of Wyatt at x/M≈10, the Kolmogoroff time scale $(\nu/\varepsilon)^{1/2}$ has a minimum value of 10^{-3}sec. Hence, the .5μm particle is expected to follow the most rapid fluctuations to be found in the physical flow field.

Further insight into the aerodynamic drag effects can be gained by considering the behavior of a particle in a swirling flow which simulates the motion of the small scale eddies. Hirschkron and Echrich [1964] have analyzed the motion of a particle in an irrotational vortex ($u_\theta = c_v/r$). The salient features of this analysis are presented in the following.

A spherical particle is assumed and the analysis is restricted to the low Reynolds number, "Stokes Flow" regime. The drag coefficient c_D is given as

$$c_D = \frac{12}{\rho\,|[\vec{u}-\vec{v}]|\,a} \qquad (4.1.8)$$

where $\vec{u}$ is the fluid velocity, $\vec{v}$ is the particle velocity, and a is the particle radius. The expression for the drag force F is

$$\vec{F} = \frac{1}{2} C_D \rho(\vec{u} - \vec{v}) \cdot (\vec{u} - \vec{v}) \pi a^2$$

$$m_p \frac{d\vec{v}}{dt} = 6\pi\mu a [\vec{u} - \vec{v}] \qquad (4.1.9)$$

The fluid velocity field is assumed to be that of an irrotational vortex:

$$\vec{u} = \hat{\theta} C_v/r \qquad (4.1.10)$$

The acceleration of the particle can be written in terms of the spatial variations of the velocity field as

$$v_r \frac{dv_r}{dr} - \frac{v_\theta^2}{r} = -P v_r$$

$$v_r \frac{dv_\theta}{dr} + \frac{v_r v_\theta}{r} = P\left[\frac{C_v}{r} - v_\theta\right] \qquad (4.1.11)$$

where $P = (6\pi\mu a/m_p)$.

These equations were solved numerically and the results were plotted in normalized form. The radial position (r/r_o) of the particle as a function of time $(t\, C_v/r_\varepsilon^2)$ is of interest for the small scales of the motion. Choosing an eddy of the Kolmogoroff size

$$r_\varepsilon = (\nu^3/\varepsilon)^{1/4} = 0.123\text{mm} \qquad (4.1.12)$$

where $\varepsilon = 14.7\ m^2/sec^3$ at $t = 0.04$ sec for $\nu = 1.5 \times 10^{-5} m^2/sec$. The ε value is evaluated from the data of Wyatt [1955]. The kinetic energy of the dissipative eddies is approximated by $q = (\nu\varepsilon)^{1/2}$: consequently, a characteristic value of u_θ is given by $u_\theta(r_\varepsilon) \tilde{=} 0.122$ m/sec. The above value for $u_\theta(r_\varepsilon)$ allows C_v to be evaluated as: $C_v = 15\ mm^2/sec$. Making use of the Hirschkron and Echrich solution for a 0.5-μm particle in air, r/r_ε does not exceed 1.2 for an elapsed time of 1.0 second. The experimental times of interest are shorter than this; it is again inferred that the particle suitably follows the fluid motion.

4.2. Gravitational Effects

The terminal velocity is calculated using the Stokes drag relationship giving

$$V_T = \frac{2}{9} \frac{\rho_p}{\mu} a^2 g \qquad (4.2.1)$$

For a 0.5-μm particle with specific gravity 1.0, V_T = 0.05 mm/sec. The distance travelled by the particle in the elapsed time of the experiment is an order of magnitude smaller than the Kolmogoroff scales.

4.3. Particle Diffusion by Molecular Agitation

The random molecular motion in the neighborhood of the particle will cause it to move away from the spatial volume of its origin. In the presence of a fluid velocity (i.e., a drift velocity of the molecules) this motion would be with respect to the convected spatial volume which is defined at the initiation of the experiment. The characteristics of the motion can be assessed by kinetic theory considerations as shown in the following.

The root mean square velocity of a particle of mass m is given in terms of the Boltzman constant K_B and the absolute temperature T as

$$\tilde{v} = \left\{ \frac{3K_B T}{m_p} \right\}^{1/2} \qquad (4.3.1)$$

For a 0.5-μm particle of specific gravity 1.0 and for 300°K, $\tilde{v}$ = 4.6 mm/sec. This velocity is small ($\lesssim$ 1 percent) with respect to the rms continuum fluid velocities of interest in the present experiment.

The displacement of the fluid particle can be evaluated from the diffusion coefficient, D_p. It is defined by the expression

$$D_p = \frac{K_B T}{6\pi\mu a} \qquad (4.3.2)$$

For the conditions of a 0.5-μm particle (a = 0.25 μm) with 300°K air as the host fluid,

$$D_p = 6.7 \times 10^{-11} \text{ m}^2/\text{sec}$$

In order to relate D_p to the displacement of the marking particles, consider a field of particles in which the particle concentration c is initially given as

$$c(z,o) = c_o \text{ for } z \leq o$$

$$c(z,o) = o \text{ for } z > o$$

and in which the particle concentration c follows the Fickian law of diffusion:

$$\frac{\partial c}{\partial t} = D_p \frac{\partial^2 c}{\partial z^2} \tag{4.3.3}$$

The resulting concentration field for D_p = constant is given as

$$\frac{c}{c_o} = 1 - \text{erf} \frac{z}{\sqrt{4D_p t}} \tag{4.3.4}$$

A width measure for the migration of the particles can be specified as

$$\delta_\rho = 4\sqrt{D_p t} \tag{4.3.5}$$

For the conditions used above, δ_p = 0.047 mm for an elapsed time of 1.0 sec ($\frac{u_o t}{M} \simeq 250$). Hence the migration of the particles in one second is 0.134 times the scattering volume dimension. This gives credence to the assumption that the contaminant is "non-diffusive".

4.4. Influence of Particles on Carrier Gas Properties

The experimental technique of marking a given spatial volume requires a substantial number ($\simeq$20)* of marking particles. The influence of these particles on the carrier (or host) gas is considered in the following.

For a concentration of 10^6, 0.5-μm diameter particles/cc, the density increase with respect to the uncontaminated air is 0.1 percent. The influence on the viscosity can be assessed from the Einstein equation; (see Hirschfelder, Curtiss and Bird [1954]) $\mu = \mu(1 + \phi)$ where ϕ is the volume ratio. The

*The particles may be assumed to follow a Poisson distribution as regards their distribution in the spatial volumes. Hence, the standard deviation of the particle number per element is $N^{-\frac{1}{2}}$ where N is the average value. Consequently, N should be large to maintain an unambiguous scattering signal.

change in viscosity as a result of the additional particles is 10^{-4} percent.

The influence of the particles on the hydrodynamic stability of the host fluid has been considered by Saffman [1961]. His results can be used to infer that there is a negligible influence on the stability resulting from the presence of these 0.5-μm diameter particles in air.

5. RESULTS

5.1 Flow Visualization

The motion of the gas inside the mixing chamber was photographically recorded; a significant feature of the initial motion was revealed by this procedure. Marking particles, with a concentration of 10^6 particles/cc, were initially introduced in the upper volume;† they were illuminated by a light sheet formed with a cylindrical and spherical lens system. The motion pictures were taken at 50 frames/sec; the exposure time was 150^{-1} sec. The first visible frame could not be precisely correlated with the passage of the grid; it represents an experimental time of 0-0.02 seconds. Representative frames are shown in Figure 18. The black/white (or marble cake) mixing character of the particle gas is apparent albeit some resolution is undoubtedly lost with the grain of the film and the relatively long exposure time.

The first frame of Figure 18 is considered to be quite significant. Specifically, the "fuzzy" end of the marked particles in the 0-0.02 sec. time span was not anticipated; it suggests a rapid mixing in the neighborhood of $z = 0$ which precedes the large scale mixing induced by the grids. The source and character of this initial mixing process has been determined.

The boundary layers which grow upon and which are shed from the splitter plate form a wake of positive and negative vortex sheets. In addition, the regular vortex structures shed from the horizontal cylinders of the biplane grid will create an organized perturbation of the vortex sheets. The antisymmetric part of the perturbation leads to an instability of the vortex sheets with a subsequent roll up or amalgamation of the vorticity into vortex clouds. Abernathy and Kronauer [1962] have computed the behavior of these vorticities. Their nonlinear analysis shows that the vortex sheets are unstable to any wavelength disturbance and that the clouds may be comprised of opposite sense vorticity with a consequent reduction in the net strength of the vortex cloud.

† The particles were introduced into the lower half volume for the quantitative experiments.

PRECEDING PAGE BLANK

The spacing of the regular vortex structures shed from the horizontal rods can be determined from the data of Roshko [1954] and the conditions of the present experiment. The pertinent Reynolds number is

$$R_n = \frac{U_o d}{\nu} \approx 2000 \qquad (5.1.1)$$

and, from Roshko, the corresponding Strouhal number is

$$S_T = \frac{f_\lambda d}{U_o} = \approx 0.2 \qquad (5.1.2)$$

The wavelength of the disturbance can be calculated from f_λ as

$$\lambda = U_o/f_\lambda = d/0.2$$
$$\approx 2.54 \text{ cm} \qquad (5.1.3)$$

From Schlicting (1968), the impulsively started boundary layer δ grows as

$$\delta = 4\sqrt{\nu t} \qquad (5.1.4)$$

The elapsed time t is the time required for the grid to move one half of its total travel across the box; the resulting value for δ is $\approx$2.54 mm. The splitter plate is approximately 1.56 mm thick and assuming that the laminar boundary layer vorticity is concentrated at ($\approx\delta/3$), the h value is $\approx$3.26 mm. Hence $h/\lambda \approx 0.13$.†

Abernathy and Kronauer present the formation of the vortex clouds for $h/\lambda \geq 0.12$. As shown by the figure, the "mixing" is quite advanced for a unit value of the dimensionless time tU'/λ, where U' is the velocity parameter introduced by Abernathy and Kronauer. (U'= plate velocity/2.) Consequently, the time to achieve significant mixing (or dispersion of the two gases in the neighborhood of y = 0) is given by

$$t = \lambda/U' \approx 0.007 \text{ sec.} \qquad (5.1.5)$$

†Figure 19 shows a schematic representation of the parameters in the initial mixing field.

Significantly, this elapsed time is quite small with respect to the time scales which characterize the subsequent mixing; specifically, the minimum Kolmogorov time in the homogeneous turbulence field is $\approx$ 5 msec. Also, the 7 msec to establish the initial mixing layer is comparable with the elapsed time (3.5 msec) between two successive scans. Consequently, the experimental technique will adequately identify the structure of this mixed region once it is formed, but it will not be able to document its evolution.

The analysis of Abernathy and Kronauer show that the mixed region is four to five times the original separation distance h. Consequently, the initial conditions for the quantitative evaluation of the mixing--as controlled by the large-scale motions--will be a lower region of contaminated gas and an upper, uncontaminated gas, region separated by a well stirred region of height $\approx$0.5M.

The smaller kinematic viscosity of the Freon gas suggests that the initial displacement of the two vortex sheets will be smaller than the displacement for the air case. The impulsively started boundary layers will be reduced by the multiplicative factor $[\nu_F/\nu_{air}]^{1/2} \approx \frac{1}{2.4}$. This suggests that the initial width measure for the Freon results should be smaller; this point is addressed in the next section.

The later times in Figure 20 and 21 show the mixing for longer time periods. It is evident from these pictures that the interface is highly convoluted and stretched by the turbulent strain field.

5.2 Data Base for the Particle Experiments

The "non-diffusive mixing" experiments are achieved by contaminating the lower volume (gas B) with a cloud of submicron particles whose dimensions are: (1) sufficiently large that they are not significantly influenced by the Brownian motion of the surrounding gas molecules and (2) sufficiently small that their "slip velocity" with respect to the continuum motion is negligible. The nominal diameter of the particles, viz., 0.5μm satisfies these joint criteria. The turbulent transport in the chamber is revealed by the presence of B in the upper half volume and that of A in the lower volume. Parenthetically, it can be noted that the incompressible nature of the mixing experiment requires that the volumes of the two gases are invarient with respect to time; however, this fact cannot be readily used in the interpretation of the data since information from only one spatial line is available and because sub-scattering volume mixing may be present which would yield an excessive estimate for the presence of B. In principal, the presence of B in the scattering volume is easily detected. The light scattering from the particles (of B) creates a photomultiplier tube output signal which is many times that for the noncontaminated gas. A comparator circuit readily distinguishes the two states (a nominal signal/noise ratio $\geq$ 10 was achieved) and creates a binary pulse train with a "0" indicating the presence of A and a "1" indicating the presence of B.

The electronics processing circuitry converted the pulse train, from the comparator circuit, into data words which were compatible with the TI minicomputer. The data was then transferred to digital magnetic tape for further processing on the CDC 6500 central computer.

The experiments were carried out with air as the working medium for 69 realizations and with Freon 12 for 100 realizations. The marking particles were placed in the lower half volume for all cases. A 74 mm scan was provided by the mimification of the optical system and there were 205 readings per

scan; hence, each data point was sampled from some fraction of a 0.36 mm section of the laser beam in the mixing chamber. The nominal scattering volume height (h) may be estimated from the slit width (w), the magnification ratio (M) and the angle of intersection between the slit and the vertical laser beam (ψ). Specifically, $h = [w/M \cos \psi] \cong [0.25/1.36 \cos(\pi/4)] = 0.26$ mm. The actual probe volumes were both somewhat larger and smaller than this nominal value; however, less than 1 percent of the scattering volumes exceeded the 0.36 mm spacing noted above and consequently they can be considered to be non-overlapping. The scans were executed in 3.11 ms; the period of the scans was 3.5 ms. The designated scan number is precisely known from the data record; however, its time, relative to the passage of the grid, is uncertain since there was no coupling between the initiation of the scan and the grid motion. Consequently, the designated time should be understood as $\frac{U_o t}{M} = 0.433$.

The data base which results from these experiments is represented by the \$/blank map shown in Figure 15. The presence of gas B, as marked by the particulate matter, is represented by "\$", the presence of the unmarked fluid A, is signified by a "blank" space. The map represents data for every other location (up to location 200) in keeping with the lateral dimension from the line printer. The quantitative results make use of the complete set of 205 locations. The interpretation of the experiments requires a careful examination of numerous aspects of the physical processes in the chamber and the details of the data acquisition process; these matters are dealt with in the following sections. Similar maps for stable and unstable cases involving Freon 12 and air are presented in Appendix C. A map showing a complete set of 240 scans for an air/air case is also presented in this appendix.

5.3 Ensemble Average Distributions

The experimental results for the ensembles of 69 and 100 realizations of the air and the Freon 12 gases are considered in this section. The instantaneous concentration of gas A or B at a given location and at a given time from the initiation

of the experiment is termed $\Gamma(z,t)$; for the non-diffusive experiments its possible values are 0 or 1. The ensemble average values of Γ are identified as $\langle\Gamma(z,t)\rangle$ and such values have been evaluated for a discrete set of times corresponding to scans (1, 2, 4, 6, 8, 11, 14, 17, 21, 25, 29, 33, 37, 41, 60, 80, 100, 120, 140, 160, 180, 200, 220).

Since the mixing field for the neutral density condition is at least expected to be symmetric, and since the turbulent transport effects in a homogeneous turbulence field are known to be readily approximated as a Gaussian process, a normal distribution was examined as a way to characterize the lateral distribution of the ensemble average values. Analytical considerations regarding the use of the normal distribution have been presented in Section 3.2. The data were found to follow such a distribution, at least for a first approximation, and the subsequent evaluation of the data will rely upon the parameters of the normal distribution to provide reference quantities for the spatial distributions of the average concentrations.

A representative data set is presented in Figure 22. The dimensional plot $\langle\Gamma(z,t)\rangle$ is shown in part (a); the solid curve of this figure is the normal distribution found by a linear least squares fit to the representation of the data on the "probability coordinates" of part (c). The probability coordinates are "defined" in part (b). The standardized normal cumulative distribution function, defined as

$$A(\xi) = \frac{1}{(2\pi)^{\frac{1}{2}}} \int_{-\infty}^{\xi} \exp\left(-\frac{\hat{\alpha}^2}{2}\right) d\hat{\alpha} \qquad (5.3.1)$$

see Dubes [1968], is shown on part b. The coordinate transformation

$$\xi = \sigma_m^{-1} (z - z_c) \qquad (5.3.2)$$

related the standard Gaussian distribution to the ensemble average concentration distribution, $\langle\Gamma(z,t)\rangle$. The symbol z_c

represents the centerline of this distribution; i.e., $\langle\Gamma(z_c,t)\rangle = 0.5$. σ_m represents the standard deviation of the spatial distribution; i.e., $\langle\Gamma(z_c \pm \sigma_m, t)\rangle = 0.5 \pm 0.34$. The standard deviation σ_m represents a convenient width measure of the distribution. Figure 23 represents the ensemble average data $\langle\Gamma(z,t)\rangle$ and Figure 24 shows the resultant transformation onto probability coordinates for Freon and air at $U_o t/M = 12$. Note, that z_c is different from the centerline of the mixing chamber (z_m). Apparently, this is a result of large scale gross transport of the mixing region. It is assumed that this transport does not directly effect the turbulent mixing near the centerline from which σ_m is calculated. The essential features of the ensemble average data are represented by straight lines on probability coordinates; see Figures 25 and 26 for a composite representation of the air and Freon 12 results. The standard deviation between the cumulative distribution function and the experimental data are also shown in the tables included with these plots.

The width measures, σ_m, for the Freon and air data are shown in Figure 27. This figure also shows the physical size of the round rod and the mesh size of the biplane grid. The evolution of the mixing field within the chamber is shown in Figure 28. The spatial locations of $\langle\Gamma\rangle = 0.15$ and $\langle\Gamma\rangle = 0.85$ are used to mark the "boundaries" of the mixing field as a function of the elapsed time from the initiation of the experiment ($U_o t/M$).

5.4 Measures of the Instantaneous Scans

The individual measurements of $\Gamma(z,t)$ in the "instantaneous" scans of the turbulent mixing field represent a very considerable amount of information which is only partially characterized by the ensemble $\langle\Gamma(z,t)\rangle$ distributions. Insight into the detailed structure and processes of the mixing field can be gained if suitable measures of the instantaneous scans can be formulated. One such formulation has been achieved; it is described below.

Consider two extreme cases for the instantaneous concentration field; both are capable of yielding the observed $\langle\Gamma(z,t)\rangle$ following the ensemble average process. The two cases are introduced in the form of statements. "The instantaneous concentration field is such that an instantaneous scan reveals:

Case 1. a well mixed field with transverse dimension and concentration $\Gamma(z,t)$ "similar" to that of $\langle\Gamma(z,t)\rangle$."

Case 2. a relatively thin mixed region (i.e., one which is small, for example, with respect to $\sigma_m(t)$) which is laterally transported by the convective action of the large scale turbulent motion to yield the observed $\langle\Gamma(z,t)\rangle$ distribution."

It is not expected that either of these models will be supported in their extreme condition; however, they do serve as a guide for the definition of measures to evaluate the character of the instantaneous scans. Specifically, definitions for i) the center of the instantaneous scan and ii) the width of the mixed region about the instantaneous center are required. The two definitions are separately considered in the following; the center of the instantaneous scan is defined by the following operations.

a.) Determine the number of blanks (or absences - A) which signify the presence of fluid A in the scattering volumes and designate this number as NA. Similarly, identify the number of filled regions and designate this number as NB (NB=205-NA).

b.) The center of the instantaneous scan will be designated as the position along the scan where the number of scattering volumes between the uppermost position of the scan and the instantaneous center is equal to NA.

Note that this definition implicitly assumes that the B fluid does not extend beyond the upper limit of the scan and

that the A fluid does not extend beyond its lower limit. Also note that the upper and lower designations are understood in terms of the physical experiment; in terms of the $(≡ B) map of Figure 15, "uppermost" corresponds to "leftmost". A schematic representation of the above operations is provided in Figure 29.

The position of the instantaneous center for the ith scan and for jth experiment will be designated as $z_{ci})_j$. The location of the average of the instantaneous centerlines $\langle z_{ci} \rangle$ and its displacement from the ensemble average centerline, $\langle z_{ci} \rangle - \langle z_c \rangle$ (see Figure 29), are of interest. The statistical characteristics of the $z_{ci})_j - \langle z_{ci} \rangle$ values allow one feature of the two cases to be assessed; namely, if the variation of the centerline position is large (with respect to σ_m for example) then support for case 2 is inferred. The standard deviation of the $z_{ci})_j - \langle z_{ci} \rangle$ population is defined as

$$\sigma_{\Delta z)_i} = \left\{ \frac{1}{N-1} \sum_{j=1}^{N} [z_{ci)_j} - \langle z_{ci} \rangle]^2 \right\}^{\frac{1}{2}} \qquad (5.4.1)$$

where N is the total number of experiments. The quantity $\sigma_{\Delta z}$ is compared with σ_m in Figure 30a and 30b; the interpretation of these results is discussed in the next section.

The width of the mixed region about the instantaneous scan can be assessed in a manner quite similar to that of the width measure for the ensemble averages. (This will offer the subsequent advantage of a basis for the comparison of their relative magnitudes.) Specifically, the emsemble average of the Γ field <u>with respect to</u> $z_{ci})_j$ was formed as

$$\langle \Gamma(z - z_{ci}) \rangle = \frac{1}{\eta} \sum_{j=1}^{\eta} \Gamma(z - z_{ci})_j) \qquad (5.4.2)$$

where $\eta \leq N$ and η represents the number of experiments which possess a measured value of Γ at the z location in question. The $\langle \Gamma(z - z_{ci}) \rangle$ so evaluated were then fit with the normal

distribution as described by equations 5.3.1 and 5.3.2. The resulting value of the width measure is termed $\sigma_I)_i$; the values of $\sigma_I)_i$ for the 69(air/air) and the 100(Freon 12/Freon 12) experiments are compared with the width measure of the ensemble average scans, $\sigma_m)_i$, in Figures 30a and 30b. These results are discussed in the next section.

6. DISCUSSION OF RESULTS

6.1. The Ensemble Average Concentration Distributions

Figures 25, 26, and 27 represent the primary documentation of the experimental results for the ensemble average concentration distributions. These figures include a tabulation of the standard deviation (S.D.) values which indicate the validity of representing the ensemble average data with a Gaussian Cumulative Distribution Function (C.D.F.).† The S.D. values are computed from the relationship between $\langle\Gamma(z,t)\rangle$ and the C.D.F. in the range $0.03 \leq \langle\Gamma(z,t)\rangle \leq 0.98$. These limits reflect the relatively small sample size, and hence the limited resolution, of the experimental data (1:69 air and 1:100 Freon 12) and are selected such that the σ_m and z_c values are "minimally" effected by the selection of an arbitrary segment of the experimental data. (Trial runs on one data set show only a nominal influence of the cut-off values on σ_m; specifically, σ_m for $U_o t/M = 18$ did not change by more than 2% when cut-offs representing 0.014 - 0.986, 0.028 - 0.972, and 0.043 - 0.957 were examined.) The relatively small values of S.D. (compared to unity) suggest that the Gaussian C.D.F. provides, at least, a satisfactory representation of the experimental data. Since this analytical form is also supported by: (i) the (assumed) Gaussian displacement of fluid elements, see [3.2.6], and (ii) (independently) by an assumed "D_T = constant" model of the turbulent transport, see [3.2.5], this compact presentation of the $\langle\Gamma(z,t)\rangle$ results is both efficient and apparently justified.

The experimental data reveal that the σ_m values for the air experiments are larger than the σ_m values for the Freon 12 experiments at a given $U_o t/M$. This result was not expected;

---

†The experimental data, $\langle\Gamma(z,t)\rangle$, are used to define the Gaussian distribution by the selection of z_c and σ_m which minimizes (least squares) the difference between the experimental data values and the C.D.F. values. The latter is defined as

$$\frac{1}{(2\pi)^{\frac{1}{2}}\sigma_m} \int_{-\infty}^{z} \exp\left[-\frac{1}{2}\left[\frac{\alpha - z_c}{\sigma_m}\right]^2 \right] d\alpha.$$

it is considered to be quite significant. If the large scale, energetic motions in the turbulence field are assumed to be independent of the Reynolds number, then the smaller σ_m values for the Freon 12 experiments suggests that the transport is not solely controlled by the large scale motions. Additional interpretations of this result are made possible by the analytical considerations of Articles 6.2 and 6.3.

The spatial evolution of the mixing region, which is suggested by these results, is presented in Figure 28. It is of interest to note that the boundaries of the ensemble average mixing region are different for the air and Freon 12 experiments and that gross differences are observed for $U_o t/M \gtrsim 50$. It is inferred that subtle differences in the two sets of experiments are probably responsible for the differences in the spatial evolution. It is also inferred, from the relatively self-consistent behavior of σ_m, σ_I and $\sigma_{\Delta z_i}$, that these differences are not significant in the interpretation of the experimental results. The Freon 12 results show a distinct trend, beginning at approximately $\frac{U_o t}{M} = 70\text{-}85$, where the entire mixing field appears to be transported to small z values. Since the extent of the field that is available to be fit by the Gaussian C.D.F. is reduced below a marginal value, the σ_m for $U_o t/M > 110$ are not presented for the Freon 12 carrier gas.

An interesting comparison can be made between the turbulent diffusivity represented by D_τ and the molecular diffusivity D of the carrier gas. Equation (3.2.9b) relates the turbulent diffusivity to the slope of the $z_p^2(t)$ curve. The following results are obtained.

$$D_{\tau(\text{air})} = 14.6 \text{ cm}^2/\text{sec} \quad \text{for } 5 \lesssim U_o t/M \lesssim 20 \qquad (6.1.1a)$$

$$D_{\tau(\text{Freon})} = 12.6 \text{ cm}^2/\text{sec}$$

$$D_{\tau(\text{air and Freon})} = 29.2 \text{ cm}^2/\text{sec} \quad \text{for} \quad 20 \lesssim U_o t/M \lesssim 200 \qquad (6.1.1b)$$

The following ratios are obtained for the turbulent diffusivity to the molecular diffusivity for air in this experiment.

$$\frac{D_\tau}{D(\text{air})} = 73 \quad 5 \lesssim U_o t/M \leq 20 \qquad (6.1.2a)$$

$$\frac{D_\tau}{D(\text{air})} = 146 \quad 20 \lesssim U_o t/M \leq 200 \qquad (6.1.2b)$$

6.2. Measures of the Instantaneous Scans

Figures 30a and 30b, which present the results from the instantaneous scan evaluations for air and Freon respectively, strongly support the "well mixed" condition described by Case 1† of Article 5.4. Specifically, the σ_I values are within 10 percent of the σ_m values at a given $U_o t/M$. The $\sigma_{\Delta z}$ values for air and Freon, which provide a measure of the range covered by the instantaneous centerlines, are substantially smaller than those for σ_I (or σ_m) and they show a much slower growth following their rapidly established "initial" value.

Only the instantaneous scans for $U_o t/M \leq 35$ are considered; the ensemble average results suggest that within this bound, the mixing field is confined within the 74 mm scan length. There is clearly more "scatter" in the air results than in the Freon results. Presumably, this is related to the number of experiments which comprise the ensemble: air: 69, Freon: 100. The Gaussian C.D.F. provides a satisfactory approximation to the $\langle \Gamma(z - z_{ci}) \rangle$ data for both the Freon and the air experiments. This inferrence is based upon the acceptably small values of the standard deviation (S.D.) between the $\langle \Gamma(z - z_{ci}) \rangle$ experimental results and the $\langle \Gamma(z - z_{ci}) \rangle$ values computed from the appropriate C.D.F. (The latter is characterized by the σ_I value described in Article 5.4. and is determined from a least squares fit to the data. Note that the S.D. is based upon the population $[\langle \Gamma(z - z_{ci}) \rangle_{\text{data},k} - \langle \Gamma(z - z_{ci}) \rangle_{\text{Gaus. C.D.F.},k}]$ where k is the index number representing the discrete sample volume. $1 \leq k \leq 205$.

†Case 1: "The instantaneous concentration field is such that an instantaneous scan reveals a well mixed field with transverse dimension and concentration $\Gamma(z,t)$ similar to that of $\langle \Gamma(z,t) \rangle$."

The $\sigma_{\Delta z}$ values for the Freon 12 and air experiments are essentially identical; this comparison is shown on Figure 30b. This is considered to be a most significant result. It was expected, a priori, that the experimental results which were dependent upon the large scale motions would not exhibit a dependence on the Reynolds number. The $\sigma_{\Delta z}$ values are considered to singularly represent the large scale transport of the interfacial region; hence, they are expected to be the same for the Freon 12 and air experiments. The agreement between the two set of experiments is considered to be a confirmation of the experimental technique and the above hypothesis. However, it could (naively) be assumed that σ_m is also singularly dependent upon the large scale motions. This (plausible) assumption is in conflict with the observations for σ_m and, as shown in Figure 30, for σ_I as well. Specifically, $\sigma_I(\text{air}) > \sigma_I(\text{Freon 12})$. Theoretical considerations, which are based upon the Lagrangian dispersion analyses of Appendicies D and E, are presented in Article 6.3. It is shown in that article that a rational explanation of the smaller σ_m values can be formulated. It is presumed that the physical influence of the kinematic viscosity, which was responsible for the relatively lower σ_m values for the Freon 12 experiments, is also responsible for the lower Freon 12 σ_I values. Consequently, a consideration of the σ_I results will be deferred until Article 6.3.

6.3 Inference of the Lagrangian Scales in the Present Experiment

As discussed in Section 3.2., the dispersion parameter z_p is considered to be numerically equal to the σ_m value. For this experiment the contaminant which occupies the lower half of the chamber has a physical "release time" t_r which corresponds to the instant the grid and splitter plate pass the observation plane. The theoretical developments of Appendix D, specifically, the formulation of the dispersion using two separate time scales, can be examined in the context of the σ_m experimental values. The micro and macro time

scales can be estimated by the procedure outlined in Appendix E. These applications of the theoretical results are carried out in this section.

6.3.1. A Priori Estimation of the Lagrangian Microscale

Utilizing Shlien's experimental data and the theoretical development by Hinze [1975], an estimate of the normalized microscale, τ^*, (τ_L/C_1) was obtained in terms of the grid Reynolds number and the parameters in the kinetic energy decay law, see equation (E.7.8). For the present experiment, these parameters have the following numerical values for decaying grid turbulence:

AIR	FREON 12
A = 31	A = 27
U_o = 6.28 m/sec	U_o = 6.28 m/sec
M = 2.54 cm	M = 2.54 cm
$\nu_{air} = 0.15 \times 10^{-4} m^2/sec$	$\nu_{freon} = 0.17\ \nu_{air}$
n = 1.27	n = 1.27

From Equation (E.7.8.) the normalized microscale can be defined as

$$\tau^* = (1 - \frac{n}{2}) \ln \left[1 + \frac{1}{C_L(\frac{3}{2})^{3/4}} \left[\frac{A}{R_m}\right]^{.25\ \dagger}\right] \qquad (6.3.1.)$$

This leads to the following values:

$$\tau^*_{(air)} = .26$$
$$\tau^*_{(Freon)} = .18 \qquad (6.3.2.)$$

The theoretical result for z_p^2, presented in (3.2.22) and plotted in Figure 33, shows that z_p^2 increases for an increasing value of τ^*. Hence, the difference in the predicted τ^* values for air and Freon 12 suggests that the dispersion, using air as a carrier gas, will be greater than that for the Freon 12 carrier gas. The σ_m values of Figure 27 are in

†C_L = .17 obtained from Shlien's [1972] data for dispersion in decaying homogeneous turbulence.

qualitative agreement with this prediction; quantitative considerations are presented below.

For the present experiment, the mixing begins before the turbulence field becomes homogeneous. That is, there is a period, $U_o t/M \lesssim 5$, of inhomogeneity during which significant mean velocity gradients and spatially non-uniform velocity fluctuation intensities exist. Sato and Yamamoto [1974] have quantitatively investigated this period in a wind tunnel investigation of the near field behind a grid. The experimentally observed results of the dispersion were influenced by the inhomogeneous turbulence field for this initial time period and since these physical effects cannot be accounted for by the theoretical considerations of Appendix D, an alternative interpretation of the data is required.

6.3.2. Evaluation of Parameters Which Describe the Turbulent Dispersion

The analytical structure for the dispersion z^{*2} which was developed in Appendix D, and extended in Appendix E, involves the parameters

$$\frac{U_o t_r}{M} \ , \quad \frac{\Delta t_j}{\Delta t_r} \ , \quad \tau^* \ , \quad \Lambda^*$$

In principal, the available experimental data can be interpreted in this theoretical context to infer these parameters. This inferrential process must acknowledge that the analytical structure is quite complex and that the assumptions involved in its construction may invalidate part or all of it. It was found useful to create a set of working drawings. These include: (i) the mean square particle displacement $\frac{1}{2}z_p^2$ as a function of $U_o t/M)^{\dagger}$ data for both air and Freon 12 over the full range of $U_o t/M$ values and (ii) an expanded scale plot of $\frac{1}{2}z_p^2$ for $U_o t/M \lesssim 35$; see Figures 31 and 32. Note that these working plot identify the dispersion as a function of the (normalized) laboratory time. The theoretical curves for

†From subsection 3.2, z_p^2 is identical to σ_m^2 for the assumptions outlined in that subsection.

$\frac{1}{2}z^{*2}(\Delta t/\Delta t_r;\ \tau^*)$ and $\frac{1}{2}z^{*2}(\Delta t/\Delta t_r;\ \Lambda^*)$ were also prepared; see Figures 33 and 34. Note that n = 1.27 for the latter two plots; this value is taken from the study by Comte-Bellot and Corrsin [1966].

A detailed examination of these results reveals that the present analytical formulation is incompatible with the experimental data. Specifically, the experimental results reveal a "plateau" in the z_p^2 distribution ($25 \lesssim U_o t/M \lesssim 40$) and an examination of Figures 33 and 34 show that a similar juncture between the microscale and macroscale dominated distributions is not possible; that is, the present analytical formulation only provides for a juncture of the two linearly increasing z_p^2 distributions. Apparently, a more accurate representation of the Lagrangian correlation function would be required to provide the "plateau" observed in the experimental data (Figures 31 and 32).

6.3.2.1. A Posteriori Evaluation of the Microscale and Δt_r

The experimental data can be used to evaluate the Lagrangian micro and macroscales; the procedure is to find the parameter values which provide optimal agreement between the theoretical and experimental results. This task is made ambiguous by the unknown value of Δt_r to use in the analysis.† Physically, $t_r = 0$; however, the analysis is not valid for small times because of the strong inhomogeneities of the turbulence field. Consequently, a scheme to select self-consistent parameter pairs (τ^*, Δt_r), which also yield z_p^2 values in agreement with the data, was adopted. This scheme is described below.

The $z^{*2}(\Delta t/\Delta t_r)$ theoretical results from the microscale analysis (Figure 33) show that z^{*2} increases linearly for sufficiently large $\Delta t/\Delta t_r$ values. (The curves are necessarily terminated at $\Delta t_L/\Delta t_r$).† Since the experimental results for

†An alternative data processing scheme which would remove this ambiguity is under consideration.

z_p^2 also reveal a region of linear growth (see Figure 31), a scheme which equated the theoretical slope to the processed data slope was adopted.

The experimental data for z_p^2 are made non-dimensional by the specification of an arbitrary Δt_r value (see 3.2.21) and the slope: $0.5d(z^{*2})/d(\Delta t/\Delta t_r)$, is then determined. A unique value of τ^* can then be found which provides the best agreement between the experimentally and theoretically determined slopes. (Note 3.2.22 for $z^*(\Delta t/\Delta t_r; \tau^*, n)$; also note that n is adopted from wind tunnel data for turbulence kinetic energy decay, Comte-Bellot and Corrsin [1966].) This process yields the following results for the $z_p^2)_{air}$ data.

Table II Evaluation of Dispersion Parameters

(U_o/M) (Δt_r):	1.73	2.14	3.47	5.17	7.36	10.8
τ^*:	0.23	0.25	0.3	0.35	0.4	0.5
(U_o/M) (Δt_L):	3.25	4.24	7.91	13.5	22.08	42.55

The Δt_L values of this table are instructive; they provide a means of establishing an upper bound for Δt_r. The experimental data reveal that the plateau begins at approximately $U_o t/M = 20$. Hence $U_o \Delta t_L/M$ must be less than $\simeq 15$ since $U_o t_o/M \simeq 5$. (See Comte-Bellot and Corrsin (1966].) It is apparently not possible to select a lower limit for the possible combination of Δt_r and τ^* values since the z_p^2 data could continue to grow linearly beyond the region which is dominated by the microscale. However, some guidance regarding the minimum value to be expected is gained from the z^{*2} distributions of Figure 32. The value $\tau_L^* = 0.25$ has been adopted as the plausible minimum. Note that the implied juncture region for this τ_L^* value would be quite extensive since the macroscale dominated region is not initiated before $U_o t/M \simeq 30$.

†From the expression: $\Delta t_L/\Delta t_r = \exp[\tau^*/(1-n/2)]$, it is seen that Δt_L represents the maximum possible value of Δt for which the microscale-dominated analysis could be used to describe z^{*2}.

The estimate of $\tau^* = 0.26$ presented in 6.3.1. is, therefore, suspect. It is not clear whether this prediction would be expected to fail because of an improper numerical value for C_L or the inappropriate use of information from Shlien's experiment.† It is pertinent to note that if the τ^* values of (6.3.2.) are accepted as valid, it would be extremely difficult to confirm them with experimental data since the Δt_L values would be quite small.

The present experimental data will be used to reevaluate†† the constant C_L in the expression (6.3.1.) for τ^* as a function of the parameter A and the mesh Reynolds number (R_M). For this, it will be assumed that $\tau^*_{air} = 0.35$ for the air results; note that this value represents the "largest feasible" Δt_r which can be used to fit the slope of the z_p^2 data for $U_o t/M \leq 20$. For $A = 31$, $R_M = 10^4$, and $\tau^* = 0.35$, C_L is evaluated to be 0.2 and (6.3.1) can be rewritten as

$$\tau^* = \left(1 - \frac{n}{2}\right) \ln \left(1 + 6.81 \left(\frac{A}{R_M}\right)^{0.25}\right) \qquad (6.3.3.)$$

This equation can be used to assess the influence of the kinematic viscosity on the observed slope of the z_p^2 distribution between the air and Freon 12 results.

The calculation of $\tau^*_{\text{Freon 12}}$ requires a knowledge of Δt_r. It is reasonable to assume††† that Δt_r is increased by $(U_o t/M = 1)$ to $U_o t_r/M = 6.17$ since t_o (apparent temporal origin of the decaying turbulence) for the larger Reynolds number is known to decrease by approximately this amount; see Wyatt [1955]. The experimentally observed slope of the z_p^2 distribution can

†Molecular diffusion effects from the temperature marker in Shlien's experiment could provide a low estimate of τ^*. This is discussed in Appendix E.3.

††Shlien's data was used in E.7.8. to evaluate C_1; a value of 0.17 was found. The present C_L is approximately 18 precent larger than that inferred from the Shlien data. $C_L (3/2)^{.75}$; its value was determined to be 4.44. The present C_L (= 0.2) differs from C_L found using Shlien's data (i.e., 0.17) by +18 percent.

†††The final result is only slightly affected (5% increase) by this assumption.

be made dimensionless by the procedures noted above; its value is 0.34. This corresponds to a $\tau^*_{\text{Freon 12}}$ value of 0.24. Hence

$$\frac{\tau^*_{\text{Freon 12}}}{\tau^*_{\text{air}}} = \frac{0.24}{0.35} = 0.69$$

The ratio of the τ^* values computed from (6.3.3.) using the air and Freon 12 values is 0.74. The agreement between these two results is interpreted as a strong endorsement for the theoretically inferred effect of the kinematic viscosity on the experimental results.

6.3.2.2. A Posteriori Evaluation of the Macroscale

If it is assumed that the maximum value of Δt_r is reliably inferred by the procedure described in 6.3.2.1 and if it is assumed that Δt_r for the short and long time analyses are the same, then Λ^* may be calculated from the observed slope of the experimental data for large $U_o t/M$ values. These calculations have been executed; it is found that the dimensionless slope (see E.4.2.) is relatively large: i.e., 0.694, and that the corresponding Λ^* is also relatively large. Figure E.3.† provides a numerical value of 3.9 for Λ^*; however, the figure also shows that a slight change in the evaluated slope will create a large change in the inferred Λ^* value. Hence, the indicated Λ^* value is rather uncertain. Figure 34 shows that z^{*2} is not particularly sensitive to the value of Λ^*.

†Figure E.3. is specifically for $\Delta t/\Delta t_r = 3.5$. However, the magnitude of the slope will be only slightly affected by this ratio; see Figure 34.

7. SUMMARY AND CONCLUSIONS

A viable experimental technique to measure the instantaneous concentration (Γ) of a non-diffusive scalar contaminant along a line segment parallel to the principal concentration gradient has been developed. This technique, which is discussed in Section 2, includes the capability to generate small (0.5 μm nominal diameter) marking particles which serve as the non-diffusive contaminant. Theoretical considerations, developed in Section 4, show that the particle's response time (to an impulsively applied motion of the continuum fluid element which serves as the host fluid) is sufficiently small that they follow the continuum motion with satisfactory accuracy, see Figure 17. It is also shown that the particle diffusion caused by the Brownian motion of the host gas, has a negligible influence on the inferred dispersion properties of the turbulence field.

The experimental facility was a closed mixing chamber fitted with a (horizontal) splitter plate to separate the two host gas regions prior to their mixing. A bi-plane, square mesh, round rod grid was used to create the mixing field. Light scattering measurements from small cylindrical volumes ($\ell \simeq 0.36$ mm, $d \simeq 0.1$ mm) were used to sense the presence or absence of the marking contaminant. The concentration at a given location (z) and at a given time from the passage of the grid (t) will be 0 or 1 depending upon the origin of the fluid element in the scattering volume. ($\Gamma = 1$ if the origin was in the lower half-volume.) Ensemble averages of the $\Gamma(z,t)$ data have been constructed ($\langle\Gamma(z,t)\rangle$). The separate assumptions of (i) a constant turbulent diffusivity (D_t) and (ii) a Gaussian distributuion of the particle displacement lead to the same analytical result that $\langle\Gamma(z,t)\rangle$ is a Gaussian Cumulative Distribution Function (C.D.F.). The experimental data were fit with such a C.D.F. and the standard deviation of the fit was evaluated.

Conclusion: The Gaussian C.D.F. provides a satisfactory description of the experimentally determined $\langle\Gamma(z,t)\rangle$. The standard deviation of this

distribution (σ_m) provides an appropriate width measure of the ensemble averaged mixed region.

The experimentally determined σ_m and the above noted analytical considerations allow D_t to be evaluated.

Conclusion: The ratio of D_t to the host gas molecular diffusivity is, for air as the host gas,

$D_t/D = 73 \qquad 5 \lesssim U_o t/M \lesssim 20$

$D_t/D = 146 \qquad 20 \lesssim U_o t/M \lesssim 200$

The dispersive property of the decaying turbulence field is represented by the mean square particle displacement z_p^2; see (3.2.8.). [$z_p^2(t)$ is shown to be equal to σ_m^2 (t) for the assumed Gaussian C.D.F. of the particle displacements]. An extensive theoretical development for the relationship of z_p^2 to the Lagrangian micro and macroscales which are used to characterize the Lagrangian auto correlation function, R_L, has been carried out in Appendix D. This analysis has been used to reevaluate the experimental results of Shlien [1972], see Appendix E. The present theoretical work utilizes the concept of a stationary $R_L(\tau)$, Batchelor and Townsend [1956], where τ is a stretched time coordinate ($\tau = C \ln[(t - t_o)/(t_r - t_o)]$); this feature is in common with prior analyses. The present theoretical structure is distinct in its use of separate micro and macro scales for the Lagrangian correlation function and for its relatively direct procedure to relate the experimental and theoretical results. Specific conclusions based upon the comparison of the theoretical and experimental results follow.

Conclusion: The experimental data of Shlien [1972] are well fit by the present analytical formulation. The Lagrangian, normalized microscale τ^* was determined from the z_p^2 data for small values of $\Delta t/\Delta t_r$; its numerical value is 0.185. The Lagrangian normalized macro scale was determined from the z_p^2 data for large $\Delta t/\Delta t_r$ values; its numerical value is 0.213.

Precise Δt_r values (42 and 98) are known for the Shlien data since the thermal marker was introduced with a heated wire; a precise value of Δt_r cannot be established for the present experiment since the mixing begins in the inhomogeneous region immediately following the passage of the grid. However, for the present study, the τ^* and Δt_r evaluations may be jointly determined by forcing agreement between the experimental and theoretical slopes of the z_p^2 vs $\Delta t/\Delta t_r$ curves. This procedure results in a range of τ^* and Δt_r values; this range can be limited by the following observation. z_p^2 (t) initially grows in apparent agreement with the theoretical description provided by the microscale dominated region of the $R_L(\tau)$ distribution, it passes through a "plateau" region where its growth is relatively slow, and it continues its growth in apparent agreement with the macroscale dominated region of the R_L (τ) distribution. (Both the air and Freon 12 host gases exhibited this behavior.) The initiation of the plateau allows a maximum τ^* to be defined.

Conclusion: The maximum value of $\tau^*)_{air}$ is 0.35 and the corresponding $U_o \Delta t_r/M$ value is 5.17, see section 6.3.2.1.

Conclusion: The macroscale, Λ^*, calculated from the comparison of the data to the long time theoretical result, is 1.9, from Section 6.3.2.7. This value is recognized to be quite uncertain because the calculation procedure shows that Λ^* is quite sensitive to small changes in the Δt_r inferred from the macroscale evaluation. The "maximum value" of Δt_r was used to determine Λ^*.

The Reynolds number dependence of the σ_m and z_p^2 results was not expected; it was expected (á priori) that these measures of the dispersion field would solely reflect the large scale motions and that the scale of these motions would be fixed by the grid mesh size, M. However, the theoretical considerations of the disperion analysis provide a rational explanation for the experimental observations. Specifically, it is shown that τ^* may

be expected to decrease as the Reynolds number is increased since the constant C, in the $\tau = C \ln (\Delta t/\Delta t_r)$ transformation, is Reynolds number dependent. Hence the 6 fold change in ν between Freon 12 and air can be expected to change z_p^2, the mean square particle displacement.

Conclusion: Using the air results for the maximum τ^* and the theoretical structure of Appendix D, the smaller dispersion for the Freon 12 shown in Figure 31, is made rational both qualitatively and quantitatively from Equations (6.3.1.) and (6.3.3.) as

$$\left(\frac{\tau^* \text{ Freon 12}}{\tau^* \text{Air}}\right)_{\text{experimental}} = 0.69, \quad \left(\frac{\tau^* \text{ Freon 12}}{\tau^* \text{ Air}}\right)_{\text{theoretical}} = 0.74$$

The availability of "instantaneous" scans for $\Gamma(z,t)$ allows additional measures of the mixing field to be evaluated as discussed in Section 5.4. Statistical measures of the instantaneous scans are examined to determine if the ensemble average mixing results can be traced to (1) a well mixed region for each realization which has the same nominal width as the ensemble average field or (2) a relatively narrow mixed region which is convected by the large scale motions to yield the observed width of the ensemble average field. The instantaneous scans were shifted (Δz) to align their instantaneous centers. The width $\sigma_{\Delta z}$ reflects the magnitude of these shifts; σ_I reflects a measure of the Gaussian C.D.F. which was fitted to the shifted and ensemble averaged concentration distributions.

Conclusions: The approximate equality of σ_I and σ_m ($\sigma_I \gtrsim .8\sigma_m$) and the small values of $\sigma_{\Delta z}$ ($\sigma_{\Delta z} \lesssim .5\sigma_m$) imply that the observed mixing is strongly influenced by the relatively small motions of the turbulence field, see Figure 30.

Conclusions: The essential equivalence of the $\sigma_{\Delta z}$ values for the Freon 12 and air host gases implies that $\sigma_{\Delta z}$ is both a measure of the large scale motions and that these large scale motions are insensitive to the Reynolds number.

REFERENCES

1. Abernathy, F. H. and Kronauer, R. E., "The formation of vortex streets," Jour. Fluid Mech., v. 13, no. 1, (1962).

2. Batchelor, G. K., Howells, I. D. and Townsend, A. A., "Small scale variations of convected quantities like temperature in turbulent fluid," Jour. Fluid Mech., v. 5, p. 134, (1959).

3. Batchelor, G. K. and Townsend, A. A., "Turbulent Diffusion," Surveys in Mechanics, Ed. by G. K. Batchelor and R.M. Daires Cambridge Univ. Press, New York, (1956).

4. Becker, H. A., "Mixing, concentration fluctuations and marker nephelometry", Studies in Convection, v. III, ed., B. Launder, p. 45-139 (1977).

5. Bendat, J. S., Piersol, A. G., Random Data: Analysis and Measurement Procedures, Wiley Interscience (1971).

6. Bradshaw, P. "Interacting Shear Layers in Turbo Machines and Diffusers", Turbulence in Internal Flows, Ed. SNB Murthy, Hemisphere Publishing Corp., Washington (1977).

7. Brodkey, R. S., "Mixing in turbulent fields", Turbulence in Mixing Operations, Academic Press Inc., New York, p. 48-119 (1975).

8. Chao, B. T., "Oesterreichischer", Ingenieur-Archiv., v. 18, p. 7 (1964).

9. Comte-Bellot, G. and Corrsin, S. "The use of a contraction to improve the isotropy of grid generated turbulence", J. Fluid Mech., v. 25, p. 657-682 (1966).

10. Comte-Bellot, G and Corrsin, S., "Simple Eulerian time correlations of full and narrow band velocity signals in grid generated isotropic turbulence," Jour. Fluid Mech. Vol. 48, p. 278 (1971).

11. Cooper, G. R., McGillem, C. D., "Methods of signal and systems analysis", Holt, Rinehart and Winston, Inc. (1967).

12. Corrsin, S. and Lumley, J., "On the equation of motion for a particle in a turbulent fluid", App. Sci. Res., v. A 6, p. 114 (1956).

13. Corsin, S., Limitations of Gradient Transport Models in Random Walks and in Turbulence Advances in Geophysics, v. 18A, Academic Press, N.Y. (1974).

14. Corrsin, S., "Some current problems in turbulent shear flows", Naval Hydronamics Publication 515 (1957).

15. Chevray, R,. "Total dispersion of a scalar quantity in turbulent flow", Private communication of a manuscript (1977).

PRECEDING PAGE BLANK

16. Dubes, R. C., The Theory of Applied Probability PRENTICE-HALL, Inc., Englewood Cliffs, N.J. (1968).

17. Falco, R., "Measurement of intensity and correlation from the initial to final period of decaying grid generated turbulence," Ph.D. dissertation, Dept. of Aero and Mech. Sciences, Princeton Univ.

18. Foss, J. F., Shlien, D. J. and Corrsin, S., "Study of a thermal interface in isotropic turbulence," Bulletin of the American Physical Soc., sec. 11, v. 7, no. 11, p. 1089 (1972).

19. Friehe, C. A. and Schwarz, "Grid generated turbulence in dilute polymer solution," Jour. Fluid Mech., v. 44, p. 173-193 (1970.

20. Gibson, C. H. and Schwarz, W. H., "Universal equilibrium spectra of turbulent velocity and scalar fields," Jour. Fluid Mech., v. 16, p. 365, (1963).

21. Grant, H. L. and Nisbet, I.C.T., Jour. Fluid Mech., v. 2, p. 263 (1957).

22. Hinze, J. O., Turbulence, McGraw Hill Book Co., New York (1975).

23. Hirschfelder, J. O., Curtiss, C. F. and Bird, R. B., Molecular Theory of Gases and Liquids, John Wiley and Sons, New York (1954).

24. Hirschkron, R., and Echrich, F. F., "Entrained particles trajectories in swirling flow," ASME Paper 64-WA/FE-30, (1964).

25. Johnson, D. A., "An investigation of the turbulent mixing between two parallel gas streams of different composition and density with a laser doppler velocimeter," Univ. of Missouri, Columbia, Ph.D. dissertation, Mechanical Engineering Dept. (1971).

26. Khosla, P. K. and Lederman, S., "Motion of spherical particle in turbulent flow," Pibal Report No. 73-22, Polytech. Inst. of New York (1973).

27. Libby, P. A., "Diffusion of heat downstream of a turbulence grid," Acta Astronautica, v. 2, p. 867-878 (1975).

28. Monin, A. S. and Yaglom, A. M., Statistical Fluid Mechanics, V. 1, English translation by J. L. Lumley, M.I.T. Press (1971).

29. Nye, J. O. and Brodkey, R. S., "The scalar spectrum in the viscous-convective subrange," Jour. Fluid Mech., v. 29, p. 151-163 (1967).

30. Ozisik, M. N., Boundary Value Problems of Heat Conduction, International Textbook Co. (1968).

31. Potter, M. C. and Foss, J. F., Fluid Mechanics, The Ronald Press Co. (1975).

32. Rayleigh, Lord, "On the instability of cylindrical fluid surfaces," Phil., May 5, XXXIV. 177 (1892).

33. Roshko, A., "On the development of turbulent wakes from vortex streets," NACA Rep. 1191 (1954).

34. Saffman, P. G., "Some aspects of the effects of the molecular diffusivity in turbulent diffusion," The Mechanics of Turbulence, Gordon and Breach, New York (1964).

35. Saffman, P. G., "On the stability of laminar flow of a dusty gas," Jour. Fluid Mech., v. 13, p. 120-128 (1961).

36. Sato, Y. and Yamamato, K., "Local structure of isotropic turbulence," Bulletin, Yokohama Nat. Univ., v. 23 (1974).

37. Schlichting, H., Boundary Layer Theory, translation by J. Kestin, McGraw Hill Book Co., New York 6th ed. (1968).

38. Shlien, D. J., "Dispersion measurements of a fluid sheet in two turbulent flows," Ph.D. dissertation, Mech. Dept., Johns Hopkins Univ. (1972).

39. Shlien, D. J. and Corrsin, S., "A measurement of lagrangian velocity auto correlation in approximately isotropic turbulence," Jour. Fluid Mech., v. 62, p. 255-271 (1974).

40. Soo, S. L., Fluid Dynamics of Multiphase Systems, Blaisdell Publication Co., Massachusetts (1967).

41. Taylor, G. I., "Diffusion by continuous movements," Proc. London Math. Soc., ser. A, v. 20, p. 196-212 (1922).

42. Taylor, G. I., "Statistical theory of turbulence IV-diffusion in a turbulent air stream," Proc. Royal Soc., ser. A, vol. 151, no. 873, London, p. 465-478 (1935).

43. Tchen, C. M., "Mean value and correlation problems connected with the motion of small particles suspended in a turbulent fluid," Dissertation publ. 51 of Lab for Aero- and Hydrodynamics, Tech. Univ. of Delft (1947).

44. Townsend, A. A., "The diffusion of heat spots in isotropic turbulence," Proc. Royal Soc., vol. A209, no. 1098, p. 418-430 (1954).

45. Townsend, A. A., "The diffusion behind a line source in homogeneous turbulence," Proc. Royal Soc., v. A224, no. 1159, p. 487-512 (1956).

46. Uberoi, M. S. and Corrsin, S., "Diffusion of heat from a line source in isotropic turbulence," NACA Report 1142 (1953).

47. Uzkan and Reynolds, "A shear-free turbulent boundary layer," J. Fluid Mech. v. 28, pt. 4, p. 803-821 (1967).

48. Yeh, T. T. and Van Atta, C. W., "Spectral transfer of scalar and velocity fields in heated grid turbulence," J. Fluid Mech., v. 58, no. 2 p. 233-261 (1973).

49. Wyatt, L. A., "Energy and spectra in decaying homogeneous turbulence," Ph.D. thesis, Univ. of Mass. (1955).

Table 1 Slit and Scattering Volume Dimensions from Selected Locations

Fraction of Slit length, measured from r_o	Slit Width w				Slit Height: ℓ				Scattering Volume Height: ℓ/M			
	Slit No: 1	2	3	4	1	2	3	4	1	2	3	4
1/16	0.26	0.23	0.27	0.24	0.36	0.32	0.37	0.33	0.26	0.23	0.27	0.24
3/16	0.20	0.20	0.30	0.27	0.26	0.26	0.38	0.34	0.19	0.19	0.28	0.25
5/16	0.27	0.20	0.26	0.25	0.33	0.24	0.32	0.30	0.24	0.17	0.23	0.22
7/16	0.26	0.17	0.36	0.22	0.31	0.20	0.43	0.26	0.22	0.15	0.31	0.19
9/16	0.25	0.17	0.33	0.24	0.29	0.20	0.38	0.27	0.21	0.14	0.27	0.20
11/16	0.26	0.14	0.38	0.19	0.29	0.16	0.43	0.21	0.21	0.12	0.31	0.15
13/16	0.22	0.14	0.27	0.20	0.24	0.15	0.3	0.21	0.17	0.11	0.22	0.15
15/16	0.21	0.15	0.27	0.17	0.23	0.17	0.29	0.18	0.16	0.12	0.21	0.13

Notes: Slit geometry: $r = r_o + c_s$; $r_o = 6.99$ cm, $c_s = 7.14$ cm/radian

$\Psi = \tan^{-1} c_s/r$: angle of intersection between slit and vertical laser beam

$\ell = w/\cos\Psi$: vertical dimension of slit

ℓ/M = vertical dimension of scattering volume, M = magnification = 1.38

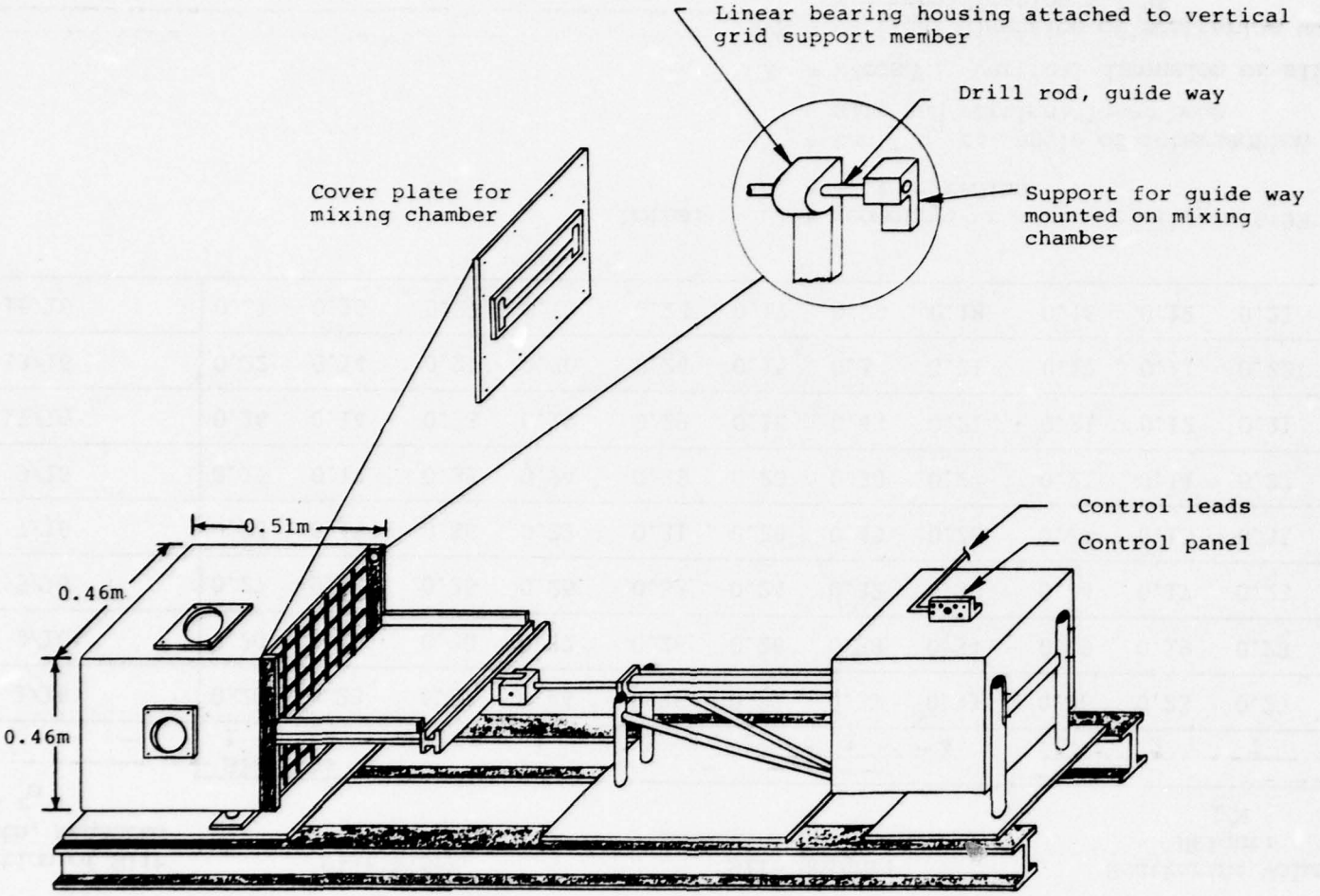

Figure 1. Schematic Representation of the Mixing Chamber
Note: Biplane, square mesh grid is attached to the splitter plate.

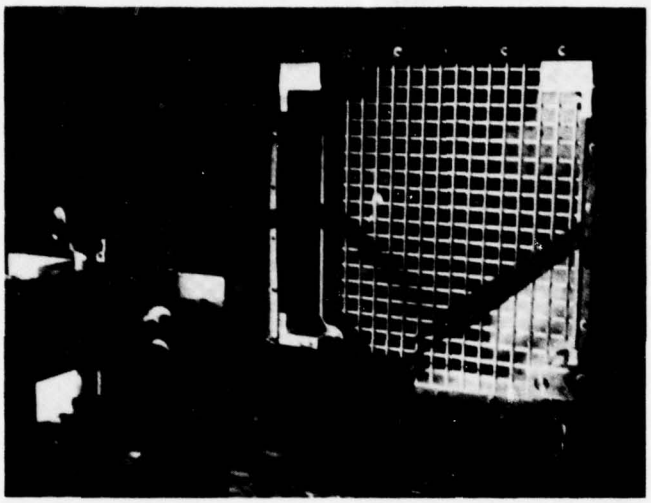

Figure 2. Detail of Turbulence Generating Grid

Note: Front wall and splitter plate have been removed for this photograph

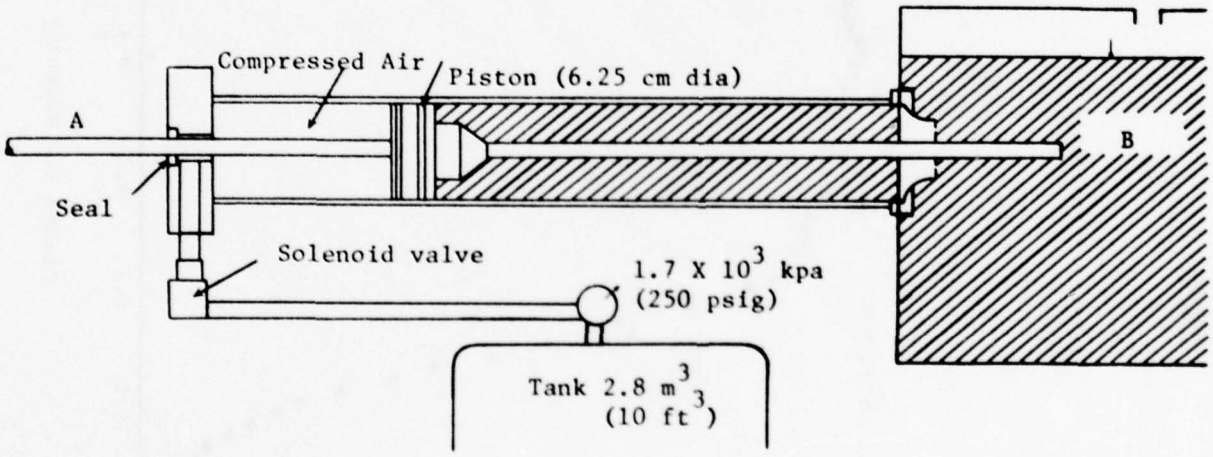

Figure 3. Schematic Representation of the Acceleration/Deceleration System

Notes: A shaft connects to the grid-plate unit
B hydraulic oil

The steady state motion of the piston represents balance between the driving effects of the compressed air and the resisting effects of the high pressure hydraulic oil. The deceleration of the piston is caused by the pressure increase in the hydraulic oil as the conical plug (a) seats into the tapered nozzle (b); see Appendix B.

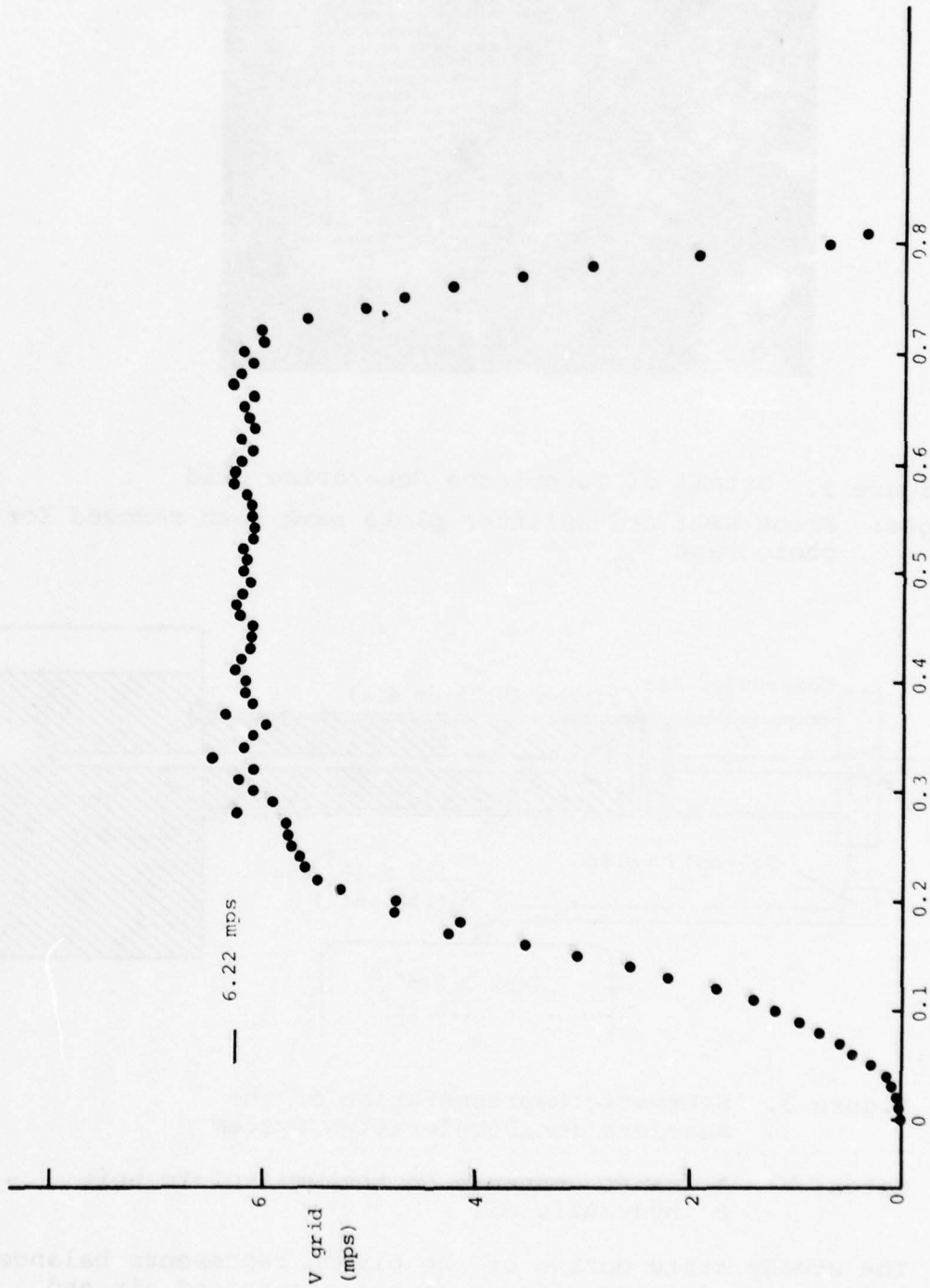

Figure 4. Velocity of Grid as a Function of Time.

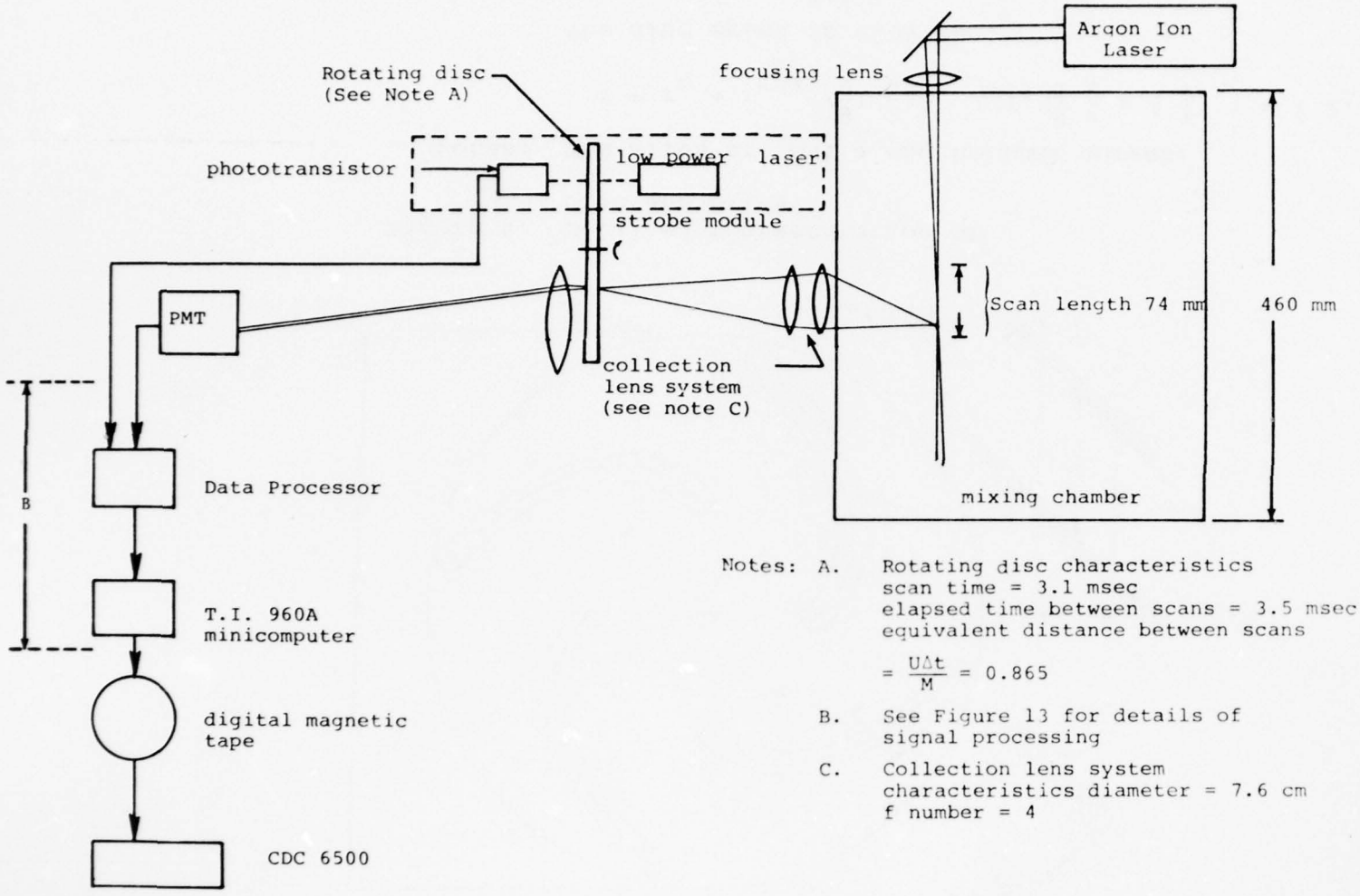

Notes: A. Rotating disc characteristics
scan time = 3.1 msec
elapsed time between scans = 3.5 msec
equivalent distance between scans

$$= \frac{U\Delta t}{M} = 0.865$$

B. See Figure 13 for details of signal processing

C. Collection lens system characteristics diameter = 7.6 cm
f number = 4

Figure 5. Schematic Representation of the Optical and Data Acquisition Systems

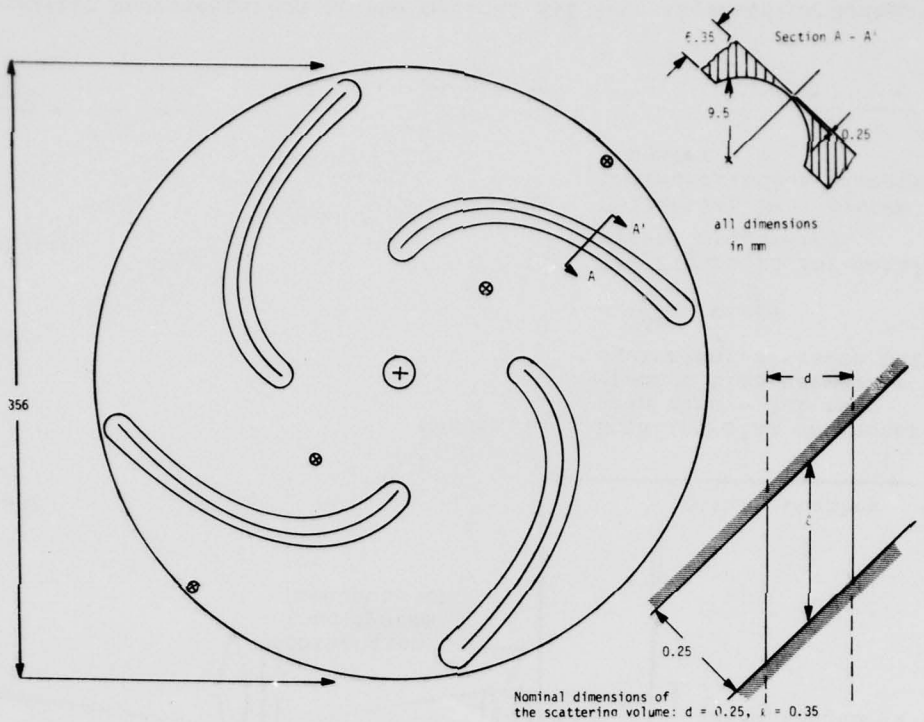

Figure 6. Detailed Representation of Disc and Slits

Notes: The slits are cut along helical curves:

$$r = r_o + r_{max} \left(\frac{9}{8}\right)\left(\frac{2}{\pi}\right)\theta_i \quad \theta \leq \theta_i \leq \frac{8}{9}\frac{\pi}{2} + j\frac{\pi}{2},\ j = 1,2,3$$

The disc speed is 4300 rpm,

$r_{max} - r_o = 100$ mm.

Figure 7. Representative cross-section of light transmission slit in the rotating disc.

Note: Magnification of photograph ≈ 125

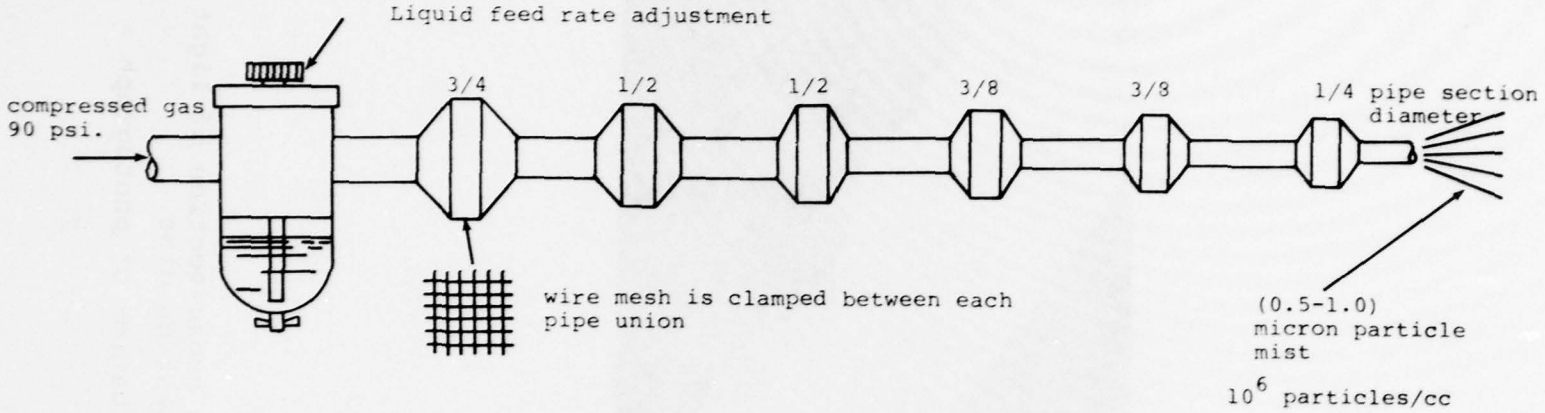

Figure 8. Particle generator suitable for use with air.

Notes: plain double crimped weaved brass wire cloth 100x100/inch mesh
compressed flat under 25 ton load
wire diam. = 4.5 mil expanded to 5.5 mil
width opening = 5.5 mil compacted to 4.5 mil

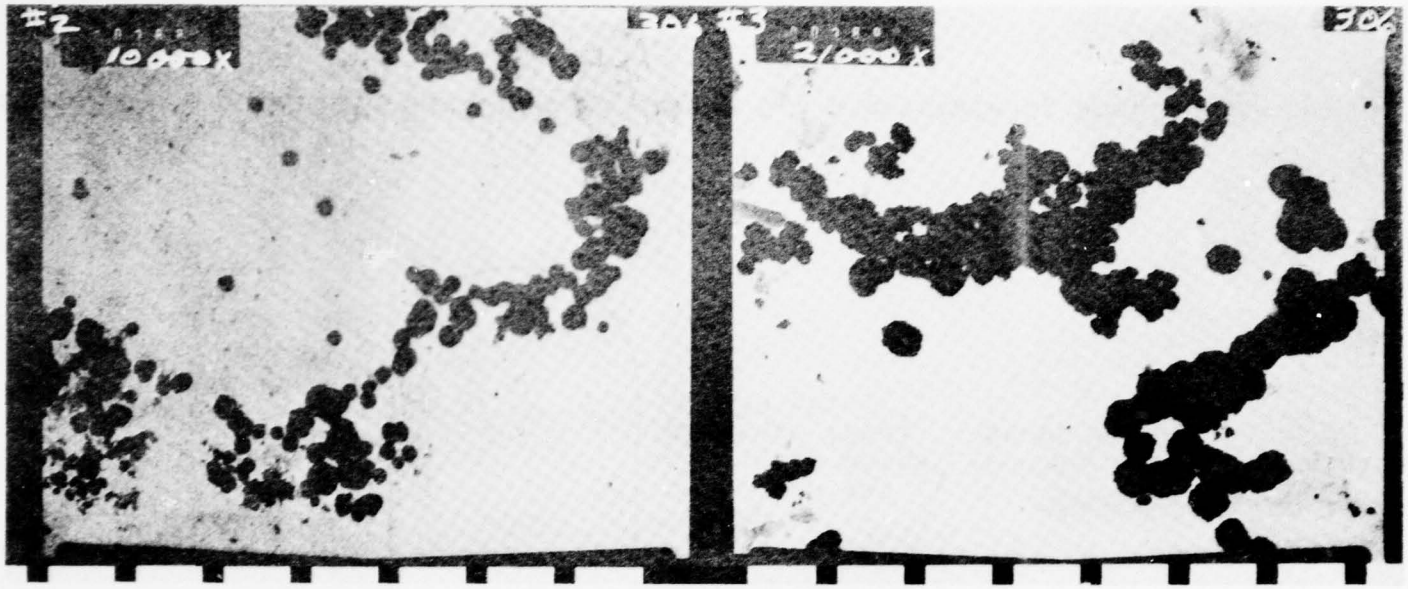

Figure 9. Electron Microscope Photograph of Soy Bean Oil Droplets.

Note: Amplification Factor in Upper Left Corner.

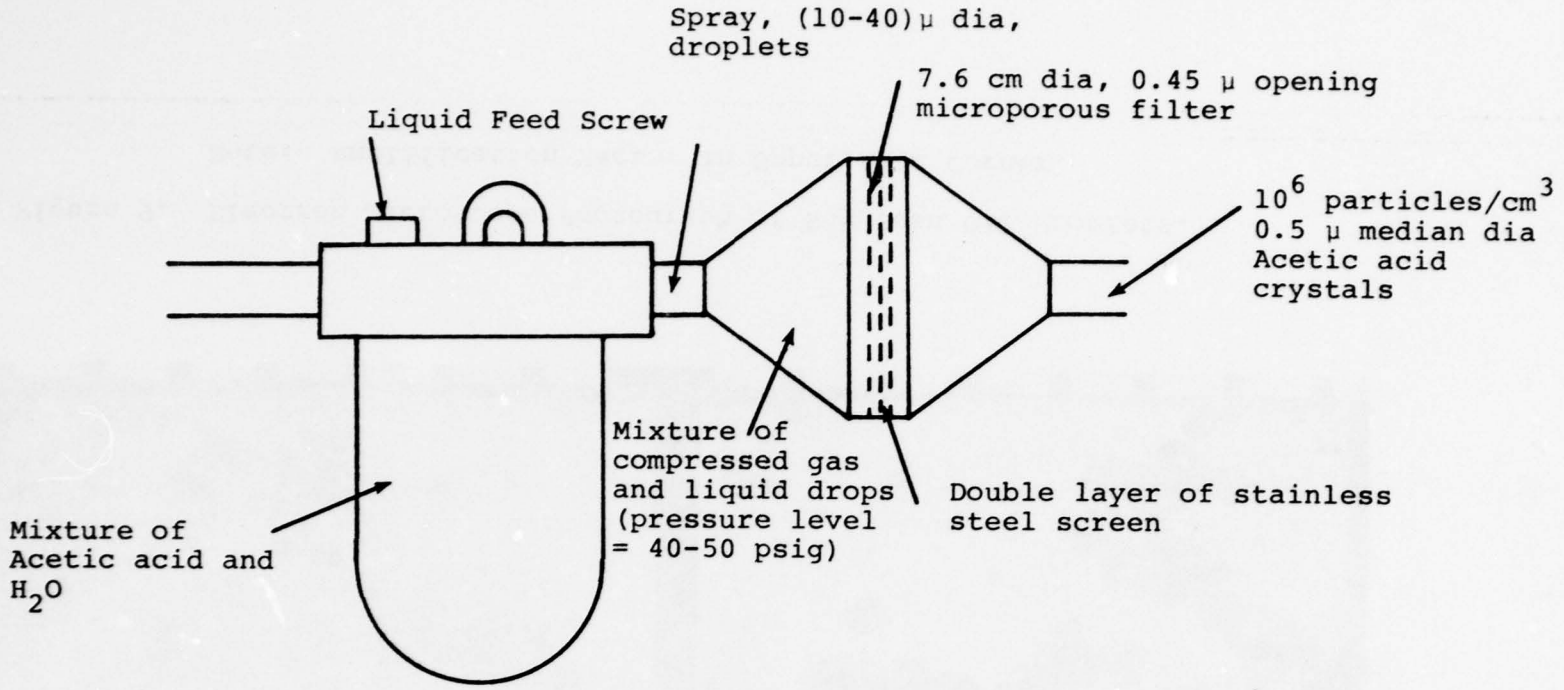

Figure 10. Particle Generator to create 0.5 μ crystals of Acetic Acid

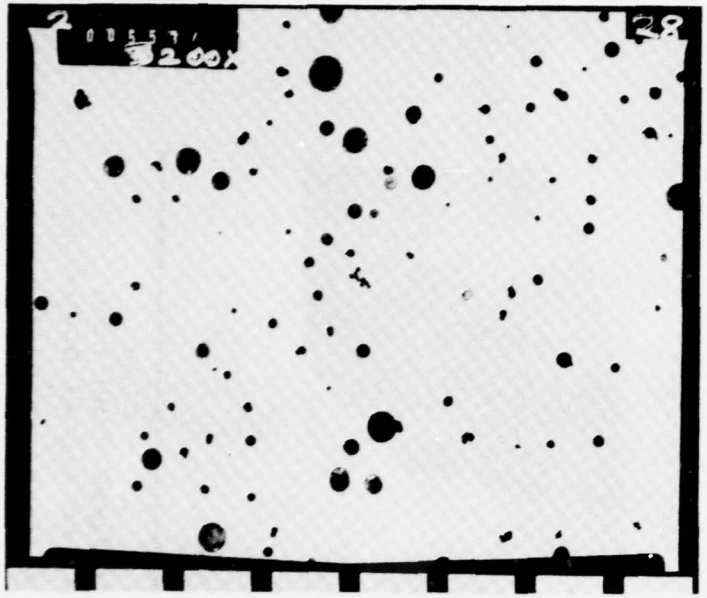

a. Particles

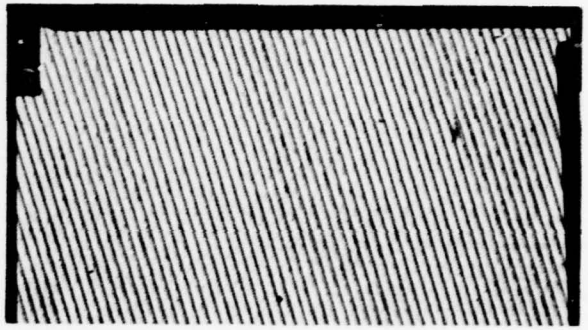

b. Reference length: 0.5 μm/Division

Figure 11. Electron Microscope Photograph of Acetic Acid Particles

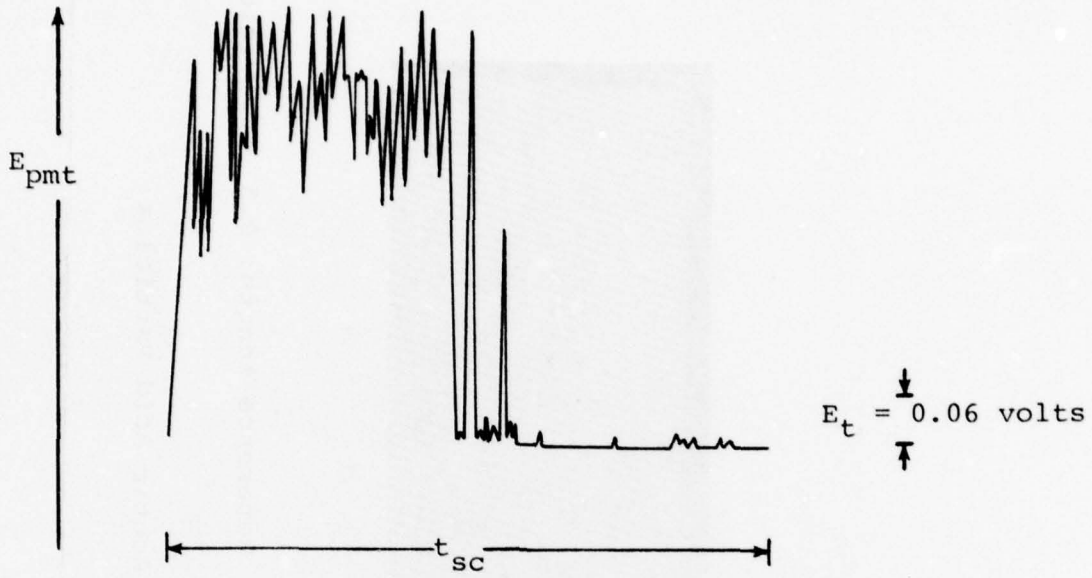

a. Instantaneous Scan
Note: E_t = threshold voltage level for the comparator circuit, see Figure 13.

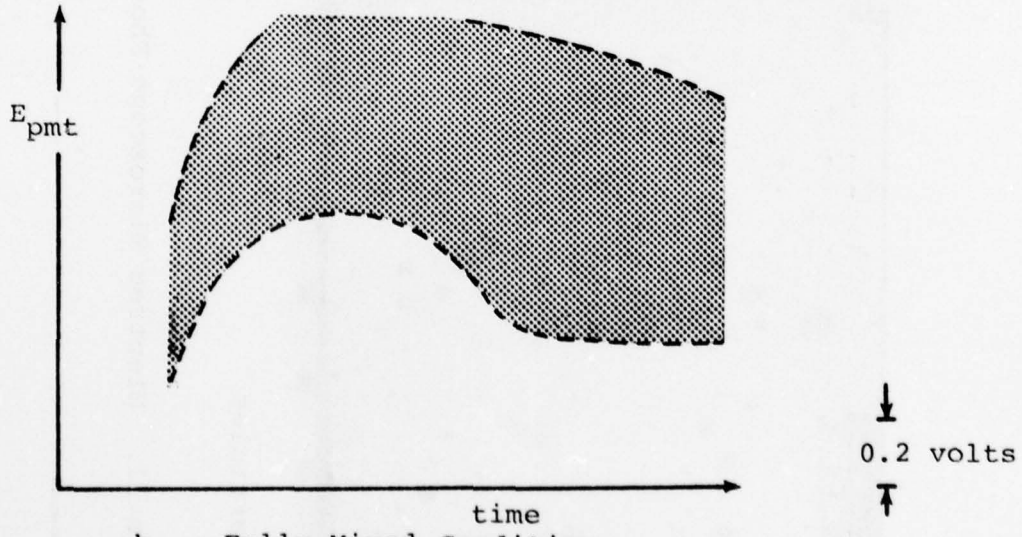

b. Fully Mixed Condition
Note: No signal dropouts

Figure 12. Ink Tracings of Oscilloscope Photographs Showing:
a.) An instantaneous scan of the photomultiplier tube voltage (E_{pmt}) for the second scan following the passage of the grid
b.) A 3-second time exposure of the scope traces for the fully mixed condition of large time

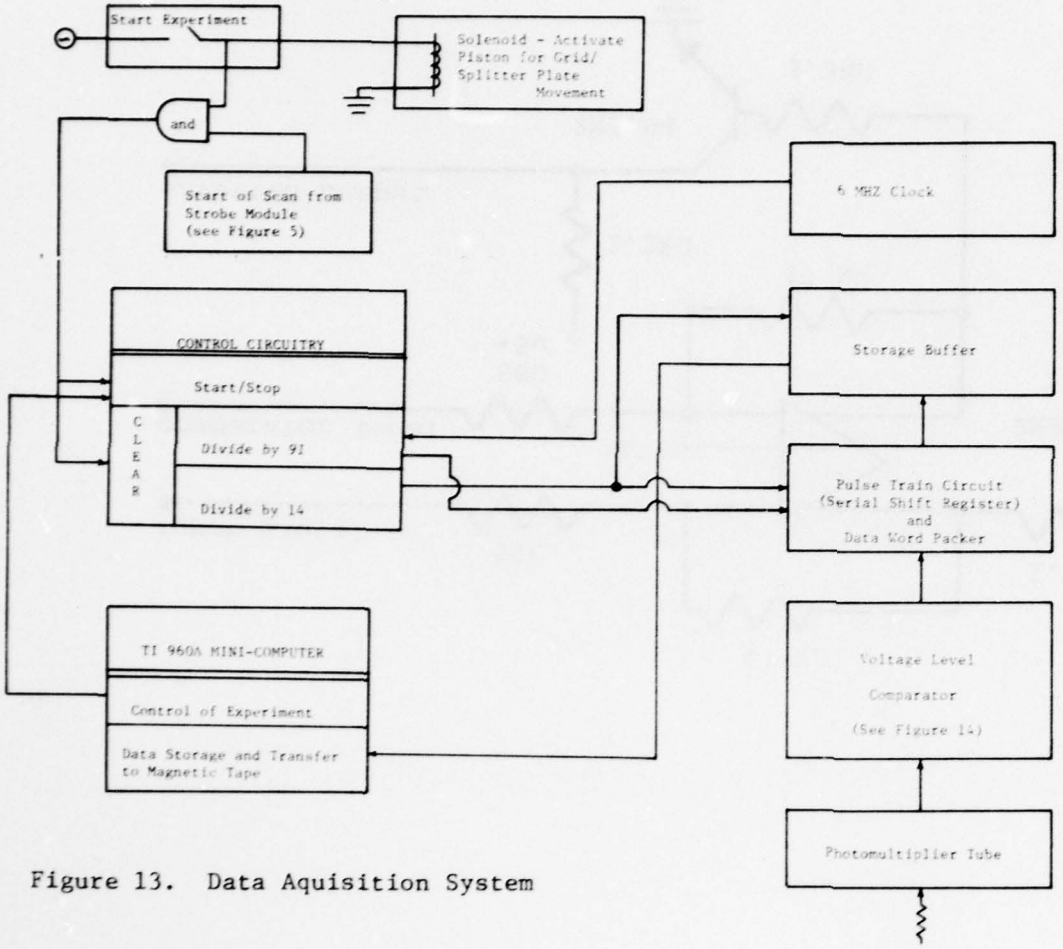

Figure 13. Data Aquisition System

Notes: 1) Voltage Level Comparator - creates pulse train of 0, 1 from the p.m.t. signal. Signal noise level ~0.01 volts, E_t (comparator threshold level) set at ~0.06 volts, and typical signal levels are 0.2-0.3 volts. (Signal/noise ratio = 20, signal threshold ratio ~3)

2) Pulse Train Circuit - comparator level is examined for 5μ sec at 15.2μ sec intervals. This yields 205 points in a 3.11m sec scan.

3) The data samples are drawn from 0.36mm segments along the incident laser beam. The 0, 1 bits represent (respectively) the absence or presence of gas B in the instantaneously defined scattering volume.

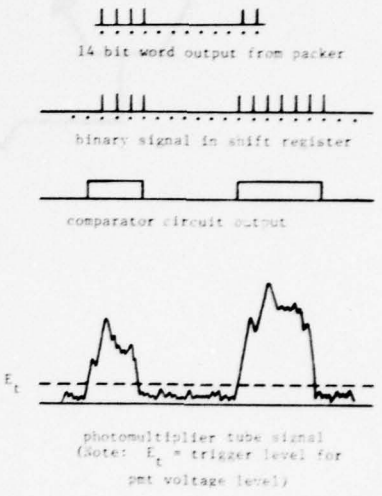

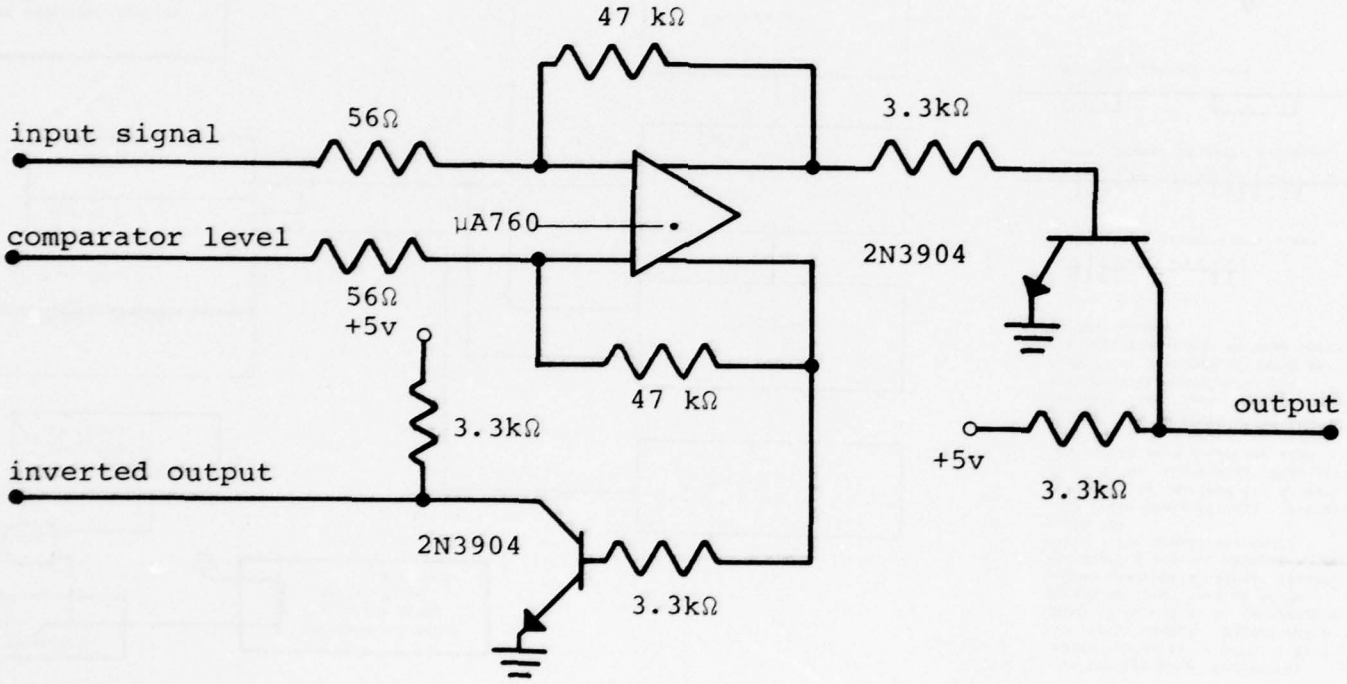

Figure 14. Circuit Diagram for the Comparator Circuit

Figure 15. Representation of the non-diffusive mixing field
Note: Gas A = Air, Gas B = Air
Note: $ - presence of gas B in the scattering volume; 100 of the 205, data points are shown. Nominally every other data point in a scan is shown: (1,2,3...100) Correspond to 2,4,6,...200)
For the graph horizontal locations: 1 is the z value: +37.1 mm.
100 is the z value: -35.5 mm
For the graph vertical locations: 1 → 120 are the scan numbers; each scan is executed in 3.11 msec and the scans are repeated every 3.5 msec.

U_o (3.5 msec) = 0.865 M.

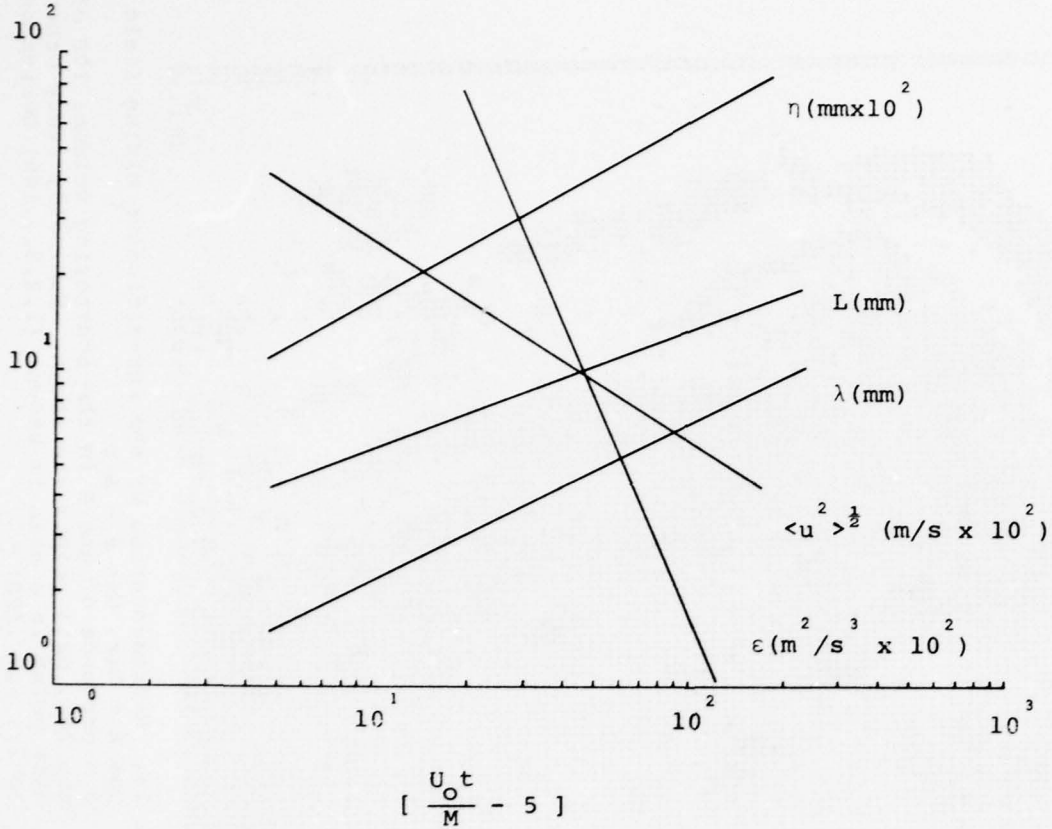

Figure 16. Representative length and velocity scales for homogeneous turbulence calculated from the $\tilde{u}^2$ data of Wyatt [1955].

Notes: R_n - 10^4, m - 2.54 cm, U_o = 6.25 m/s
biplanar round rod grid, 0.34 solidity ratio

$\langle u^2 \rangle$ measured data used with isotropic relations to compute other values shown.

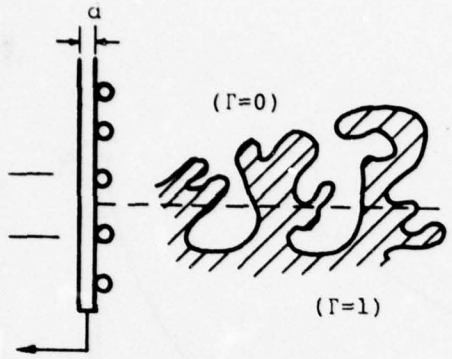

U_o = velocity of grid

a.) Schematic representation of mixing

t_o apparent temporal origin of turbulence

$$\frac{\tilde{w}^2}{U_o^2} = \frac{1}{A}\left[\frac{U_o t}{M} - \frac{U_o t_o}{M}\right]^{-n}$$

t_r apparent time at which contaminant is released

$\Delta t_r = t_r - t_o$, $\Delta t = t - t_o$

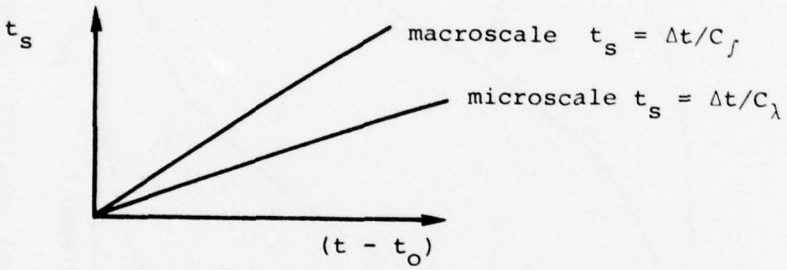

b.) Schematic representation of Lagrangian time scales development

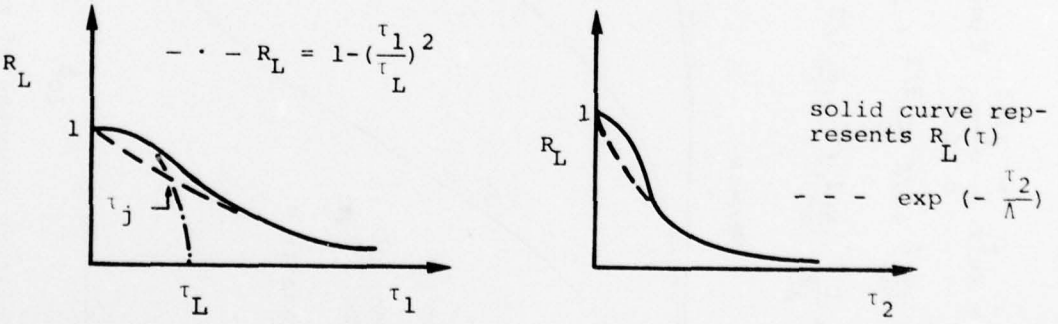

c. Definition sketches for τ (microscale), τ_j (juncture point) and Λ (macroscale) for the Lagrangian auto correlation function which is assumed to be stationary in the stretched τ coordinates

Notes: $$R(t\ \delta t) = \frac{\langle u(t)\ u(t+\Delta t)\rangle}{\tilde{u}(t)\ \tilde{u}(t+\Delta t)} = R_L(\tau)$$

$$\tau = \int_{\Delta t_r}^{\Delta t} \frac{dt}{t_s}\ ;\quad \tau_1 = C_\lambda \ln\frac{\Delta t}{\Delta t_r},\quad \tau_2 = C_f \ln\frac{\Delta t}{\Delta t_r},\quad \tau_j \text{ is defined by:}$$

$$1-\left(\frac{\tau_j}{\tau_L}\right)^2 = \exp\left[\frac{-\tau_j}{(C_\lambda/C_f)\Lambda}\right]$$

Figure 16b. Schematic representation of the quantities used in the Lagrangian dispersion analysis.

$$\langle \hat{up}^2 \rangle = \langle u^2 \rangle \int_0^\infty \frac{\Omega^{(1)}}{\Omega^{(2)}} \, F(\omega) \, d\omega$$

$$\Omega^{(1)} = \left(\frac{\omega}{\alpha}\right)^2 + \sqrt{6}\left(\frac{\omega}{\alpha}\right)^{3/2} + 3\left(\frac{\omega}{\alpha}\right) + \sqrt{6}\left(\frac{\omega}{\alpha}\right)^{1/2} + 1$$

$$\Omega^{(2)} = \frac{1}{\beta^2}\left(\frac{\omega}{\alpha}\right)^2 + \frac{\sqrt{6}}{\beta}\left(\frac{\omega}{\alpha}\right)^{3/2} + 3\left(\frac{\omega}{\alpha}\right) + \sqrt{6}\left(\frac{\omega}{\alpha}\right)^{1/2} + 1$$

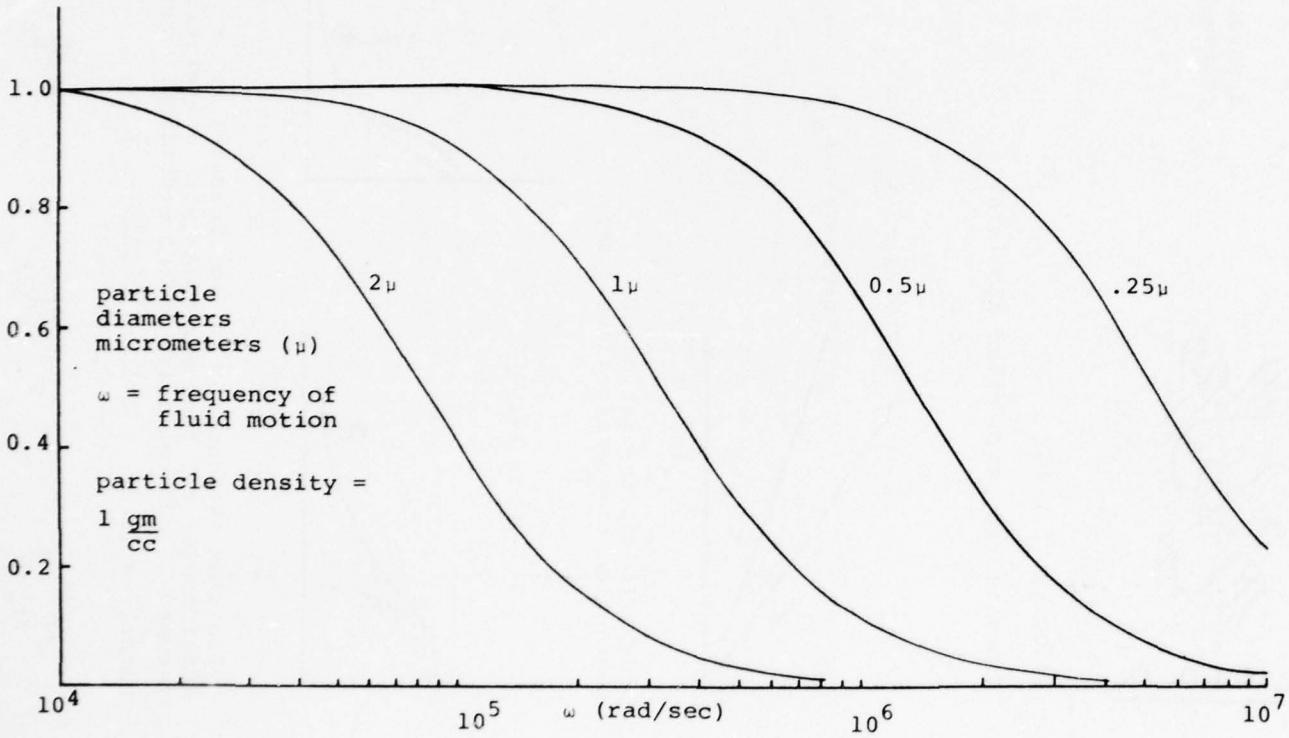

Figure 17. Amplitude response of spherical particles to an oscillatory air flow from equation 4.1.7.

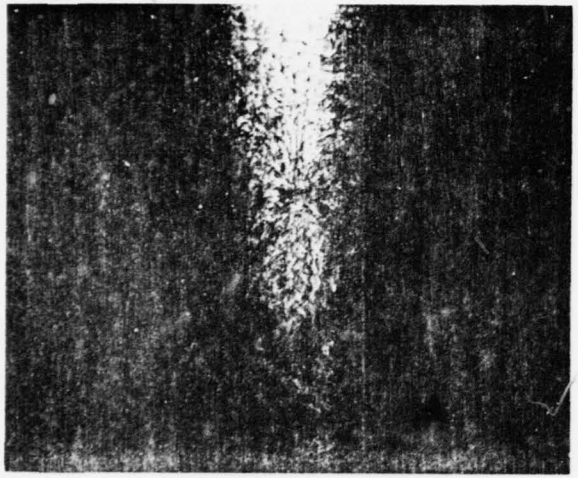

(i)

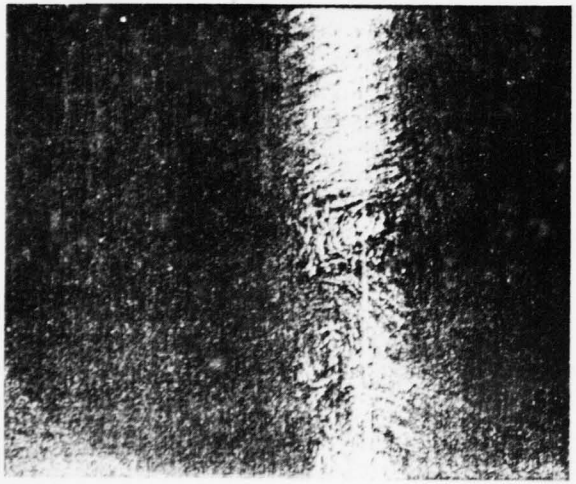

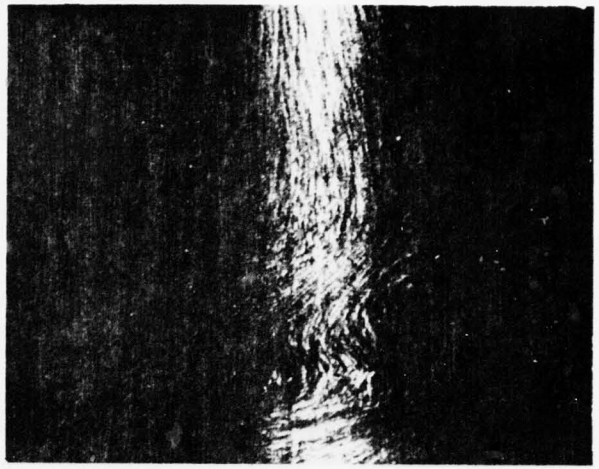

(iii)

0.25 M

Figure 18. Close-up of the initial mixing process to show the periodic structures developed from the instability of the vortex sheet. Elapsed times from the passage of the grid are

i) 0.02 sec
ii) 0.04 sec
iii) 0.06 sec

Note: The divider plate is at the bottom of the photograph.

AD-A060 463 PURDUE UNIV LAFAYETTE IND PROJECT SQUID HEADQUARTERS F/G 20/4
AN EXPERIMENTAL STUDY OF THE TRANSPORT OF A NON-DIFFUSIVE SCALA--ETC(U)
AUG 78 K C CORNELIUS, J F FOSS N00014-75-C-1143
UNCLASSIFIED SQUID-MSU-1-PU NL

2 OF 2
AD
A060 463

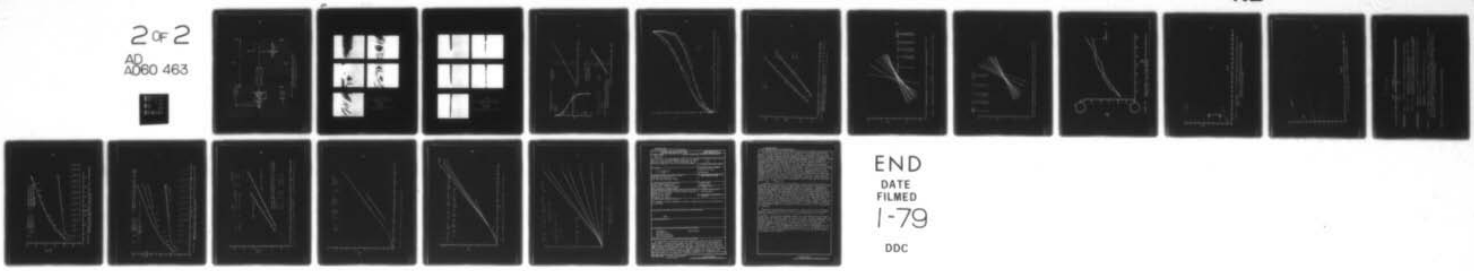

END
DATE
FILMED
1-79
DDC

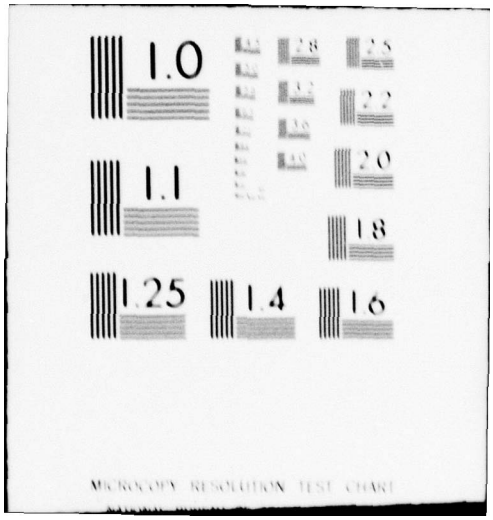
1.0
1.1
1.25
1.4
1.6
2.8
2.5
2.2
2.0
1.8
MICROCOPY RESOLUTION TEST CHART

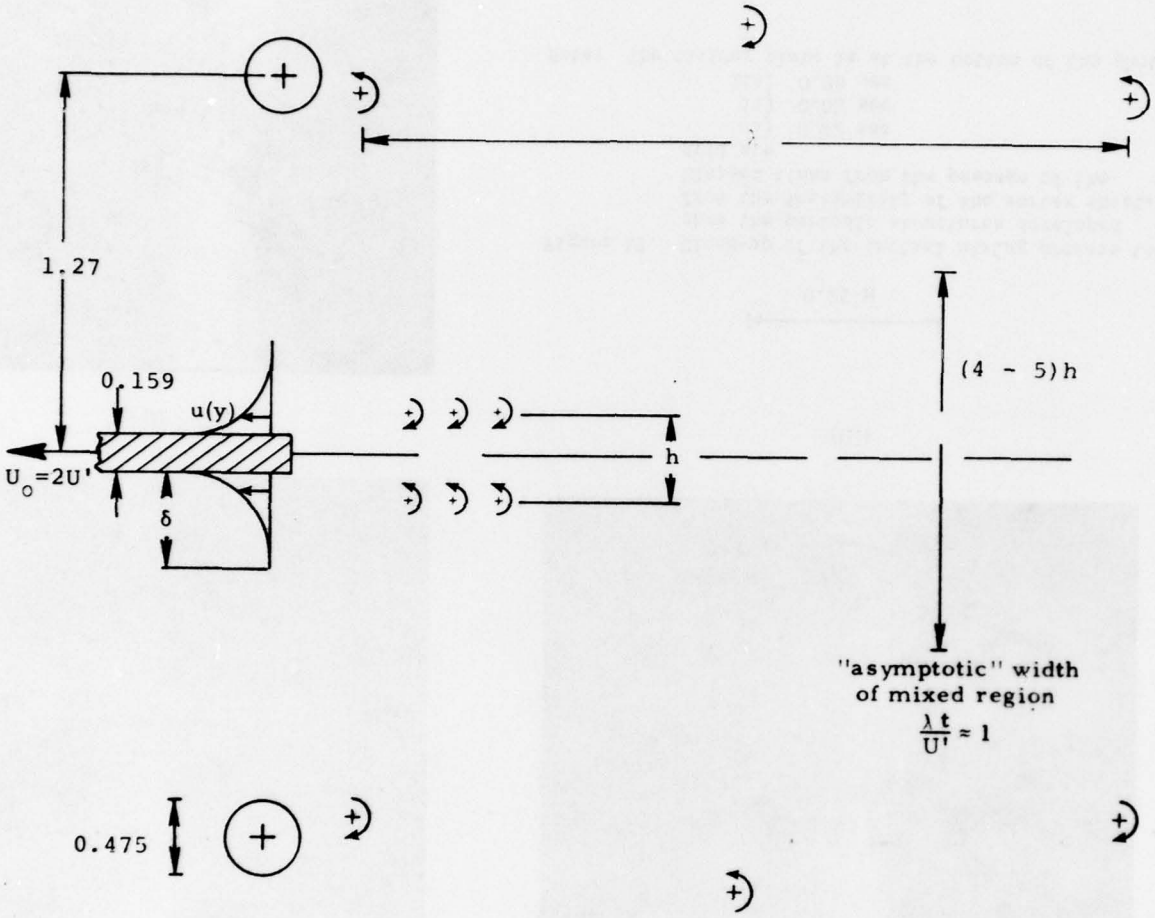

Figure 19. Schematic representation of the parameters associated with the initial mixing process.

Note: All dimensions are in cm

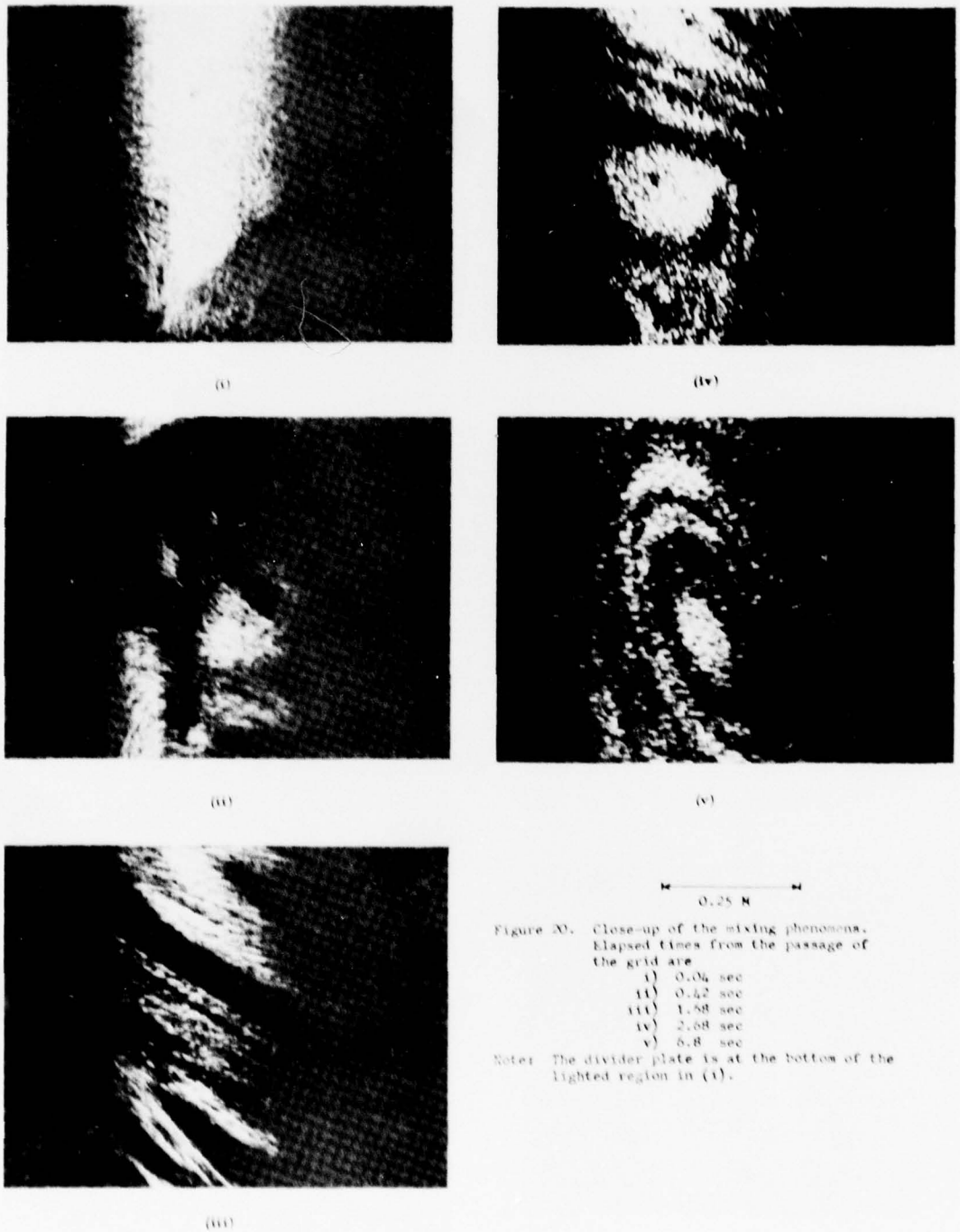

Figure XV. Close-up of the mixing phenomena. Elapsed times from the passage of the grid are
i) 0.04 sec
ii) 0.42 sec
iii) 1.58 sec
iv) 2.68 sec
v) 6.8 sec

Note: The divider plate is at the bottom of the lighted region in (i).

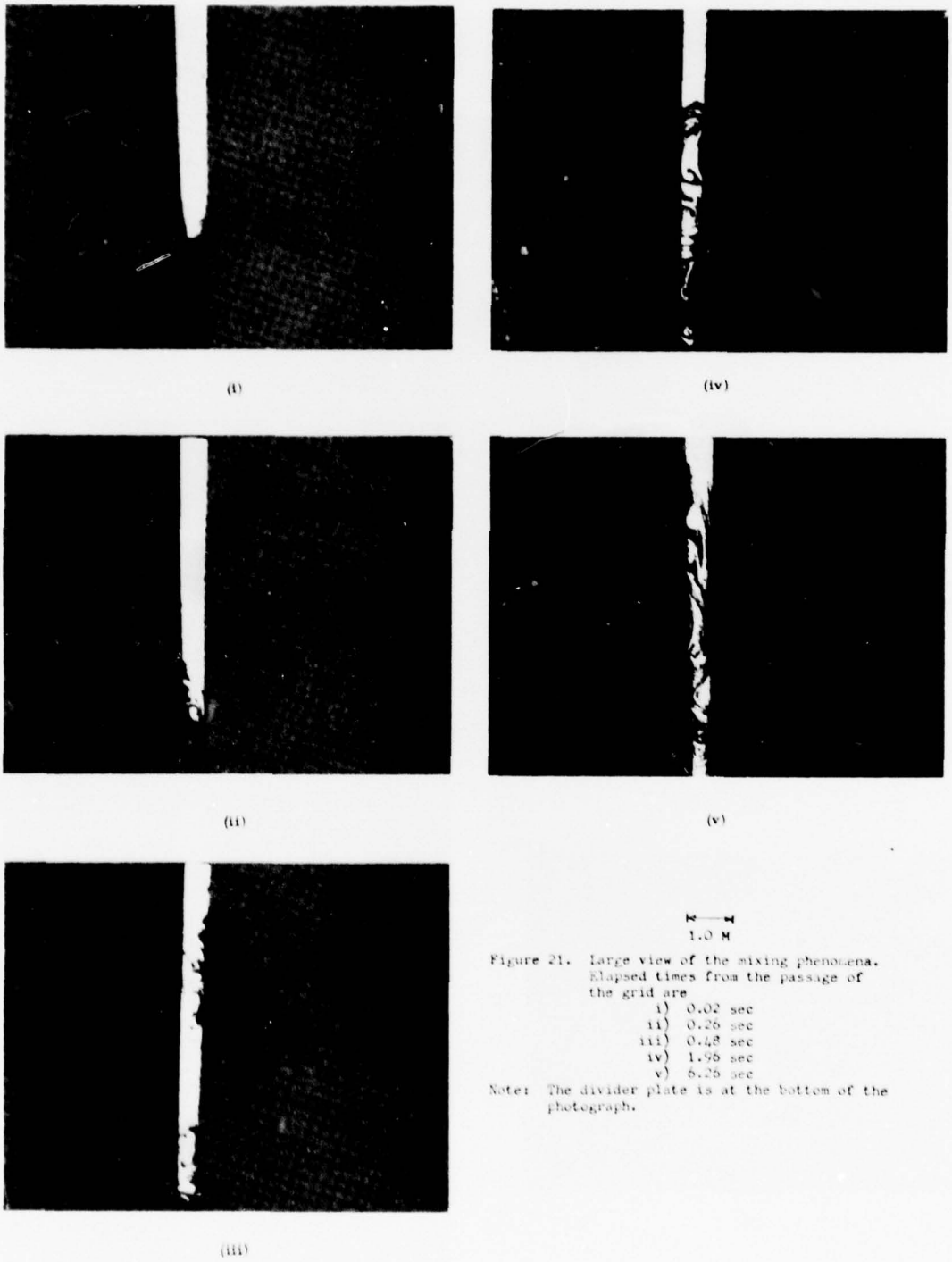

Figure 21. Large view of the mixing phenomena. Elapsed times from the passage of the grid are

i) 0.02 sec
ii) 0.26 sec
iii) 0.48 sec
iv) 1.96 sec
v) 6.26 sec

Note: The divider plate is at the bottom of the photograph.

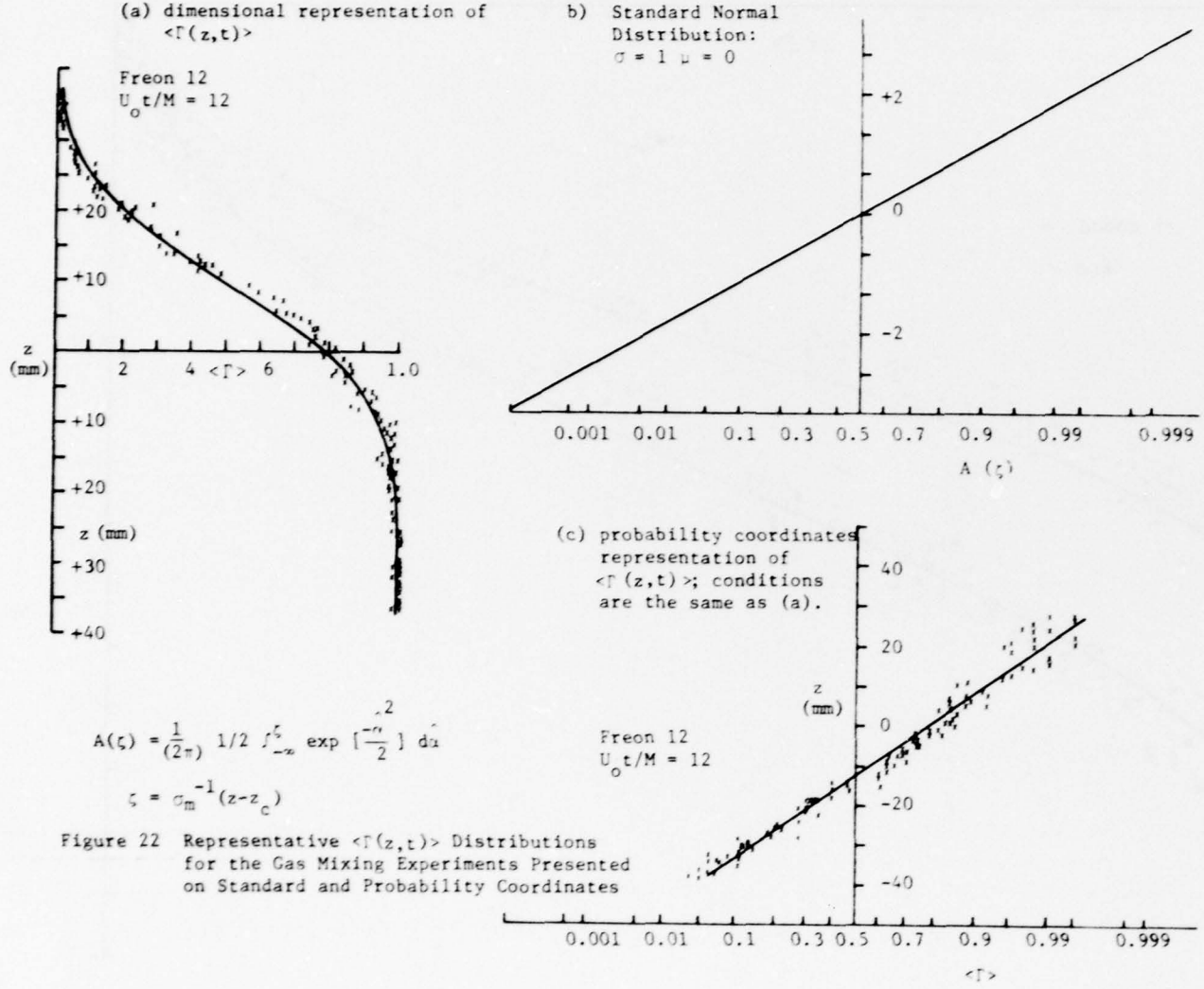

$$A(\zeta) = \frac{1}{(2\pi)}\ 1/2 \int_{-\infty}^{\zeta} \exp\left[\frac{-u^2}{2}\right] du$$

$$\zeta = \sigma_m^{-1}(z - z_c)$$

Figure 22 Representative <Γ(z,t)> Distributions for the Gas Mixing Experiments Presented on Standard and Probability Coordinates

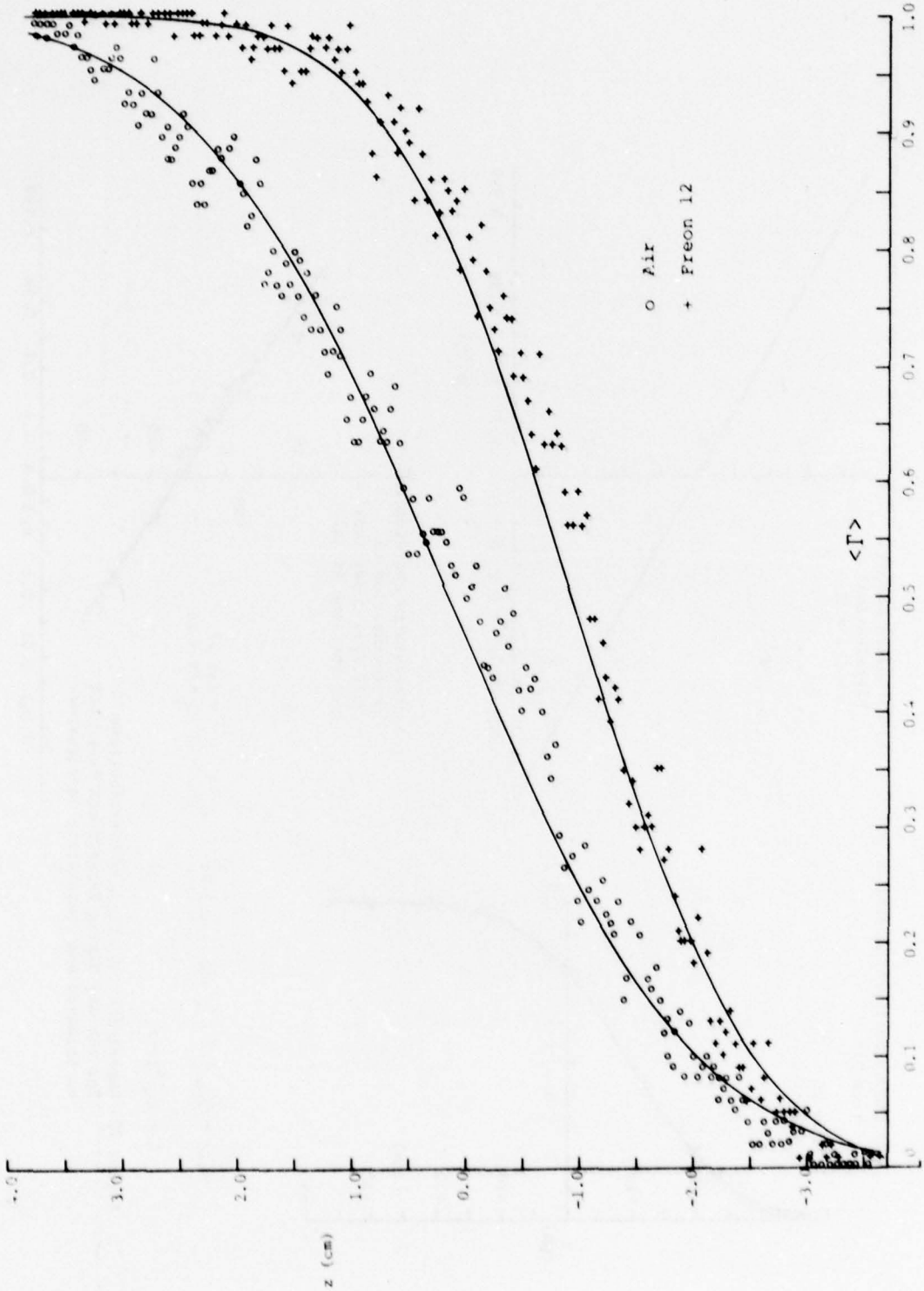

Figure 23. Comparison of the $\Gamma(z,t)$ measurements for the Freon 12 and air data sets $U_o t/M=12$.
Note: Solid curves represent Gaussian C.D.F., see (5.3.1) and (5.3.2.)

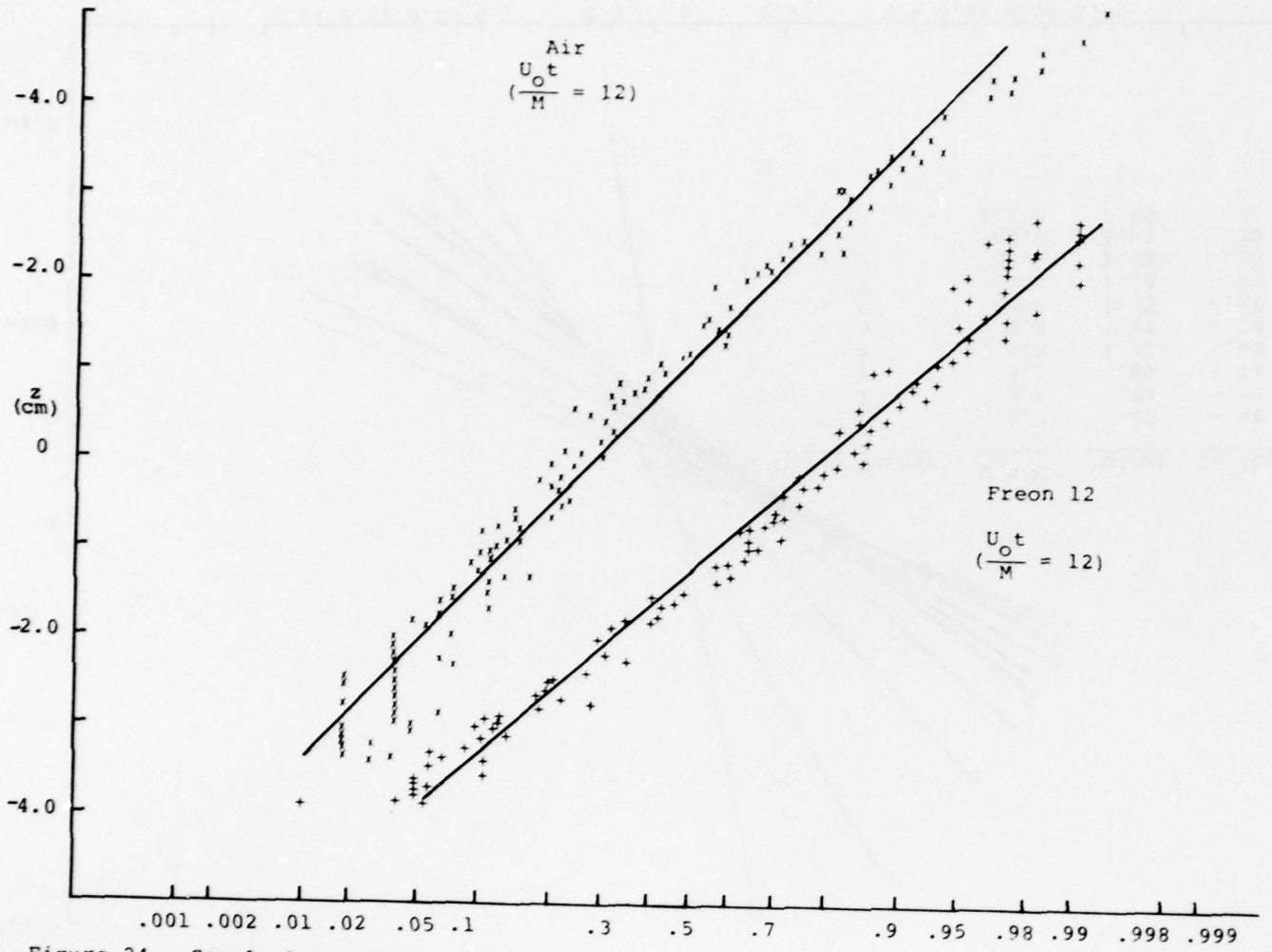

Figure 24. Sample Least Squares Fits, to the Ensemble Average Data for the Freon 12 and Air Carrier Gases, on Probability Coordinates
Note: Solid lines represent Gaussian C.D.F.; see 5.3.1. and 5.3.2.

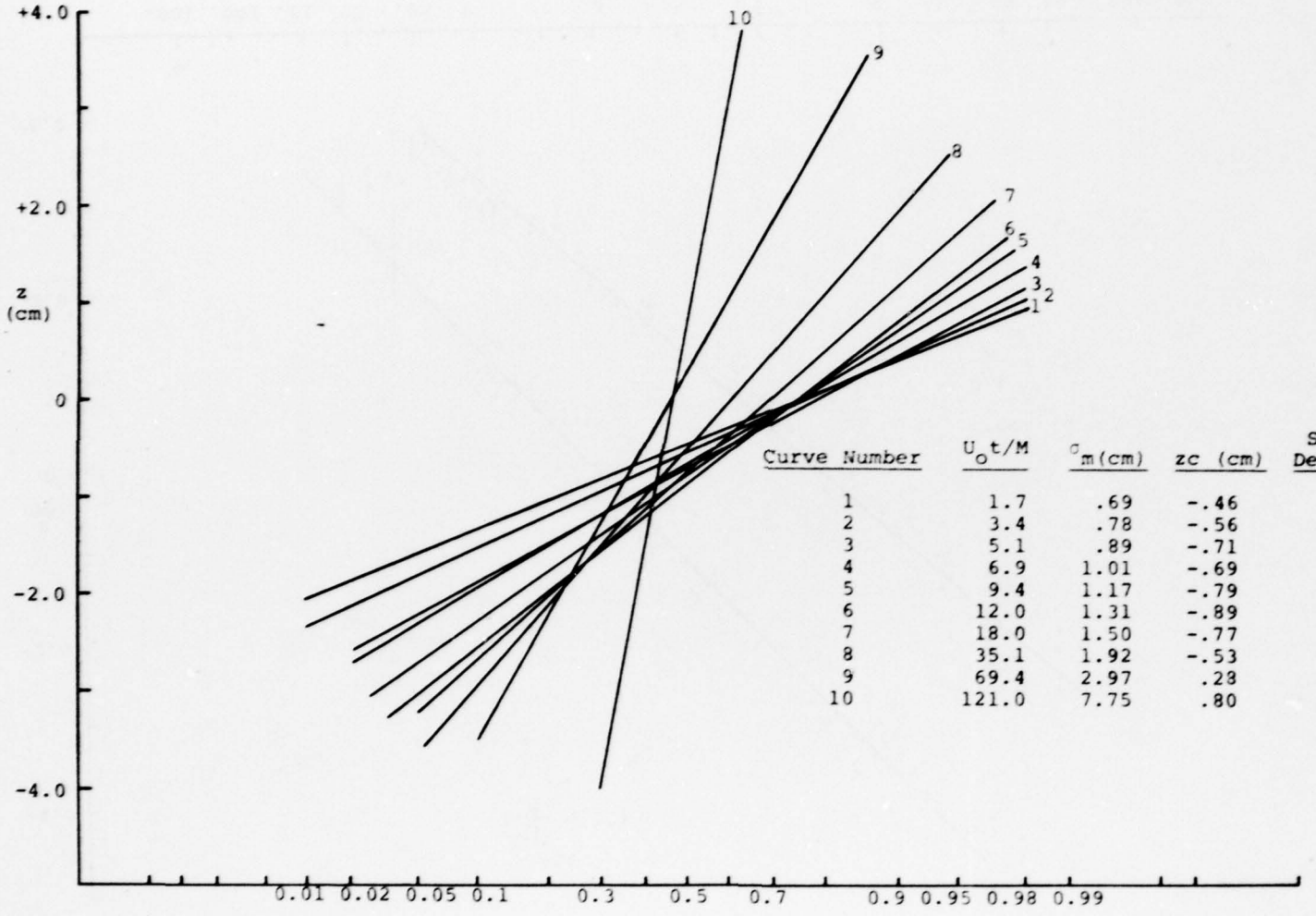

Curve Number	$U_o t/M$	σ_m(cm)	zc (cm)	Standard Deviation
1	1.7	.69	-.46	.041
2	3.4	.78	-.56	.051
3	5.1	.89	-.71	.041
4	6.9	1.01	-.69	.040
5	9.4	1.17	-.79	.042
6	12.0	1.31	-.89	.042
7	18.0	1.50	-.77	.056
8	35.1	1.92	-.53	.053
9	69.4	2.97	.28	.053
10	121.0	7.75	.80	.042

Figure 25. Probability Coordinates Representation of Ensemble Average Concentration for Freon.

Curve Number	$U_o t/M$	σ_m (cm)	z_c (cm)	Standard Deviation
1	1.7	.72	-.36	.038
2	3.4	.82,	-.41	.059
3	5.1	.98	-.42	.047
4	6.9	1.19	-.46	.051
5	9.4	1.27	-.42	.041
6	12.0	1.45	-.57	.048
7	18.0	1.68	-.33	.048
8	35.1	2.28	-.23	.052
9	69.4	3.99	-.86	.059
10	121.0	5.09	-2.5	.076

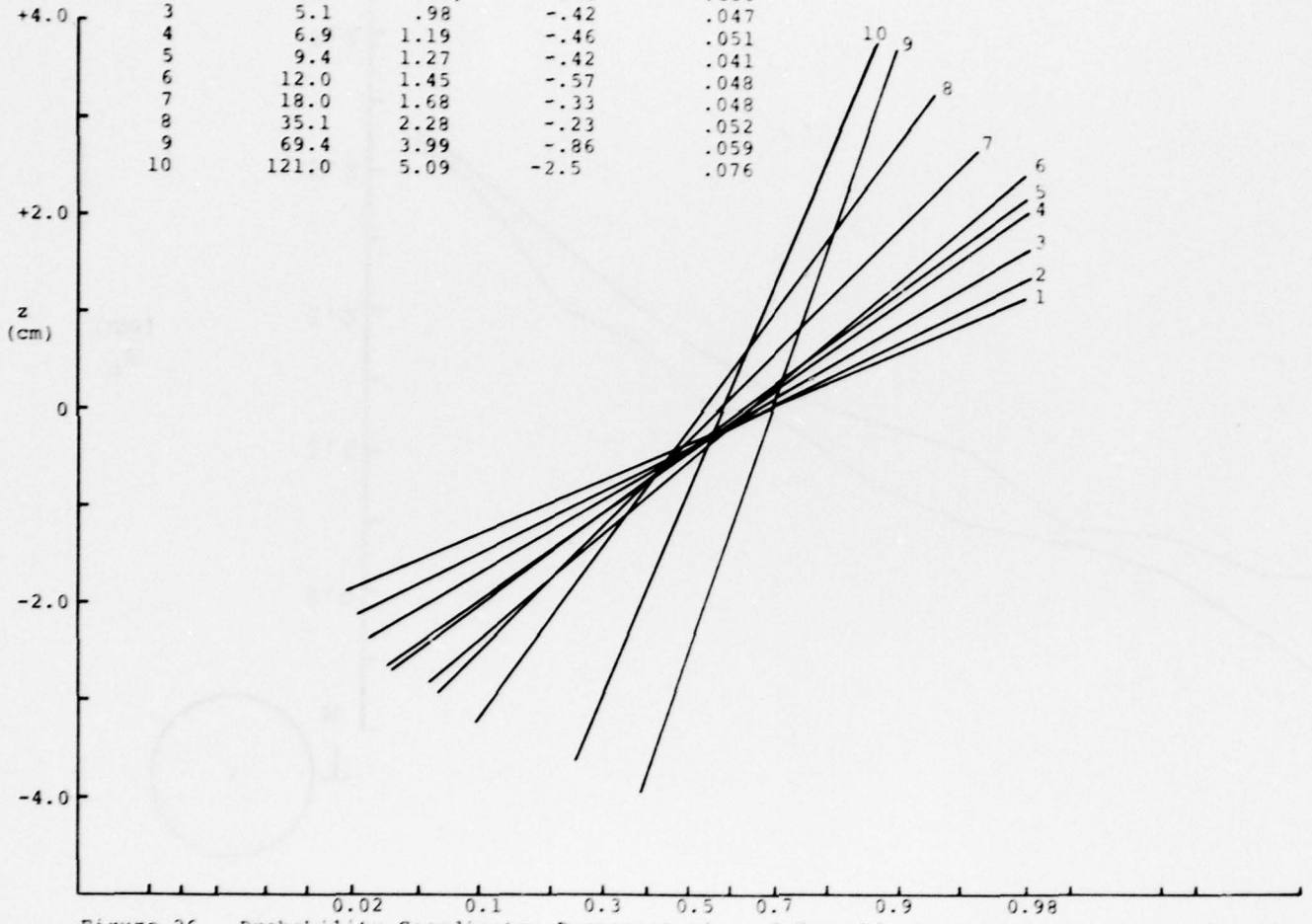

Figure 26. Probability Coordinates Representation of Ensemble Average Concentration for Air

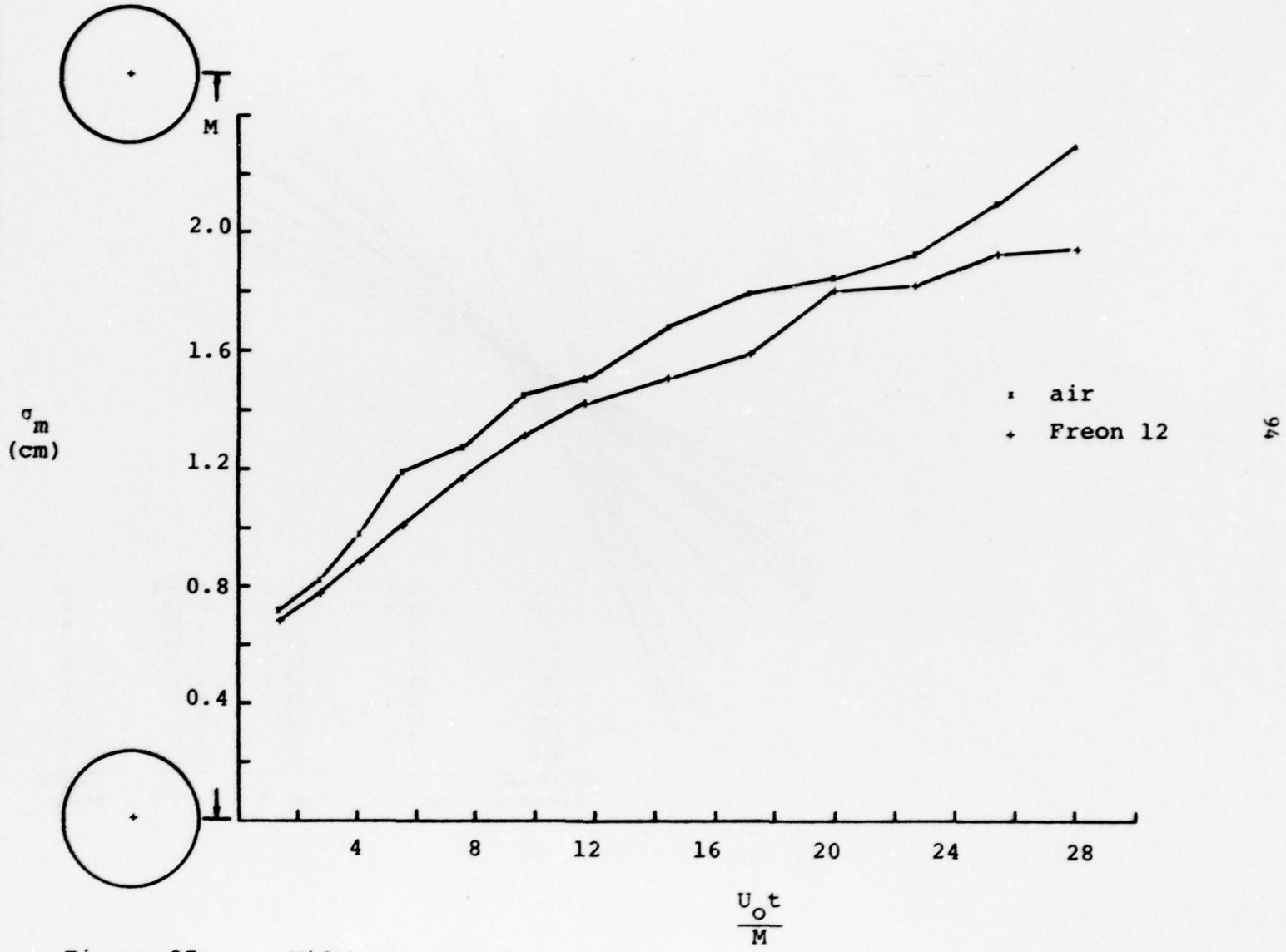

Figure 27a. Width measure (σ_m) of the ensemble average concentration distribution - short time results

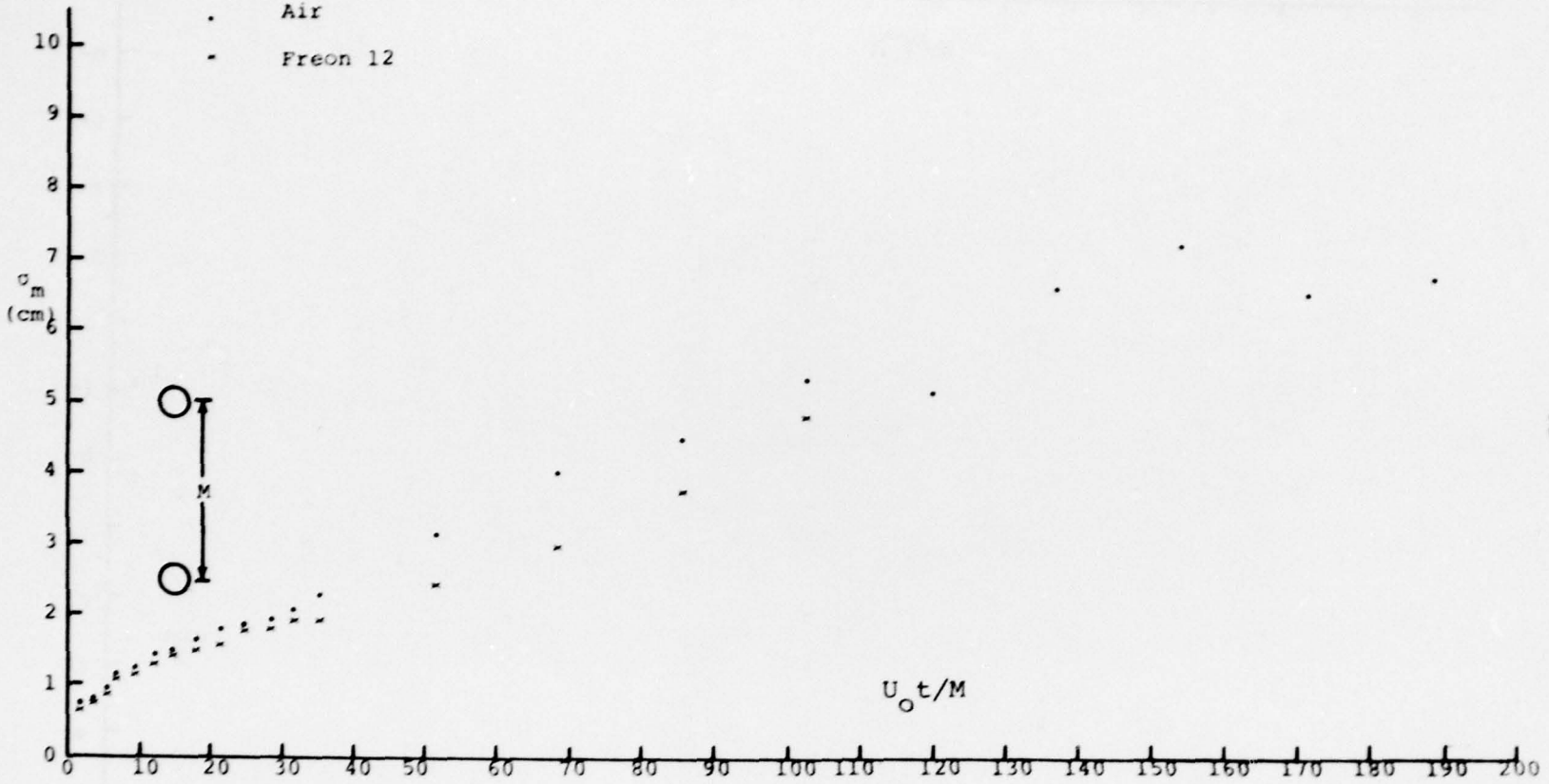

Figure 27b. Width measure (σ_m) of the ensemble average concentration distribution--long time results

NOTE: The $U_o t/M > 100$ values for Freon 12 are not shown since the apparent mixed region migrated beyond the optically sampled region of the mixing chamber.

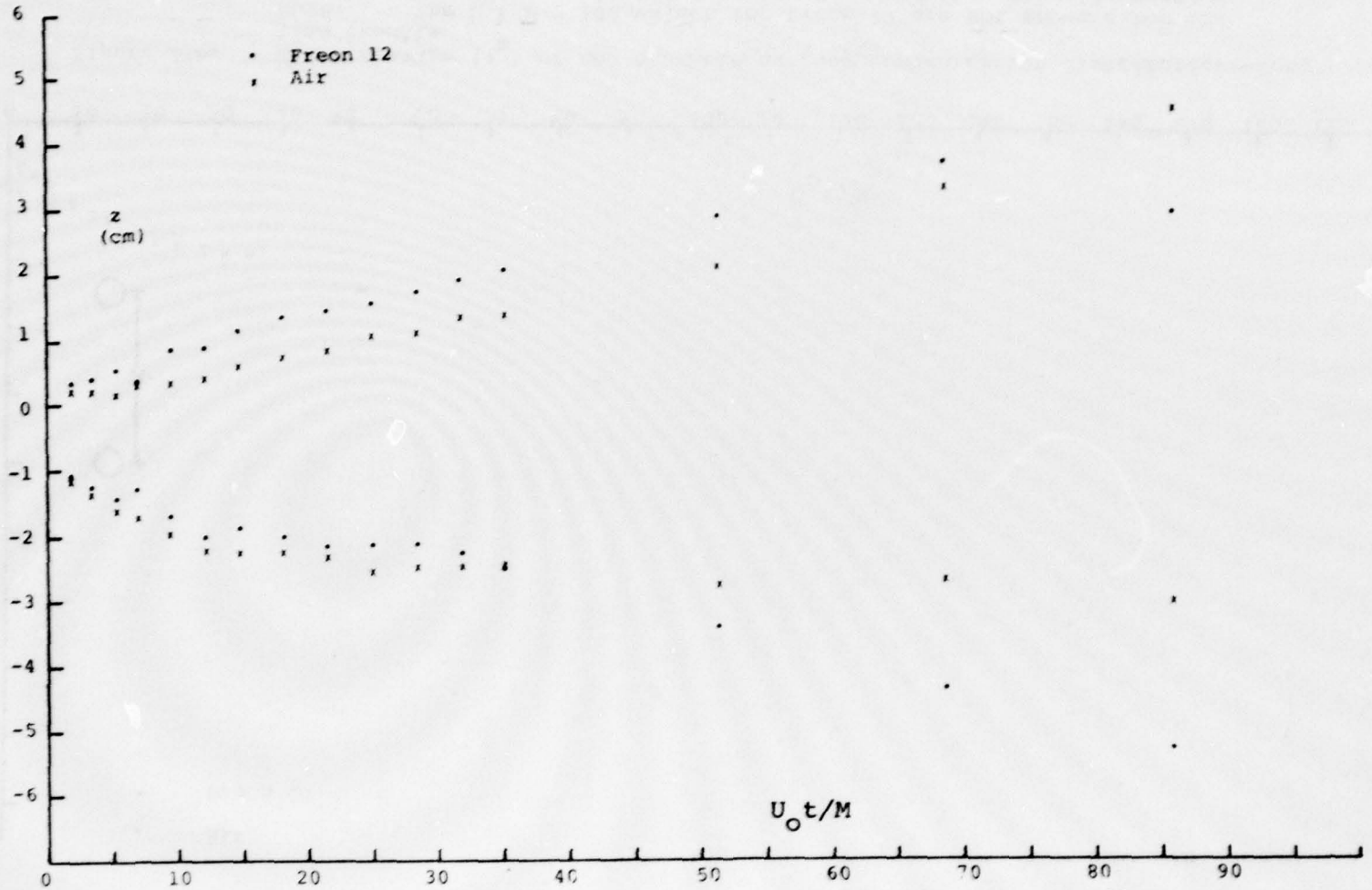

Figure 28. z Values of Physical Displacement from Centerline Corresponding to $\langle \Gamma(z,t) \rangle = 0.15$ and 0.85

$$A = z_{ci} - \langle z_{ci} \rangle$$

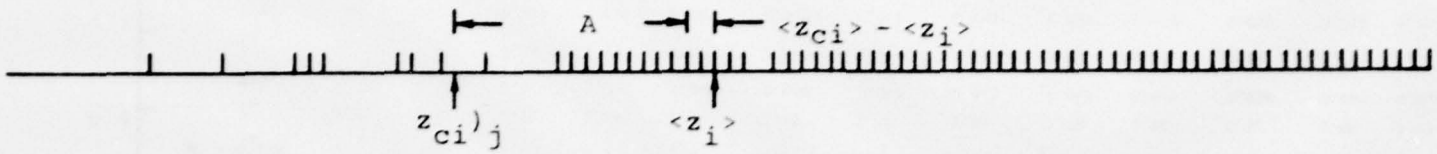

Definitions: $z_{ci})_j$ center of the ith instantaneous scan, jth experiment

$z_{ci})_j - \langle z_i \rangle$ displacement of instantaneous center from ensemble average centerline, jth experiment

$z_{ci})_j - \langle z_{ci} \rangle$ displacement of instantaneous center from the ensemble average of the instantaneous centers, jth experiment

Width Measures: Mixedness... σ_I, parameter in Gaussian C.D.F. which is used to represent $\langle \Gamma(z - \langle z_{ci} \rangle, t)$

Transport... $\sigma_{\Delta z}$, standard deviation of $(z_{ci})_j - \langle z_{ci} \rangle)$

Notes: i = scan number ($1 \leq i \geq 240$), j = experiment number air...$1 \leq j \geq 69$; Freon 12...$1 \leq j \geq 100$

For this schematic representation, the total number of sample volumes is $N_T = 100$, the number of volumes with fluid B is 68 and the number of volumes with fluid A is 32. $\langle z_{ci} \rangle$ is arbitrarily selected.

Figure 29. Definitions of Instantaneous Scan Measures

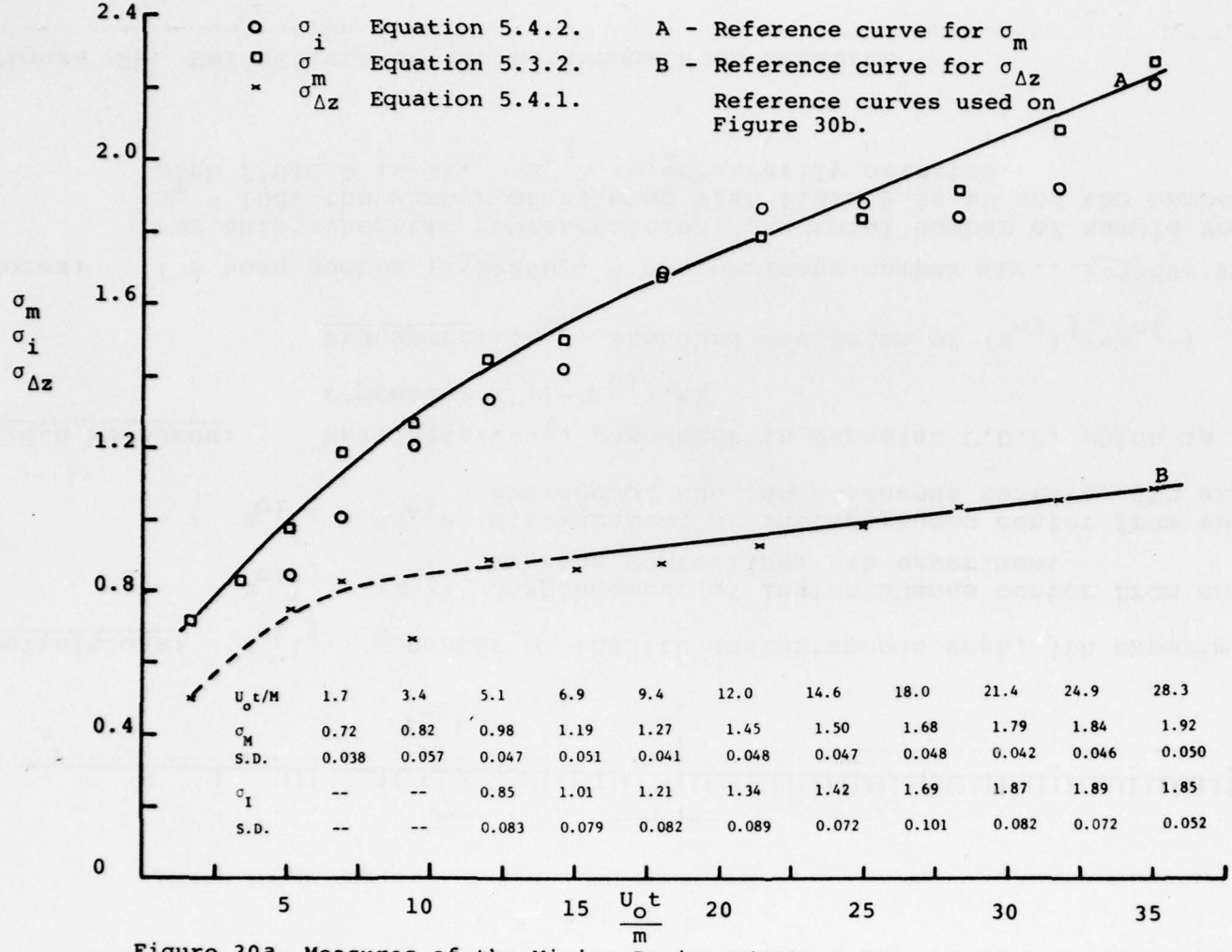

$U_o t/M$	1.7	3.4	5.1	6.9	9.4	12.0	14.6	18.0	21.4	24.9	28.3	31.7	35.1
σ_M	0.72	0.82	0.98	1.19	1.27	1.45	1.50	1.68	1.79	1.84	1.92	2.09	2.28
S.D.	0.038	0.057	0.047	0.051	0.041	0.048	0.047	0.048	0.042	0.046	0.050	0.047	0.052
σ_I	--	--	0.85	1.01	1.21	1.34	1.42	1.69	1.87	1.89	1.85	1.93	2.22
S.D.	--	--	0.083	0.079	0.082	0.089	0.072	0.101	0.082	0.072	0.052	0.058	0.060

Figure 30a. Measures of the Mixing Region Width as Determined from the Conventional and Instantaneous Scans...air, carrier gas.

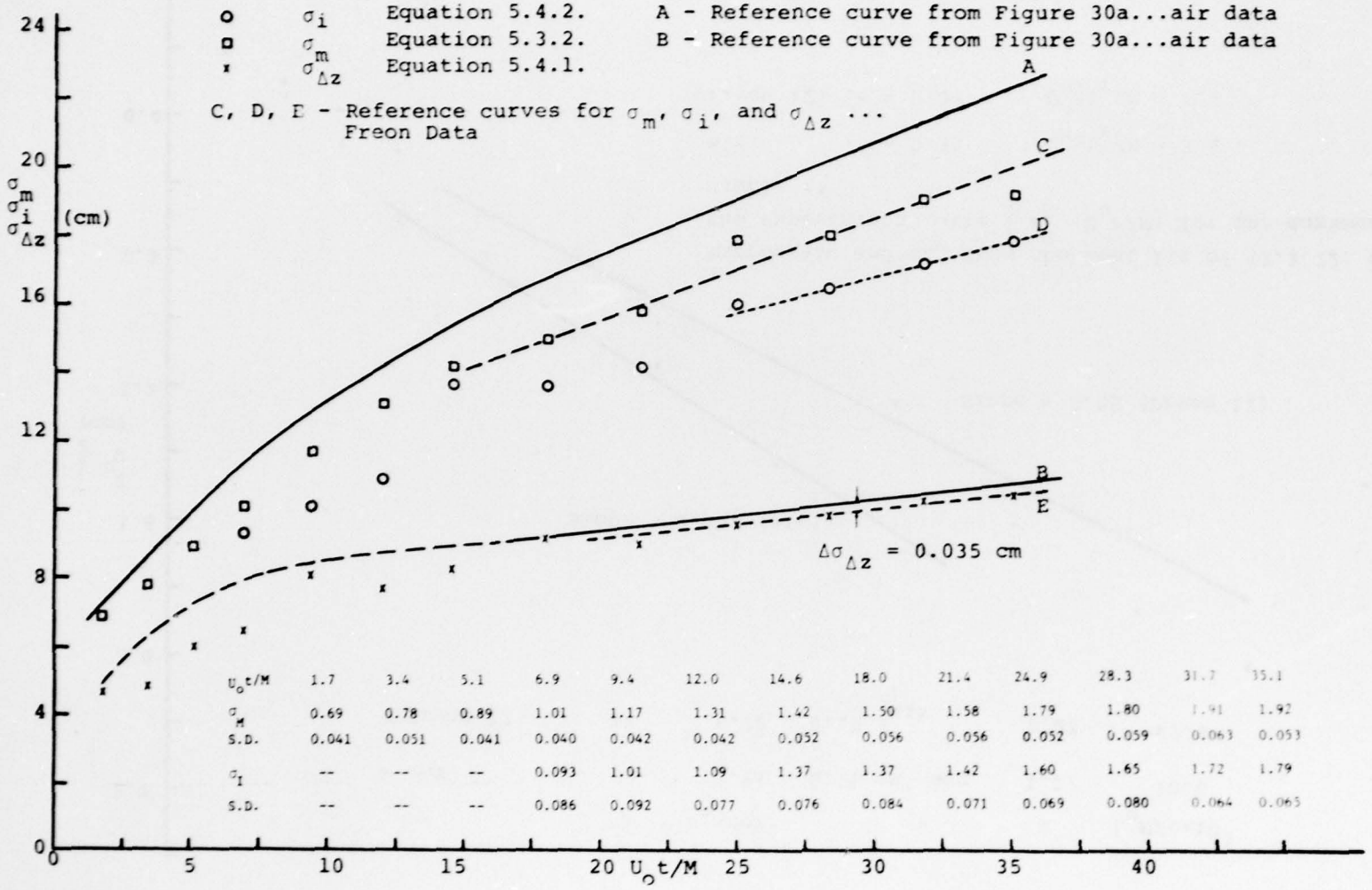

$U_o t/M$	1.7	3.4	5.1	6.9	9.4	12.0	14.6	18.0	21.4	24.9	28.3	31.7	35.1
σ_M	0.69	0.78	0.89	1.01	1.17	1.31	1.42	1.50	1.58	1.79	1.80	1.91	1.92
S.D.	0.041	0.051	0.041	0.040	0.042	0.042	0.052	0.056	0.056	0.052	0.059	0.063	0.053
σ_I	--	--	--	0.093	1.01	1.09	1.37	1.37	1.42	1.60	1.65	1.72	1.79
S.D.	--	--	--	0.086	0.092	0.077	0.076	0.084	0.071	0.069	0.080	0.064	0.065

Figure 30b. Measures of the Mixing Region width as determined from the conventional and the Instantaneous Scans...Freon 12 Carrier Gas

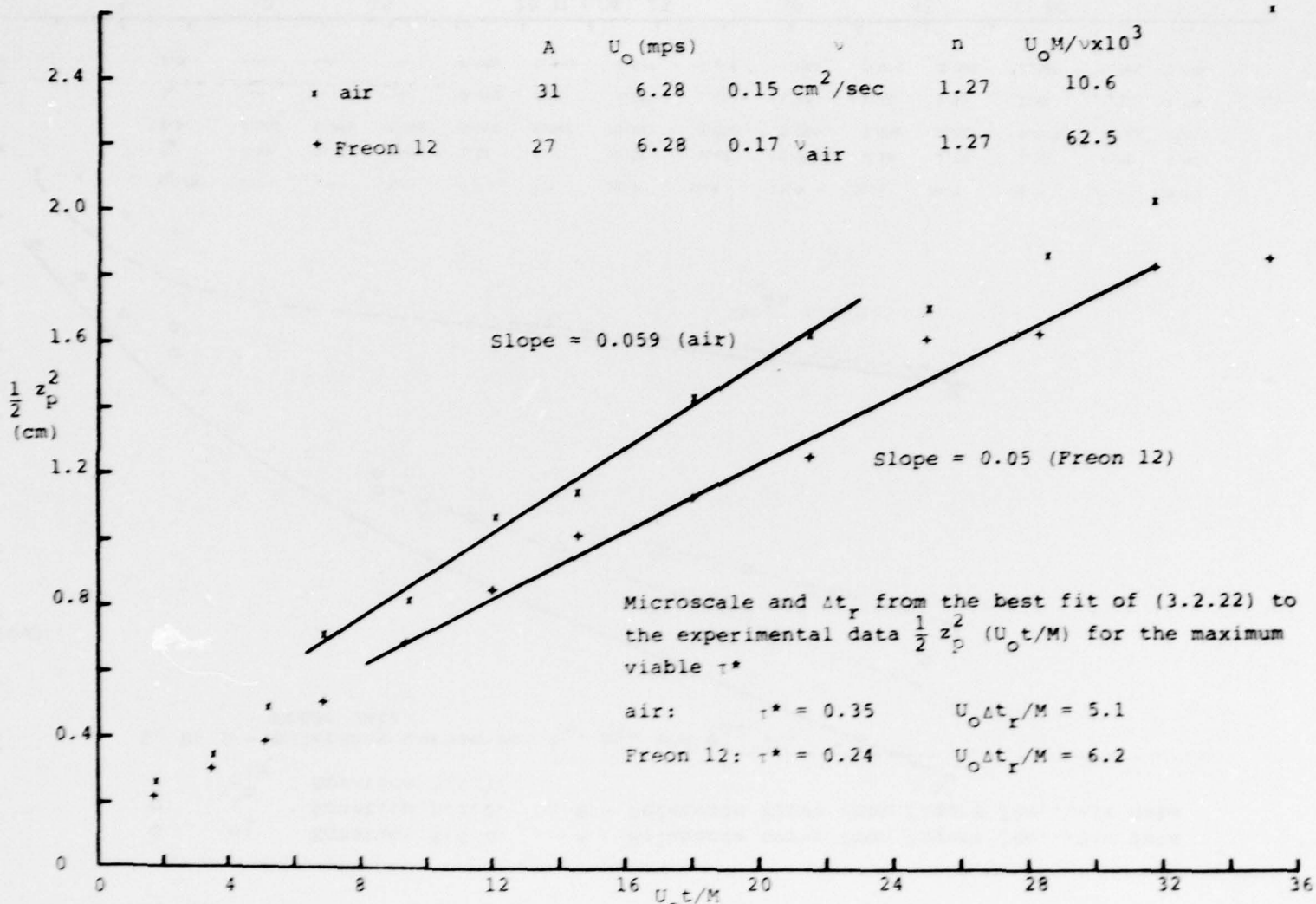

Microscale and Δt_r from the best fit of (3.2.22) to the experimental data $\frac{1}{2} z_p^2$ $(U_o t/M)$ for the maximum viable τ^*

air: $\tau^* = 0.35$ $U_o \Delta t_r/M = 5.1$

Freon 12: $\tau^* = 0.24$ $U_o \Delta t_r/M = 6.2$

Figure 31. Evaluation of the Lagrangran microscale (τ^*) and the effective release time (t_r)

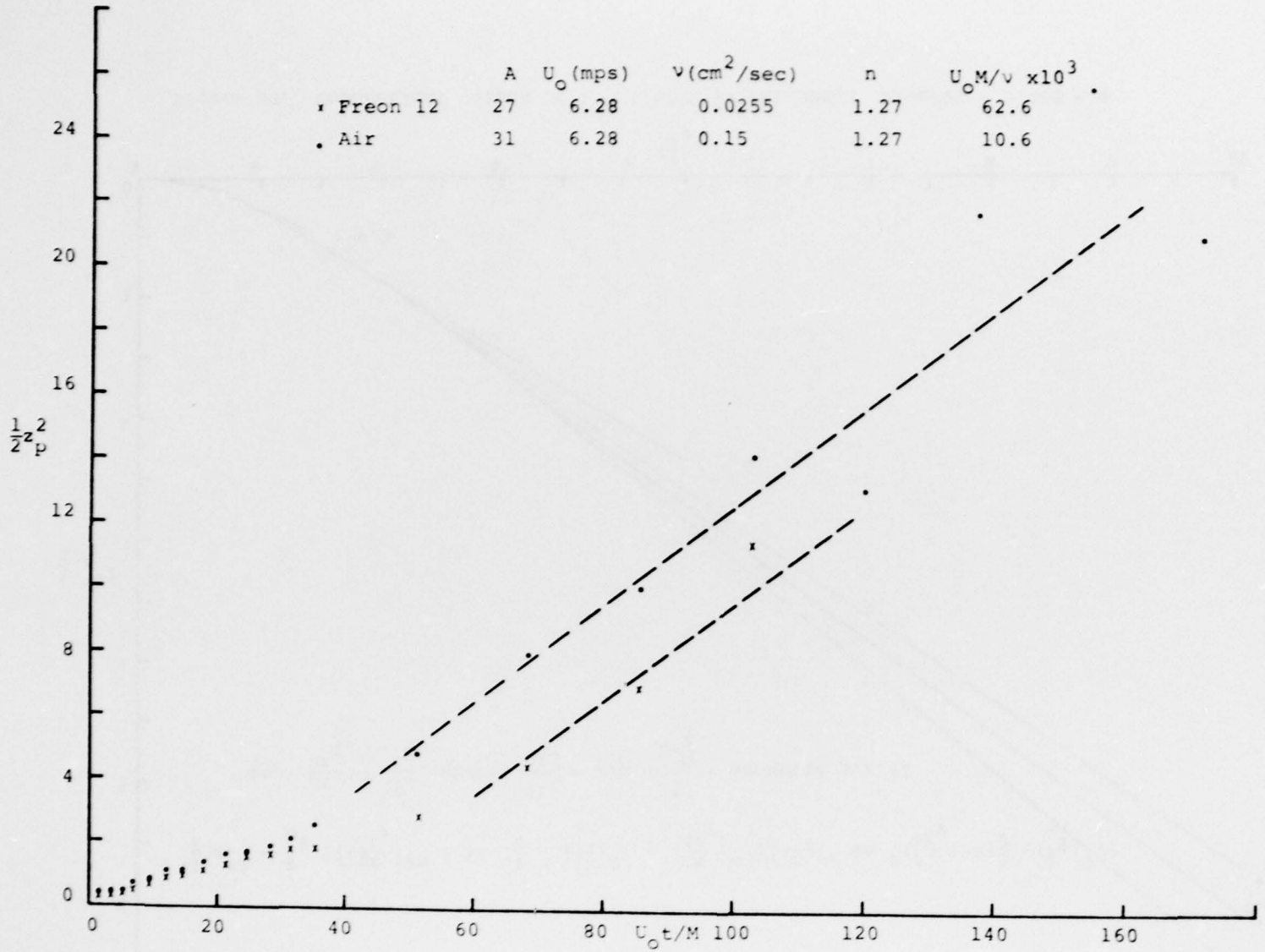

Figure 32. Long Time Results for the Dispersion Parameter z_p^2

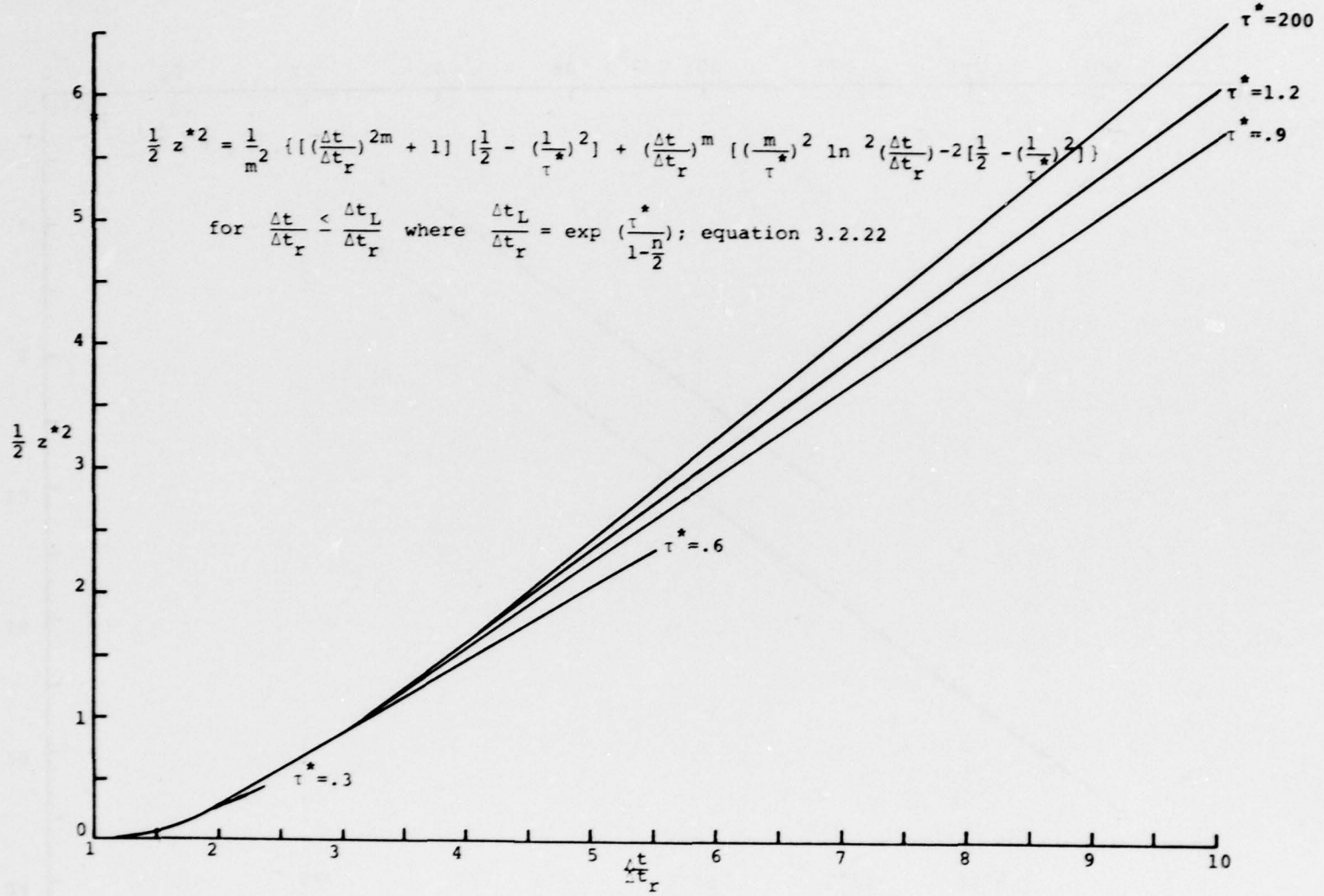

Figure 33. Theoretical values of z^{*2} $(\Delta t/\Delta t_r; \tau^*, n)$-NOTE: (1-n/2) = 0.365 = m

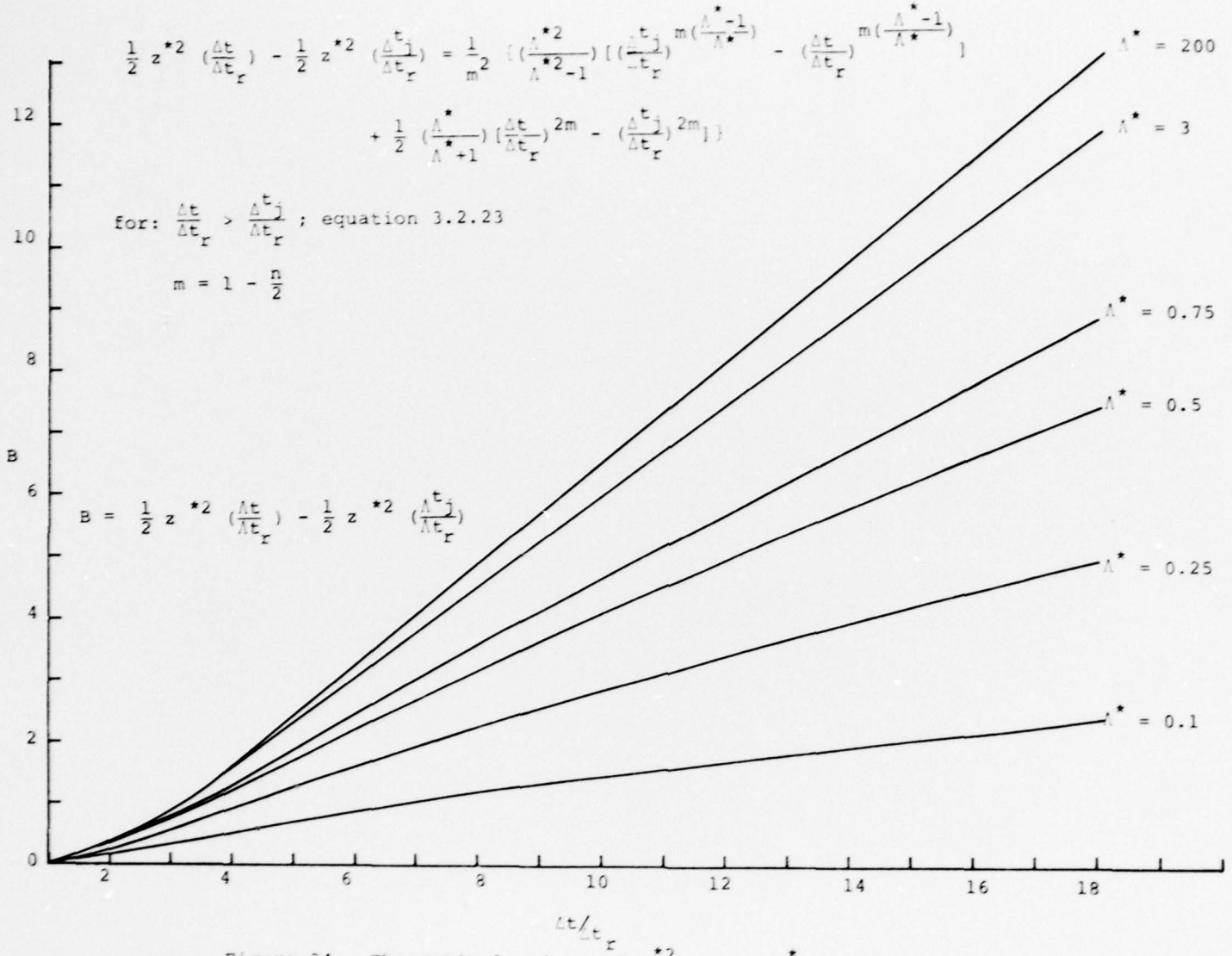

Figure 34. Theoretical values of $z^{*2}(\Delta t/\Delta t_r; \Lambda^*, \Delta t_j, \Delta t_r, n)$ from Equation (3.2.23)
NOTE: $(1 - n/2) = 0.365$, $\Delta t_j/\Delta t_r = 1$

Unclassified

SECURITY CLASSIFICATION OF THIS PAGE (When Data Entered)

REPORT DOCUMENTATION PAGE		READ INSTRUCTIONS BEFORE COMPLETING FORM
1. REPORT NUMBER MSU-1-PU	2. GOVT ACCESSION NO.	3. RECIPIENT'S CATALOG NUMBER
4. TITLE (and Subtitle) AN EXPERIMENTAL STUDY OF THE TRANSPORT OF A NON-DIFFUSIVE SCALAR CONTAMINANT IN THE DECAYING TURBULENCE FIELD OF AN ENCLOSED CHAMBER		5. TYPE OF REPORT & PERIOD COVERED Final 6. PERFORMING ORG. REPORT NUMBER
7. AUTHOR(s) K. C. Cornelius J. F. Foss		8. CONTRACT OR GRANT NUMBER(s) N00014-75-C-1143 NR-098-038
9. PERFORMING ORGANIZATION NAME AND ADDRESS Michigan State University East Lansing, Michigan 48824		10. PROGRAM ELEMENT, PROJECT, TASK AREA & WORK UNIT NUMBERS
11. CONTROLLING OFFICE NAME AND ADDRESS Project SQUID Headquarters Chaffee Hall, Purdue University West Lafayette, Indiana 47907		12. REPORT DATE August 1978 13. NUMBER OF PAGES 123
14. MONITORING AGENCY NAME & ADDRESS(if different from Controlling Office) Office of Naval Research, Power Program, Code 473 Department of the Navy 800 No. Quincy Street Arlington, VA 22217		15. SECURITY CLASS. (of this report) Unclassified 15a. DECLASSIFICATION/DOWNGRADING SCHEDULE

16. DISTRIBUTION STATEMENT (of this Report)

This document has been approved for public release and sale; its distribution is unlimited.

17. DISTRIBUTION STATEMENT (of the abstract entered in Block 20, if different from Report)

Same

18. SUPPLEMENTARY NOTES

19. KEY WORDS (Continue on reverse side if necessary and identify by block number)

Turbulence
Two-Phase Flow
Flow Visualization
Particle Generators
Laser Optics

20. ABSTRACT (Continue on reverse side if necessary and identify by block number)

An experimental investigation of the convective properties of a turbulence field within a closed mixing chamber has been executed; the investigation is supported by appropriate theoretical analyses. The purpose of the study were (i) to develop an experimental technique which could ascertain the convective, or dispersive, properties of such a turbulence field (i.e., with the constraint of "zero" molecular diffusivity), and (ii) to document the influence of the Reynolds number on the convective transport properties of a representative field.

DD FORM 1 JAN 73 1473 EDITION OF 1 NOV 65 IS OBSOLETE
S/N 0102-LF-014-6601

Unclassified

SECURITY CLASSIFICATION OF THIS PAGE (When Data Entered)

The derived technique involves the introduction of submicron particulate matter into the lower half-volume (as defined by a horizontal splitter plate which is rapidly removed from the chamber at the initiation of an experiment) and the subsequent monitoring of the presence/absence of this contaminant along a vertical line centered at the plane of the splitter plate. An optical/mechanical/electrical technique was used to scan 205 locations along a 7.4 cm portion of an incident, focused ($d \simeq 0.1$ mm), laser beam and the scattered light intensity was used to identify the presence or absence of the fluid elements which originated in the lower half-volume. That is, since the particulate matter is shown to be too large to respond to the diffusion effects of the Browman motion of the gas, and too small to move independently of the fluid element of its origin, it is inferred that it faithfully marks the lower half-volume fluid over the duration of the experiment (0.6 sec). The 7.4 cm scan length covered 2.92 mesh lengths of the biplane, round rod, turbulence generating grid. Air was used for 69 experiments; Freon 12 was used for 100 experiments ($\nu_{air} = 5.8\nu_{Freon\ 12}$).

A principal result of this investigation is that the particle dispersion is dependent upon the mesh Reynolds number (U_oM/ν); the width of the mixing field was found to decrease as the Reynolds number was increased. A theoretical model of the dispersion was developed using the suggestion by Batchelor and Townsend [1956] that the Lagrangian velocity auto correlation function can be made stationary, in a decaying turbulence field, by an appropriate stretching of the time coordinate. The present model utilizes both the Langrangian micro and macro scales to describe this correlation function; numberical values for these two scales are inferred from the experimental data. The observed decrease in the particle dispersion with increasing Reynolds number is supported by a previously suggested relationship between the Lagrangian micro scale and the mesh Reynolds number, a new value for the coefficient in this relationship is proposed.

Analytical considerations are presented to support the use of a (spatial) Gaussian cumulative distribution function for the description of the ensemble average concentration; viz, $\Gamma(z,t) = [2\pi\ \sigma_m(t)^2]^{-\frac{1}{2}} \int_o^z \exp - [(\hat{\alpha} - \langle z \rangle)/2\sigma_m(t)^2]d\hat{\alpha}$. Satisfactory agreement between this distribution and the experimental data was obtained; $\sigma_m(t)^2$ was used to evaluate the mean square particle dispersion, z_p^2. Two properties of the instantaneous scans were defined: i) an ensemble average measure of the instantaneous width of the mixing field, σ_I, and an ensemble average measure of the migration of the instantaneous center lines, $\sigma_{\Delta z}$. The instantaneous scans are shown to have essentially the same width as that of the ensemble average field $\sigma_I \gtrsim 0.8\sigma_m$ whereas $\sigma_{\Delta z}$ exhibits very little growth with respect to time following the establishment of its nominal value at $U_o t/M \simeq 8$.